



Dipartimento Interateneo di Fisica "M.Merlin"

TESI DI LAUREA MAGISTRALE IN
"NUCLEAR, SUBNUCLEAR AND ASTROPARTICLE
PHYSICS"

Search for $H \rightarrow c\bar{c}$
at a Muon Collider experiment

Relatrici:
Chiar.ma Prof.ssa Anna Colaleo
Dott.ssa Rosamaria Venditti

Laureanda:
Paola
Mastrapasqua

Anno Accademico 2019/2020

Contents

Introduction	13
1 Standard Model state of art and prospect	15
1.1 Basics of QCD and jet physics	16
1.2 Higgs Boson in the Standard Model	20
1.3 Status of Higgs Boson Physics at LHC	24
1.4 Higgs Boson Physics at Future Colliders	29
1.5 Muon Collider potential	34
2 Muon Collider machine and detector	38
2.1 Muon Accelerator Complex	39
2.2 Detector description	42
2.2.1 Tracking system	44
2.2.2 Calorimetry	46
2.2.3 Muon detector system	49
2.3 Data taking conditions: the Beam Induced Background issue . .	50
3 Event reconstruction at Muon Collider	56
3.1 Software tools	56
3.2 Track reconstruction	57
3.2.1 Track parametrization	57
3.2.2 Track finding	59
3.2.3 Track fitting	61
3.3 Particle Flow	61
3.4 Jet Reconstruction	65
3.4.1 Jet reconstruction efficiency	66
3.5 Secondary Vertex Reconstruction	72
3.5.1 LCFIPlus processor	74
3.5.2 Track selection for vertex finding	77
3.5.3 Performance of vertex finding	79
4 The c jet identification	82
4.1 Heavy-flavour jet discriminating variables	82
4.1.1 Track selection and variables	83
4.1.2 Secondary vertex selection and variables	86
4.1.3 Soft lepton selection and variables	89
4.2 Tagger algorithm description	90
4.3 Flavour tagging performance	96

5 Analysis of $H \rightarrow c\bar{c}$	99
5.1 Signal and background event generation	99
5.2 Event selection	100
5.3 Statistical analysis and results	110
5.4 Future developments	111
Conclusions	113
Appendices	115
A Tagger input variables	116
B Multivariate Analysis	119
B.1 The Decision Tree	120
B.2 Boosting of a tree	122
B.3 Kolmogorov-Smirnov test	123
Bibliography	129

List of Figures

1.1	A summary table with all the SM particles: the fermions (on the left) are divided into quarks (in violet) and leptons (in green), while the bosons (on the right), are classified into gauge bosons, i.e. the carriers of the interactions (in red) and the scalar Higgs boson (in yellow). For each particle, the mass, electric charge and spin values are reported.	16
1.2	Illustration of the antiscreen effect in QCD (left) and of an approximate behaviour of the effective color charge versus the distance from the bare color charge (right). The distance r can be equivalently expressed in terms of the transferred four-momentum Q^2 between the charge and the probe, since $r \simeq 1/Q^2$	18
1.3	Summary of measurements of α_S as a function of the energy scale Q . The respective degree of QCD perturbation theory used in the extraction of α_S is indicated in brackets (NLO: next-to-leading order; NNLO: next-to-next-to-leading order; NNLO+res.: NNLO matched to a resummed calculation; N3LO: next-to-NNLO).	18
1.4	Quark/gluon cascades (left) and fragmentation to hadrons induced by confinement forces (right), in $\mu^+\mu^-$ annihilation.	19
1.5	Four jet event in the Muon Collider detector: front view (left) and lateral view (right).	20
1.6	Main leading order Feynman diagrams contributing to the Higgs boson production in (a) gluon fusion, (b) Vector-boson fusion, (c) Higgs-strahlung (or associated production with a gauge boson at tree level from a quark-quark interaction), (d) associated production with a gauge boson (at loop level from a gluon-gluon interaction), (e) associated production with a pair of top quarks [3].	25
1.7	The SM Higgs boson production cross sections as a function of the center of mass energy for pp collisions (left) and the branching ratios for the main decays of the SM Higgs boson near $m_H = 125$ GeV (right). The VBF process is indicated here as qqH. The theoretical uncertainties are indicated as bands [3].	26
1.8	The invariant mass distribution of diphoton candidates observed by ATLAS at Run 2 (left). The residuals of the data with respect to the fitted background are displayed in the lower panel. The m_{4l} distribution from CMS Run 2 data (right)[3].	27

1.9	Summary plot of the fit to the production–decay signal strength products μ_i^f [15]. The points indicate the best fit values while the horizontal bars indicate the 1σ CL intervals. The hatched areas indicate signal strengths that are restricted to nonnegative values.	28
1.10	Result of the phenomenological (M, ϵ) fit overlayed with the SM expectation for ATLAS [16] and CMS [17]. The ratio of the fit result to SM prediction is shown in the bottom part of the figure. The linear trend is experimentally confirmed.	30
1.11	Higgs production cross sections in e^+e^- collisions. The cross section of different production processes for single and double Higgs production are shown as function of \sqrt{s} . The dominant processes for single Higgs production are Higgs-strahlung (ZH) for \sqrt{s} less than 500 GeV and VBF ($H\nu_e\bar{\nu}_e$ and He^+e^-) for greater values [1].	33
1.12	The energy at which the proton collider cross-section equals that of a muon collider. The dashed line assumes comparable Feynman amplitudes for the muon and the proton production processes. A factor of ten enhancement of the proton production amplitude squared, possibly due to QCD production, is considered in the continuous line [28].	35
1.13	Double Higgs production at a high energy muon collider via W^+W^- fusion. The production goes through the VBF topology.	36
1.14	W^+W^- fusion (solid) and analogous s-channel annihilation (dashed) cross sections for HX (left), HHX (middle) and HHHX (right) [30].	37
2.1	Schematic layouts of Muon Collider complexes based on the proton driver scheme (top) and on the low emittance positron driver scheme (bottom).	39
2.2	Conceptual picture of the principle of ionization cooling. A particle loses momentum by ionizing an energy absorber, where only the longitudinal momentum is restored by RF cavities (left). Longitudinal cooling is achieved through the process of emittance exchange (right).	41
2.3	Plan views of MARS (simulation code [45]) for the Interaction Region (top) and the detector with the MDI (bottom). The tungsten components are coloured in yellow, empty spaces in light blue, iron components in red and concrete supports in grey.	43
2.4	Longitudinal section of the detector at the Muon Collider. Each sub-detector system is indicated and briefly described in terms of its components.	44
2.5	Longitudinal section of the full tracker system.	45
2.6	The VTX barrel detector (left), and longitudinal view of the entire VTX (right) where endcap detectors are visible as half disks.	45
2.7	Longitudinal section of the calorimeter system.	48

2.8	Longitudinal section of the solenoid (cyan) and muon detectors (in blue and green).	49
2.9	MARS [45] model of the IR and detector. Several BIB tracks are also shown [47].	50
2.10	Particle composition of the beam-induced background as a function of the muon decay distance from the interaction point [48].	51
2.11	Momentum spectra of the beam-induced background particles at the detector entry point [48].	51
2.12	Time of arrival of the background particles at the detector entry point with respect to the bunch crossing time [48].	52
2.13	Simulated time of arrival (TOF) of the beam background particles to the tracker modules, summing up all the modules, with respect to the expected time (T0) of a photon emitted from the interaction point and arriving at the same module [48].	53
2.14	Average density of BIB hits in the tracker layers per bunch-crossing (top) and polar angle distribution of the BIB hits for one bunch-crossing (bottom) [49].	54
2.15	BIB energy distribution in the calorimeter (top) and distribution of the arrival time at a given calorimetry position of BIB particles and prompt muons (bottom). Particle arrival time is measured with respect to t_0 , defined as the arrival time in the given position of a photon produced in the primary vertex at the collision time [31].	55
3.1	Projection of a helix in the xy (left) and sz (right) plane.	58
3.2	Schematic representation of a traditional energy reconstruction algorithm (left) opposed to a the new particle flow approach (right).	62
3.3	Schematic representation of the three main types of failures in the Particle Flow Calorimetry.	63
3.4	The cone clustering algorithm explained [69].	63
3.5	Some clear recurring topologies [69].	64
3.6	Fragment removal examples [69].	64
3.7	Jet reconstruction efficiency versus transverse momentum (top) and pseudorapidity (bottom).	67
3.8	Distribution of the variable $\Delta p_T/p_{T_{MC}}$ in the <i>MC-jet</i> transverse momentum region [140, 180] GeV (top) and <i>MC-jet</i> pseudorapidity region [1.6, 2.0] (bottom). The gaussian fit is overlaid in red.	68
3.9	Distribution of the variable $\Delta E/E_{MC}$ in the <i>MC-jet</i> transverse momentum region [140, 180] GeV (left) and <i>MC-jet</i> pseudorapidity region [1.6, 2.0] (right). The gaussian fit is overlaid in red.	69
3.10	Jet transverse momentum resolution versus transverse momentum (top) and pseudorapidity (bottom).	70
3.11	Jet energy resolution versus transverse momentum (top) and pseudorapidity (bottom).	71

3.12	Lorentz factor for c hadrons in the $H \rightarrow c\bar{c}$ sample (left) and b hadrons in the $H \rightarrow b\bar{b}$ (right) at $\sqrt{s} = 1.5$ TeV.	72
3.13	Distance from the IP of b hadron and c hadron decay points in the $H \rightarrow c\bar{c}$ sample (red) and in the $H \rightarrow b\bar{b}$ (blue) at $\sqrt{s} = 1.5$ TeV.	73
3.14	Number of tracks wrongly associated to PV per event (left) and number of tracks wrongly associated to SV per event (right) in the $H \rightarrow c\bar{c}$ (red) and $H \rightarrow b\bar{b}$ (blue) samples.	74
3.15	Number of SVs reconstructed per jet (left) and corrected mass for SVs matched with a jet (right) in the $H \rightarrow c\bar{c}$ (red) and $H \rightarrow b\bar{b}$ (blue) samples.	74
3.16	Flight distance (left) and flight distance significance (right) for SVs matched with a jet in the $H \rightarrow c\bar{c}$ sample (red) and in the $H \rightarrow b\bar{b}$ (blue).	75
3.17	Longitudinal impact parameter (left) and transverse impact parameter (right) for the two types of tracks.	78
3.18	Uncertainty on D_0 (left) and Z_0 (right) for the two types of tracks.	78
3.19	D_0 - Z_0 significance (left) and transverse momentum (right) for the two types of tracks selected as described in this paragraph.	79
4.1	Illustration of a heavy-flavour jet with a secondary vertex (SV) from a decay of b/c hadron resulting in displaced tracks (including possibly a soft lepton). The displaced tracks are characterized by a large impact parameter with respect to the primary interaction vertex (PV), while the SV is characterized by a certain sizeable flight distance with respect to PV.	83
4.2	Illustration of the difference between primary tracks and tracks from a SV in terms of Signed Impact Parameter.	84
4.3	Distribution of the 3D SIP significance of the first track, for the three different flavours of jet. Histograms are normalized to unit area. The first and last bin include the underflow and overflow entries, respectively.	85
4.4	Distribution of the 3D SIP significance of the second track, for the three different flavours of jet. Histograms are normalized to unit area. The first and last bin include the underflow and overflow entries, respectively.	85
4.5	Transverse momentum of the first track with respect to the jet axis for different jet flavour samples. Histograms are normalized to unit area. The last bin include the overflow entries.	86
4.6	2D SIP significance of the first track above the invariant mass threshold, for different jet flavour samples. Histograms are normalized to unit area. The first and last bin include the underflow and overflow entries, respectively.	87
4.7	Corrected mass of the first SV. Histograms are normalized to unit area. The last bin includes the overflow entries.	88
4.8	3D flight distance significance of the first SV. Histograms are normalized to unit area. The last bin includes the overflow entries.	89

4.9	Boost of the first SV. Histograms are normalized to unit area.	89
4.10	Mass-energy fraction of the first SV. Histograms are normalized to unit area.	90
4.11	p_T of the first lepton divided by jet p_T . Histograms are normalized to unit area. The last bin includes the overflow entries.	91
4.12	p_T of the first lepton with respect to the jet axis. Histograms are normalized to unit area. The last bin includes the overflow entries.	91
4.13	Jet fraction per vertex category.	92
4.14	Jet fraction per lepton category.	93
4.15	BDT score for CvsB (left) and CvsL (right) discriminators. Training and test distributions are overlaid to look for eventual overtraining issues.	96
4.16	Distribution of the CvsB (left) and CvsL (right) discriminator scores for jets of different flavours in simulated events described in Table 5.1. Histograms are normalized to unit area.	96
4.17	Efficiency for b, c and light jets versus discriminator cut, for CvsB and CvsL.	97
4.18	Misidentification probability for b jets (left) and light-flavour jets (right) versus c jet identification efficiency.	97
4.19	Misidentification probability for light-flavour jets versus misidentification probability for b jets for several constant c jet efficiencies. .	98
5.1	Number of jet per event, invariant mass of the Higgs candidate, jet pseudorapidity, jet energy, jet transverse momentum and di-jet separation, for the samples $H \rightarrow b\bar{b}$, $H \rightarrow c\bar{c}$ and $H \rightarrow gg$. For the kinematic variable plots only the jets used to form the Higgs candidate are included. No further selections are applied. Distributions are normalized to unit area.	102
5.2	Correlation between CvsL and CvsB taggers for the different jet flavours, with a star indicating the chosen working point.	103
5.3	C tagging efficiency (left) and misidentification probability for b jets (left) as a function of the jet transverse momentum. The working point for CvsB is fixed at 0.	103
5.4	C tagging efficiency (left) and misidentification probability for light-flavour jets (left) as a function of the jet transverse momentum. The working point for CvsL is fixed at 0.04.	104
5.5	From top to bottom: energy, transverse momentum, ΔR and invariant mass of the di-jet system for all the samples after flavour tagging. Histograms are scaled to cross section and luminosity. .	107
A.1	The number of secondary vertices (left) and the number of tracks associated with the first SV (right) for jets in the RecoVertex category.	116
A.2	The 2D flight distance significance (left) and the energy ratio (right) of the first SV for jets in the RecoVertex category.	116
A.3	The ΔR between the first SV and the jet axis for jets in the RecoVertex category (left) and the ΔR between the first track and the jet axis (right).	117

A.4	The ΔR between the summed four-momentum vector of the tracks and the jet axis (left) and the number of tracks associated with the jet (right).	117
A.5	The 2D SIP significance of the first two tracks.	117
A.6	The 3D SIP significance of the first track that raises the combined invariant mass of the tracks above 1.5 GeV (left) and the transverse energy of the total summed four-momentum vector of the selected tracks divided by the transverse energy of the jet (right).	118
A.7	The track momentum parallel to the jet direction (left) and the track momentum parallel to the jet direction divided by the magnitude of the track momentum vector (right), for the first track.	118
A.8	The track p_T relative to the jet axis divided by the magnitude of the track momentum vector, for the first track (left) and the first lepton momentum parallel to the jet direction divided by the magnitude of the jet momentum, for jets in the SoftMuon or SoftElectron category (right).	118
B.1	Illustration of a Decision Tree. The rectangular boxes contain the cuts applied on the features(x_i , x_j and x_k), the circles represent nodes and the terminal ones contain the label S for signal and B for background.	120

List of Tables

1.1	The branching ratios and the relative uncertainty for a SM Higgs boson with $m_H = 125$ GeV [3].	26
1.2	Summary of the Future Colliders considered in this section. The operative center of mass energy \sqrt{s} , the instantaneous \mathcal{L}_{inst} and integrated \mathcal{L} luminosity and data taking years are reported [2]. . .	32
1.3	Expected relative precision (%) of the κ parameters in the scenario with no BSM Higgs width, for future accelerators[2]. Cases in which a particular parameter has been fixed to the SM value due to lack of sensitivity are shown with a dash (-). A star \star indicates the cases in which a parameter has been left free in the fit due to lack of input in the documentation. <i>FCC-ee/eh/hh</i> corresponds to the combined performance of FCC-ee at 240 and 365 GeV, FCC-eh and FCC-hh. In the case of HE-LHC, two theoretical uncertainty scenarios, S2 and S2', are given, with S2' theoretical uncertainty reduced by a factor two with respect to S2.	34
1.4	Working hypothesis for the Muon Collider [27].	35
1.5	Relative precision on Higgs boson coupling to b quark at Muon Collider [31] and at CLIC [32].	37
2.1	Main parameters of the MAP proton driver muon facility working at different center of mass energies.	41
2.2	VTX barrel (top) and VTX endcap (bottom) layer geometrical characteristics [46].	46
2.3	IT barrel (top) and IT endcap (bottom) layer geometrical characteristics [46].	46
2.4	OT barrel (top) and OT endcap (bottom) layer geometrical characteristics [46].	47
2.5	Cell dimensions and resolutions for the three sub-detectors making up the tracker system.	47
2.6	ECAL and HCAL dimensions in the barrel region. Absorber and sensor materials employed are also reported [46].	48
2.7	ECAL and HCAL dimensions in the endcap region. The HCAL ring connects the endcap to the barrel section, providing a good coverage in the transition region. Absorber and sensor materials employed are also reported [46].	48

2.8	Expected average number of muon decays per meter and estimated number of background particles entering the detector per bunch crossing. In parentheses the thresholds set on the particle kinetic energy in simulation (MARS code used [45]) are shown [48].	51
3.1	Overview of the pattern recognition steps and parameters. VTX stands for Vertex Detector, B for Barrel and E for Endcap. I-L and O-L are respectively the Inner and Outer layers of the Vertex Detectors.	61
3.2	Parameters set in the PV and SV finder.	77
3.3	Track selection for PV and SV finding. VTX stands for vertex detector, considering both the barrel and the endcap portion.	79
3.4	The performance of the LCFIPplus vertex finder evaluated on a sample of $H \rightarrow b\bar{b}$ at Muon Collider at $\sqrt{s} = 1.5 \text{ TeV}$	80
3.5	The performance of the LCFIPplus vertex finder evaluated on a sample of $H \rightarrow c\bar{c}$ at Muon Collider at $\sqrt{s} = 1.5 \text{ TeV}$	80
3.6	The performance of the LCFIPplus vertex finder evaluated on a sample of $b\bar{b}$ events at $\sqrt{s} = 91.2 \text{ GeV}$ at ILC	81
4.1	Basic quality requirements for reconstructed objects. VTX stands for vertex detector, considering both the barrel and the endcap portion.	92
4.2	BDT parameters and number of signal and background events for the training procedure of CvsB and CvsL. An explanation of the parameters can be found in Appendix B.	95
4.3	P-values returned by the K-S test are reported for Signal and Background distributions independently, for both CvsB and CvsL tagger.	96
4.4	Beauty and light-flavour contamination for fixed values of c tagging efficiencies at Muon Collider (w/o BIB), CMS and CLIC (w/o overlay).	98
5.1	Table summarizing the sample produced for the analysis. It reports the simulated physics processes, the estimated cross sections, the number of simulated events, the cuts imposed at generator level and the generator used. All samples are produced at $\sqrt{s} = 1.5 \text{ TeV}$	101
5.2	Number of jets for each process before and after the tagger application. The tagger efficiency is reported.	104
5.3	Number of events with at least two jets for each process before and after the tagger application. The selection efficiency is reported.	104
5.4	Number of scaled events after each cut, together with the relative efficiencies.	108
5.5	Number of surviving events (normalized to cross section and luminosity) in the Higgs region after all selections. The absolute efficiencies are reported. The unreported processes are completely rejected by the cuts.	109

5.6	Signal and background yields, signal significance, uncertainty on $H \rightarrow c\bar{c}$ production cross section and uncertainty on the Hcc coupling at 1.5 TeV, 500 fb^{-1} integrated luminosity, without BIB overlay.	111
5.7	Projected signal and background yields, signal significance, uncertainty on $H \rightarrow c\bar{c}$ production cross section and uncertainty on the Hcc coupling at 3 TeV, 1300 fb^{-1} integrated luminosity, without BIB overlay.	111
5.8	Relative precisions on the Hcc coupling at CLIC, for different energies and integrated luminosities. Each new stage at increased energy includes all measurements of the previous stages.	111

Introduction

The highest scientific priorities identified in the update of the European Strategy for Particle Physics [1] are the study of the Higgs boson and the exploration of the high-energy frontier. These are two crucial and complementary ways to address the open questions in Particle Physics.

In this perspective, a multi-TeV ($\sqrt{s} = 1.5 - 30 \text{ TeV}$) muon collider providing $O(ab^{-1})$ integrated luminosity has been proposed. It offers several advantages with respect to the traditional hadronic and e^+e^- machines, but, at the same time, it poses some new technical challenges, as the mitigation of the background produced by the decay of muons in the beams.

A muon collider would have a discovery machine potential as well as the opportunity to measure precisely the Higgs couplings to several Standard Model (SM) particles and the Higgs self-couplings. The study of the Higgs boson couplings to the second generation of fermions is especially challenging because of the small branching ratio. The coupling to the c quark, in particular, is still out of reach experimentally and it will not be accessible even at the next to come High Luminosity LHC [2].

In this thesis I have explored, for the first time, the search for $H \rightarrow c\bar{c}$ at a Muon Collider experiment, at a center of mass energy of $\sqrt{s} = 1.5 \text{ TeV}$. The $\mu^+\mu^- \rightarrow H\nu\bar{\nu} \rightarrow c\bar{c}\nu\bar{\nu}$ signal process has been fully generated, simulated and reconstructed in the current detector design, along with the main physics backgrounds and without the machine background.

In order to improve rejection of jets coming from b quark and u-d-s-g hadronization, I have developed a c quark-tagging algorithm, combining several observables in a single discriminator using Machine Learning techniques.

Finally, a first estimate of the precision on the Higgs coupling to c quark achievable at the Muon Collider is presented at $\sqrt{s} = 1.5 \text{ TeV}$, considering four years of data taking. A projection to $\sqrt{s} = 3 \text{ TeV}$ is estimated, too, showing the improvement of sensitivity with increasing energy.

A presentation about this work has been accepted at the 9th Edition of the Large Hadron Collider Physics Conference, planned from 7th to 12th June 2021.

This thesis is structured in 5 chapters:

- **Chapter 1. Standard Model state of art and prospect**

An overview of jet and Higgs physics inside the SM framework is provided, along with a summary of the most recent experimental measure-

ments of Higgs Boson properties and couplings carried out at LHC. The expected sensitivities on Higgs boson couplings at Future Colliders are reported and the Muon Collider physics potential is addressed, comparing it with the more conventional hadron and e^+e^- colliders.

- **Chapter 2. Muon Collider machine and detector**

The schemes proposed for the muon production and acceleration are outlined, together with the new technical issues posed by such a novel and peculiar machine. Furthermore, the current detector geometry and detector components are described. Finally, the machine background is characterized and the main mitigation strategies under analysis are presented.

- **Chapter 3. Event reconstruction at Muon Collider**

The steps of the full event reconstruction are outlined. The algorithms used for track reconstruction, particle identification, jet clustering and secondary vertex finding are described in full detail. In particular, the secondary vertex finding algorithm was never employed at the Muon Collider before this work, thus a study for choosing the optimal algorithm parameters is performed. In addition, the jet and secondary vertex reconstruction performances are evaluated and reported.

- **Chapter 4. The c jet identification**

A dedicated tagger for c jet identification is developed here for the first time at the Muon Collider. The discriminating variables used are shown and described in detail, together with the implemented algorithm.

Multivariate Analysis methods are employed to combine the variables into a single discriminator. Finally, the c tagger performance is evaluated.

- **Chapter 5. Analysis of $H \rightarrow c\bar{c}$**

The event generation for the signal process $\mu^+\mu^- \rightarrow H\nu\bar{\nu} \rightarrow c\bar{c}\nu\bar{\nu}$ and the physics backgrounds is described. The selections applied to reject the backgrounds are discussed and the final signal and background yields are used to estimate the relative uncertainty on the signal cross section and, consequently, the relative uncertainty on the precision of the Higgs boson coupling to c quark.

Chapter 1

Standard Model state of art and prospect

The Standard Model [3] is the mathematical framework that currently encapsulates our best understanding of nature's fundamental order. It offers a quantum-mechanical description of three out of four known fundamental forces: electromagnetic, weak and strong, leaving aside the gravitational one¹.

In Figure 1.1 the full list of the SM elementary particles is given. The summary table shows that the fundamental particles are classified in two categories according to their intrinsic angular momentum, the *spin*:

- **Bosons** are particles with integer spin values, that follow Bose-Einstein statistics. The carriers of the aforementioned fundamental forces belong to this category.
- **Fermions** are particles with semi-integer spin values, that obey Fermi-Dirac statistics. The particles that constitute the observable matter belong to this category.

The SM is based on the observation of the fundamental symmetries of nature:

- $SU(3)_C$ symmetry characterizes the Quantum Chromodynamics (QCD), the theory that describes strong interactions between the matter particles called *quarks* through the exchange of force-carriers called *gluons*.
- $U(1)_{em}$ symmetry is at the basis of the Quantum Electrodynamics (QED), the theory that explains the electromagnetic interactions between all particles endowed with electric charge. This interactions are mediated by *photons* and affect quarks as well as the other type of matter particle existing in nature, the so-called *leptons* (neutrinos excluded because of the zero charge).
- $SU(2)_L \times U(1)_Y$ symmetry characterizes the unified theory of electromagnetic and weak interaction. The latter affects all particles in nature and is mediated by the W^\pm and Z bosons.

¹In this thesis, Natural Units are adopted: $c = \hbar = 1$, where $\hbar = h/2\pi = 6.58211889(26) \cdot 10^{-22} \text{ MeVs}$ and $c = 299792458 \text{ ms}^{-1}$

The framework is completed by the *Electroweak Symmetry Breaking* (EWSB) mechanism that accounts for the particle masses. The particle responsible for this phenomenon is the Higgs boson, a so far unique, fundamental scalar particle, whose existence was confirmed in 2012 when CMS [4] and ATLAS [5] jointly declared its discovery.

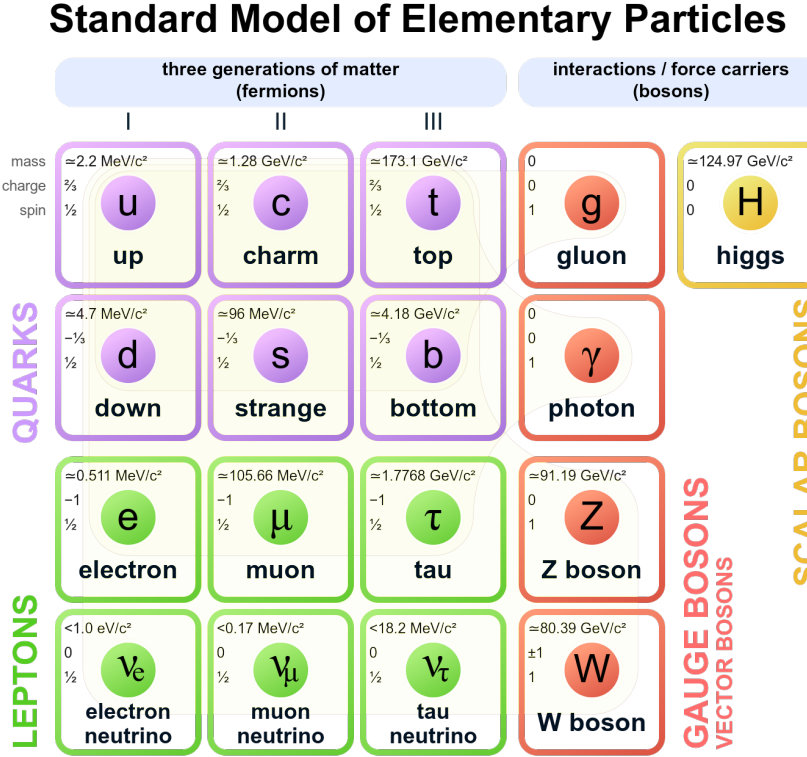


Figure 1.1: A summary table with all the SM particles: the fermions (on the left) are divided into quarks (in violet) and leptons (in green), while the bosons (on the right), are classified into gauge bosons, i.e. the carriers of the interactions (in red) and the scalar Higgs boson (in yellow). For each particle, the mass, electric charge and spin values are reported.

The first section of this chapter shortly outlines the basics of QCD and jet formation. All other sections are dedicated to the Higgs Boson physics: the theory within the SM, the status of observations at LHC and the prospect at future colliders.

1.1 Basics of QCD and jet physics

QCD [6] describes the building blocks of strongly interacting particle, the *hadrons*, and the forces acting between them. The fundamental constituents of these particles are the spin-1/2 *quarks*, which come in six types (or *flavours*) divided in three generations (see Figure 1.1). Their masses cover a large range: the three lightest quarks u , d , s weigh only a small fraction of the proton mass ($m_{\text{proton}} \simeq 938 \text{ MeV}$), the charm quark c just about the proton mass while

the two heavy quarks b , t weigh respectively more than 4 and 180 times the proton mass.

Each quark flavour can be characterized by three different values of a quantum number, called *color*. Nonetheless, in nature only colorless states are observed, which means that hadrons are non-colored bound states of quarks. Rephrased within the $SU(3)_C$ symmetry group, hadrons are singlets under rotations in the color space. So far, observed hadrons are composed either of a colorless quark-antiquark pair ($q\bar{q}$), in this case they are referred to as *mesons*, or of a colorless triplet of quarks (qqq), in this case they are called *baryons*.

Quarks interact via force mediators called *gluons*. Eight such gluon fields g are predicted by the non-abelian gauge group $SU(3)_C$. Like the photon field in Quantum Electrodynamics (QED), they are vector fields with spin = 1, but, differently from photon, they carry color charges themselves, mediating color flips of quarks by absorption or emission. The main fundamental consequence of this property is that gluons can interact with each other, while photons cannot. Such a dissimilarity leads QCD to be profoundly different from QED. Because of the gluon self coupling, QCD vacuum consists not only of virtual quark pairs ($q\bar{q}$) but it is also filled with virtual gluon pairs, as illustrated in Figure 1.2. The polarizing effect due to quark pairs is similar to the QED one², while gluons have an opposite effect of antiscreening.

Overall the effective color charge becomes larger with larger distance.

Charge screening in QCD leads to the concept of *running coupling constants*. At short distance (large momentum transfer) the strong coupling decreases such that quarks can be considerate approximately as free particles. This property is called *asymptotic freedom* and allows the usage of perturbation theory in calculations, in order to produce quantitative predictions for hard scattering cross sections in hadronic interactions. Conversely, at increasing distance the coupling becomes so strong that it is impossible to isolate a quark from a hadron. This mechanism is called *confinement* and explains why in nature only colorless bound states of quarks are observed.

The strong coupling constant α_S can be approximately parametrized with the following formula:

$$\alpha_S(Q^2) \approx \frac{1}{\beta_0 \ln \left(\frac{Q^2}{\Lambda^2} \right)} \quad (1.1)$$

where β_0 is a constant first computed by Wilczek, Gross [7] and Politzer [8], and the quantity Λ is called *QCD scale* and is indicative of the energy range where non-perturbative dynamics dominates. Figure 1.3 [3] reports experimental results for α_S as a function of the momentum transfer, obtained with different techniques. The word average value of α_S at the energy scale of the Z boson is also quoted.

²In QED the *vacuum polarization* leads to a screening effect of the charge, which appears smaller with increasing distance of the probe, i.e. with decreasing transferred four-momentum between the charge and the probe.

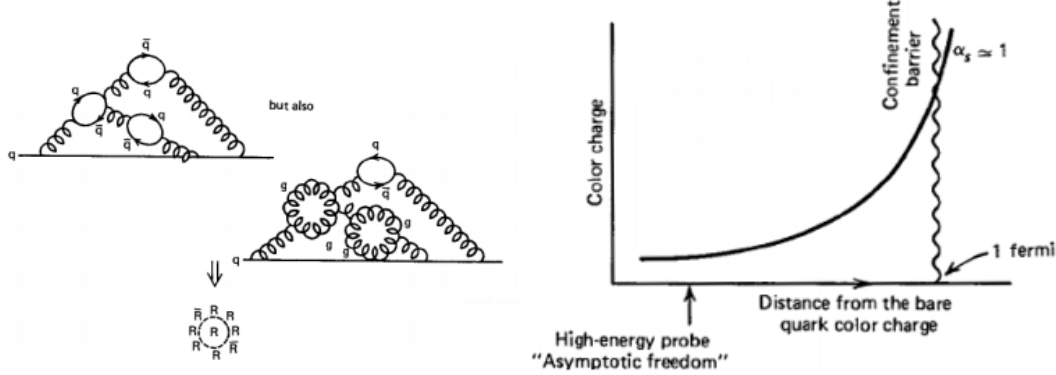


Figure 1.2: Illustration of the antiscreen effect in QCD (left) and of an approximate behaviour of the effective color charge versus the distance from the bare color charge (right). The distance r can be equivalently expressed in terms of the transferred four-momentum Q^2 between the charge and the probe, since $r \simeq 1/Q^2$.

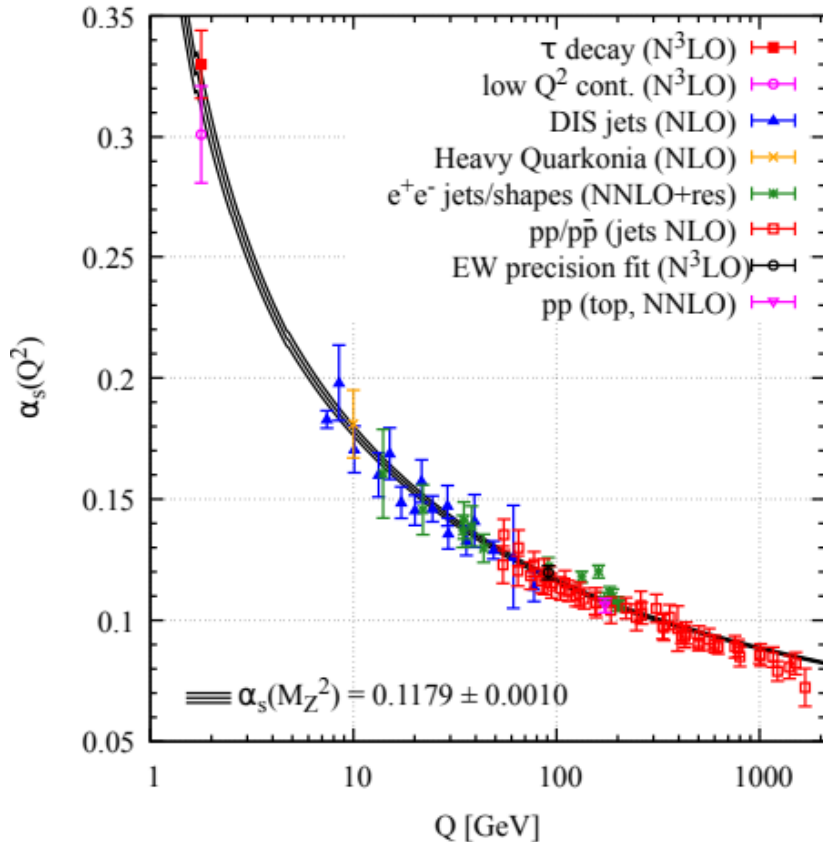


Figure 1.3: Summary of measurements of α_s as a function of the energy scale Q . The respective degree of QCD perturbation theory used in the extraction of α_s is indicated in brackets (NLO: next-to-leading order; NNLO: next-to-next-to-leading order; NNLO+res.: NNLO matched to a resummed calculation; N3LO: next-to-NNLO).

Let us consider a scattering process that has quarks in the final state, as the $\mu^+\mu^-$ annihilation to hadrons, $\mu^+\mu^- \rightarrow q\bar{q}, q\bar{q}g, \dots$, in Figure 1.4.

Due to asymptotic freedom of QCD, quarks and gluons move as quasi-free particles at short distances. When these coloured objects separate more than 1 fm (order of magnitude), confinement forces become effective and bind the quarks and gluons in hadrons, in a process called *hadronization*. The hadronization proceeds through the formation of jets of highly collimated particles which is driven by two dynamical mechanisms:

1. Quarks, which are suddenly accelerated in the production process, at short distance and time of the order of $1/E \ll 1 \text{ fm}$, radiates gluons preferentially into a cone of small opening angle Θ , $dN/d\Theta^2 \sim 1/\Theta^2$. Subsequently the gluons may split into two gluons or quark-antiquark pairs, and, repeatedly, quarks and gluons again into quark and gluon pairs, so that the original quark fragments comprehensively into a quark/gluon cascade within a narrow cone.
2. When the coloured quarks, on the way out of the femto-universe to large distances, separate to more than 1 fm, a gluonic flux tube of narrow transverse dimensions builds up and fragments into ordinary hadrons.

Similar mechanisms lead to the hadronization of gluons.

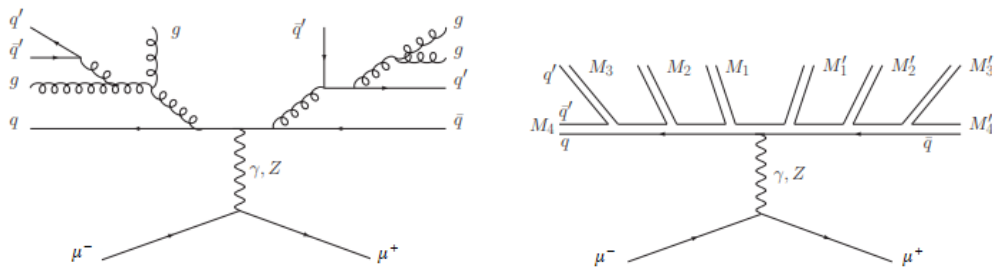


Figure 1.4: Quark/gluon cascades (left) and fragmentation to hadrons induced by confinement forces (right), in $\mu^+\mu^-$ annihilation.

Overall, the perturbative quark/gluon cascade and the non-perturbatively fragmentation into hadrons generate jets of particles preserving, in momentum and energy, the original kinematic characteristics of their parent.

Since jets are the final physical objects that can be observed experimentally, through their analysis it is possible to determine the properties of quarks and gluons, such as their spins, flavour and colour charges as well as their basic interactions. Figure 1.5 shows an event with four jets in the Muon Collider detector: they are visible as clusters of many hits in subsequent detectors, that appear to be approximately collimated in an unique direction.

In this work processes with jets in the final state are considered. The focus is particularly on jets initiated by c quark (signal signature) and b quark (background signature). Moreover, properties of hadrons containing b or c quarks (collectively called *heavy hadrons*) are studied in detail. In literature, hadrons containing at least a b quark are referred to as *b hadrons* or *bottom hadrons*, while hadrons containing at least a c quark (and no b quark) are called *c hadrons* or *charm hadrons*.

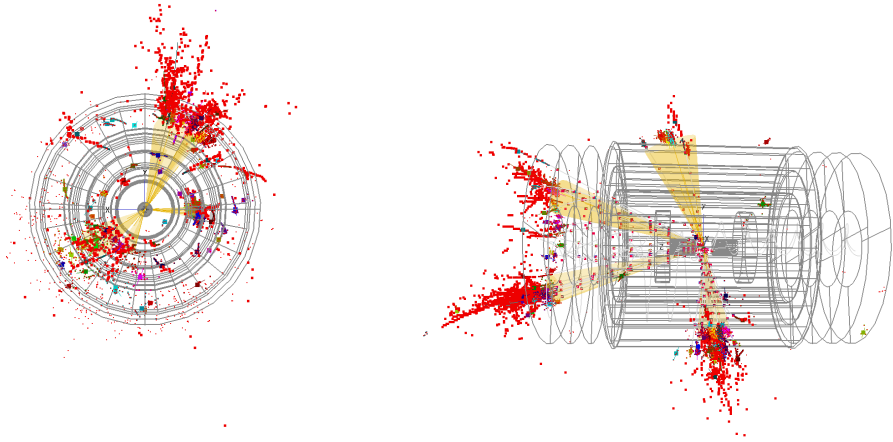


Figure 1.5: Four jet event in the Muon Collider detector: front view (left) and lateral view (right).

1.2 Higgs Boson in the Standard Model

In the SM, the electroweak interactions [3] [9] (the unified description of weak and electromagnetic force) are described by a gauge field theory invariant under the $SU(2)_L \times U(1)_Y$ symmetry group. Four vector gauge fields are associated to this local symmetry group: three W_μ (W_μ^1 , W_μ^2 and the neutral W_μ^3) and the neutral B_μ . These fields are related to the physical W^\pm and Z bosons and to the photon A through the following relations:

$$\begin{aligned} W_\mu^+ &= \frac{W^1 - iW^2}{\sqrt{2}} & Z_\mu &= -\sin \theta_W B_\mu + \cos \theta_W W_\mu^3 \\ W_\mu^- &= \frac{W^1 + iW^2}{\sqrt{2}} & A_\mu &= +\sin \theta_W W_\mu^3 + \cos \theta_W B_\mu \end{aligned} \quad (1.2)$$

where θ_W is known as the Weinberg angle, or the weak mixing angle, and is an unfixed parameter of the theory.

The mechanism of EWSB provides a general framework to keep untouched the structure of the electroweak gauge interactions at high energies and still generate the observed masses of the W and Z gauge bosons, making the weak interactions short ranged.

The EWSB mechanism introduces a self-interacting complex EW doublet scalar field with $Y_H = \frac{1}{2}$ hypercharge, Φ :

$$\Phi = \frac{1}{\sqrt{2}} \begin{pmatrix} \phi_1 + i\phi_2 \\ \phi_3 + i\phi_4 \end{pmatrix} \quad (1.3)$$

where $\phi_1, \phi_2, \phi_3, \phi_4$ are real scalar fields. The SM scalar potential reads:

$$V(\Phi) = m^2 \Phi^\dagger \Phi + \lambda (\Phi^\dagger \Phi)^2 \quad (1.4)$$

where m^2 and λ are real constants related to the shape of the Higgs potential. $\lambda > 0$ is required to ensure the presence of a ground state, while $m^2 < 0$ implies that this ground state is infinitely degenerate. The choice of a particular

ground state induces the spontaneous breaking of the SM gauge symmetry $SU(2)_L \times U(1)_Y$ into $U(1)_{em}$.

From the four generators of the $SU(2)_L \times U(1)_Y$ SM gauge group, three are spontaneously broken, leading to the existence of three massless Goldstone bosons identified with three of the four Higgs field degrees of freedom. The three Goldstone bosons are absorbed to give masses to the W and Z gauge bosons. The last degree of freedom gives rise to an excitation mode of the field Φ above its ground state, i.e. the physical Higgs boson. It is possible, in fact, to write Φ as:

$$\Phi = \frac{1}{\sqrt{2}} \begin{pmatrix} 0 \\ v + h(x) \end{pmatrix} \quad (1.5)$$

with:

$$v = \sqrt{\frac{-m^2}{\lambda}} \quad (1.6)$$

where v is the vacuum expectation value ($v \approx 246 \text{ GeV}$, it sets the scale of the symmetry breaking) and $h(x)$ is the Higgs field.

The Higgs field couples to the three W_μ gauge fields and to the B_μ gauge field through the covariant derivative appearing in the kinetic term of the Higgs Lagrangian:

$$\mathcal{L}_{Higgs} = (D_\mu \Phi)^\dagger (D^\mu \Phi) - V(\Phi) \quad (1.7)$$

with the covariant derivative defined as:

$$D_\mu = \partial_\mu + ig \frac{\sigma^a}{2} W_\mu^a + ig' Y_H B_\mu \quad (1.8)$$

where g and g' are respectively the $SU(2)_L$ and $U(1)_Y$ gauge couplings and σ^a , $a = 1, 2, 3$ are the three Pauli matrices.

Let's consider the vacuum state:

$$\Phi \equiv \Phi^0 = \frac{1}{\sqrt{2}} \begin{pmatrix} 0 \\ v \end{pmatrix} \quad (1.9)$$

By substituting 1.9 in the Higgs lagrangian 1.7 and considering the definitions in 1.2, it is possible to demonstrate that the W^\pm and Z bosons acquire masses whose values are given by the following expressions:

$$m_W^2 = \frac{g^2 v^2}{4} , \quad m_Z^2 = \frac{(g'^2 + g^2)v^2}{4} \quad (1.10)$$

Thus, EW theory predicts boson masses only as a function of fundamental parameters (g , g' and v). The same holds for fermion masses, as it will be clear later in the paragraph.

Since the gauge couplings g and g' can be expressed in terms of the elementary charge e and the Weinberg angle θ_W :

$$g = \frac{e}{\sin \theta_W} \quad g' = \frac{e}{\cos \theta_W} \quad (1.11)$$

The two masses are not independent but the following relation holds:

$$\left(\frac{m_Z}{m_W}\right)^2 = \frac{g^2 + g'^2}{g^2} = \frac{1}{\cos^2 \theta_W} \quad (1.12)$$

The W, Z bosons were discovered by UA1 and UA2 experiments and later their masses were accurately measured by experiments at LEP, Tevatron and LHC. The average values of these measurements are [3]:

$$m_W = 80.379 \pm 0.012 \text{ GeV} \quad m_Z = 91.1876 \pm 0.0021 \text{ GeV} \quad (1.13)$$

The value of the Weinberg angle is then:

$$\sin^2 \theta_W = 1 - \left(\frac{m_Z}{m_W}\right)^2 = 0.22337 \pm 0.00010 \quad (1.14)$$

The unbroken generator of the $SU(2)_L \times U(1)_Y$ symmetry is the one associated to the $U(1)_{em}$ conserved gauge symmetry. Its corresponding gauge field, the photon, remains massless. Similarly the eight color gauge bosons, the gluons, corresponding to the conserved $SU(3)_C$ gauge symmetry with 8 unbroken generators, also remain massless. As a consequence, the Higgs boson is neutral under the electromagnetic interactions and transforms as a singlet under $SU(3)_C$ and hence does not couple at tree level to the massless photons and gluons.

Higgs boson can interact with itself, as expressed by the potential in Eq. 1.4. The Higgs mass can be evaluated as function of theory parameters by substituting the field expression in Eq. 1.5 into the potential formula. In this way the mass results to be:

$$m_H = \sqrt{2\lambda}v \quad (1.15)$$

where v is fixed by the Fermi coupling constant $\left(v = (\sqrt{2}G_F)^{-1/2}\right)$ and λ is the self coupling parameter in $V(\Phi)$.

The quartic coupling λ is a free parameter in the SM, and hence, there is no a priori prediction for the Higgs mass. Moreover the sign of the mass parameter in $V(\Phi)$, $m^2 = -\lambda v^2$, has to be negative for the EW symmetry breaking to take place, but there is no a priori understanding of what decides of this sign. The experimentally measured Higgs boson mass is [3]:

$$m_H = 125.10 \pm 0.14 \text{ GeV} \quad (1.16)$$

and it implies that

$$\lambda \simeq 0.13 \quad \text{and} \quad |m| \simeq 88.4 \text{ GeV} \quad (1.17)$$

Finally, the Higgs boson interacts also with fermions (quarks and leptons), as expressed by the Yukawa lagrangian:

$$\begin{aligned} \mathcal{L}_{Yuk} = & \left\{ - (\bar{e}_R \quad \bar{\mu}_R \quad \bar{\tau}_R) \begin{pmatrix} c_e & 0 & 0 \\ 0 & c_\mu & 0 \\ 0 & 0 & c_\tau \end{pmatrix} \begin{pmatrix} e_L \\ \mu_L \\ \tau_L \end{pmatrix} \right. \\ & - (\bar{u}_R \quad \bar{c}_R \quad \bar{t}_R) \begin{pmatrix} c_u & 0 & 0 \\ 0 & c_c & 0 \\ 0 & 0 & c_t \end{pmatrix} \begin{pmatrix} u_L \\ c_L \\ t_L \end{pmatrix} \\ & \left. - (\bar{d}'_R \quad \bar{s}'_R \quad \bar{b}'_R) \mathbf{V} \begin{pmatrix} c_d & 0 & 0 \\ 0 & c_s & 0 \\ 0 & 0 & c_b \end{pmatrix} \mathbf{V}^\dagger \begin{pmatrix} d'_L \\ s'_L \\ b'_L \end{pmatrix} + h.c. \right\} \frac{(v + h(x))}{\sqrt{2}} \end{aligned} \quad (1.18)$$

where the subscripts L and R specify the left-hand and the right-hand components of the matter fields, c_e, c_μ, \dots, c_b are the coupling constants, and the \mathbf{V} is the *Cabibbo-Kobayashi-Maskawa matrix*. The \mathbf{V} matrix rotates the mass eigenstates $(d \ s \ t)$ into the weak isospin eigenstates $(d' \ s' \ t')$:

$$\begin{pmatrix} d' \\ s' \\ b' \end{pmatrix} = \mathbf{V} \begin{pmatrix} d \\ s \\ b \end{pmatrix} = \begin{pmatrix} V_{ud} & V_{us} & V_{ub} \\ V_{cd} & V_{cs} & V_{cb} \\ V_{td} & V_{ts} & V_{tb} \end{pmatrix} \begin{pmatrix} d \\ s \\ b \end{pmatrix} \quad (1.19)$$

It is a unitary matrix and it can be parametrized in terms of three angles and one complex phase, which accounts for the CP violation in weak interactions. By looking at Eq. 1.18, the masses of the fermions can be immediately identified as:

$$m_e = c_e \frac{v}{\sqrt{2}}, \dots, m_b = c_b \frac{v}{\sqrt{2}} \quad (1.20)$$

Summing up the theory predictions, the Higgs boson couplings to the fundamental particles are set by their masses. This is a new type of interaction: very weak for light particles, such as up and down quarks, and electrons, but strong for heavy particles such as the W and Z bosons and the top quark. More precisely, the SM Higgs couplings to fundamental fermions are linearly proportional to the fermion masses, whereas the couplings to bosons are proportional to the square of the boson masses. The following lagrangian summarises the SM Higgs boson couplings and self-couplings:

$$\mathcal{L} = -g_{Hf\bar{f}} f \bar{f} H + \frac{g_{3H}}{6} H^3 + \frac{g_{4H}}{24} H^4 + \delta_V V_\mu V^\mu \left(g_{HVV} H + \frac{g_{HHVV}}{2} H^2 \right) \quad (1.21)$$

with

$$g_{Hf\bar{f}} = \frac{m_f}{v}, \quad g_{HVV} = \frac{2m_V^2}{v}, \quad g_{HHVV} = \frac{2m_V^2}{v^2}, \quad g_{3H} = \frac{3m_H^2}{v}, \quad g_{4H} = \frac{3m_H^2}{v^2} \quad (1.22)$$

where $V = W^\pm$ or Z and $\delta_W = 1, \delta_Z = 1/2$.

As a result, the dominant mechanisms for Higgs boson production and decay involve the coupling of H to W, Z and/or the third generation quarks and leptons. The coupling to gluons is induced at leading order by a one-loop process

in which H couples to a virtual $t\bar{t}$ pair, while the coupling to photon proceeds via the one-loop graph with a virtual W^+W^- pair with a smaller contribution from $t\bar{t}$ pair.

In all observed production and decay modes measured so far, the rates and differential measurements are found to be consistent, within experimental and theoretical uncertainties, with the SM predictions (see section 1.3 for updated results at LHC). Nevertheless, several channels are still out of reach experimentally (because of the small Branching Ratio) and the couplings of the Higgs boson to light fermions are yet to be proven, as well as the Higgs self-interaction (see section 1.4 for future collider potential). Moreover, within the current precision, a more complex sector with additional states is not ruled out, nor it has been established whether the Higgs boson is an elementary particle or whether it has an internal structure like any other scalar particles observed before it.

Many unresolved problems within the SM are or can be related to Higgs Boson physics. One of these is the naturalness or hierarchy problem: the Higgs boson mass is affected by the presence of heavy particles and receives quantum corrections which destabilise the weak scale barring a large fine tuning of unrelated parameters. It has been the prime argument for expecting new physics right at the TeV scale. New theoretical paradigms have been imagined, such as a new fermion-boson symmetry called supersymmetry (SUSY) [10] or the existence of strong interactions at a scale of the order of a TeV from which the Higgs boson would emerge as a composite state [11].

Beyond the naturalness problem, extensions of the SM Higgs sector with additional scalars have been proposed, for example, to provide explanations for the fermion mass hierarchies [12], to account for the Dark Matter abundance [13] or to modify the properties of the electroweak phase transition [14].

For these and other more reasons the Higgs boson is considered a powerful tool to explore the manifestations of the SM and to probe the physics landscape beyond it.

1.3 Status of Higgs Boson Physics at LHC

The main production mechanism for the Higgs Boson at the LHC are (see Figure 1.6):

- *Gluon fusion* (ggF), $gg \rightarrow H + X$ (see diagram (a) in Figure 1.6). Since no direct gluon-Higgs coupling exists within the Standard Model, the process is mediated by the exchange of a virtual, heavy top quark. Contributions from lighter quarks propagating in the loop are suppressed proportionally to m_q^2 . At high-energy hadron colliders, this mechanism has the largest cross section. At the current LHC center of mass energy (13 TeV), the cross section for this phenomenon is (at the next-to next-to next to leading order) $\sigma_{ggF}^{N3LO} \approx 48.6 \text{ pb}$.
- *Vector-boson fusion* (VBF), $qq \rightarrow qqH$ (see diagram (b) in Figure 1.6). It's the second largest cross section at LHC. It proceeds by the scattering of two quarks, mediated by the exchange of a W or Z boson, with

the Higgs boson radiated off the weak-boson propagator. The scattered quarks give rise to two back-to-back hard jets in the forward and backward regions of the detector. The cross section of this process, in pp collisions at 13 TeV, is $\sigma_{VBF} \approx 3.78 pb$.

- *Higgs-strahlung* (VH), $q\bar{q} \rightarrow VH$ (see diagram (c) in Figure 1.6). It is a process of associated production with W or Z gauge bosons. In addition, for ZH production there is also a gluon-gluon induced contribution that involve top-quark loops, $gg \rightarrow VH$ (see diagram (d) in Figure 1.6). The cross sections of this processes, in pp collisions at 13 TeV, are $\sigma_{WH} \approx 1.37 pb$ and $\sigma_{ZH} \approx 0.88 pb$.
- *Associated production with $t\bar{t}$* ($t\bar{t}H$), $gg \rightarrow Ht\bar{t}$ (see diagram (e) in Figure 1.6). In this process, the Higgs boson radiates off top quarks, providing a direct probe of the top-Higgs Yukawa coupling. The cross section in pp collision at 13 TeV is $\sigma_{t\bar{t}H} \approx 0.50 pb$.

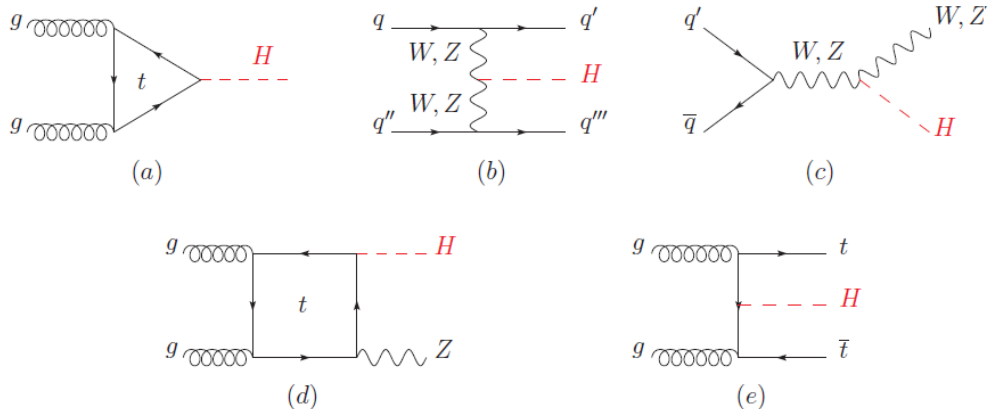


Figure 1.6: Main leading order Feynman diagrams contributing to the Higgs boson production in (a) gluon fusion, (b) Vector-boson fusion, (c) Higgs-strahlung (or associated production with a gauge boson at tree level from a quark-quark interaction), (d) associated production with a gauge boson (at loop level from a gluon-gluon interaction), (e) associated production with a pair of top quarks [3].

The main Higgs decay modes and their branching ratio (BR) are shown in Table 1.1. The dominant ones are $H \rightarrow b\bar{b}$ and $H \rightarrow WW^*$, followed by $H \rightarrow gg$, $H \rightarrow \tau^+\tau^-$, $H \rightarrow c\bar{c}$ and $H \rightarrow ZZ^*$. With much smaller rates the Higgs boson decays also into $H \rightarrow \gamma\gamma$, $H \rightarrow \gamma Z$ and $H \rightarrow \mu^+\mu^-$. The decays into gluons, diphotons and $Z\gamma$ are loop induced.

The Higgs boson decay into charm quarks, in particular, is the subject of this thesis, as the Higgs coupling to c quark, nowadays not accessible, can be measured in a future muon collider.

Figure 1.7 shows the cross section of different production mechanism versus the center of mass energy in pp collisions on the left, and the branching ratios of the main decays as a function of the Higgs boson mass on the right.

Decay channel	Branching ratio	Rel. uncertainty
$H \rightarrow \gamma\gamma$	2.27×10^{-3}	2.1%
$H \rightarrow ZZ$	2.62×10^{-2}	$\pm 1.5\%$
$H \rightarrow W^+W^-$	2.14×10^{-1}	$\pm 1.5\%$
$H \rightarrow \tau^+\tau^-$	6.27×10^{-2}	$\pm 1.6\%$
$H \rightarrow b\bar{b}$	5.82×10^{-1}	$+1.2\%$ -1.3%
$H \rightarrow c\bar{c}$	2.89×10^{-2}	$+5.5\%$ -2.0%
$H \rightarrow Z\gamma$	1.53×10^{-3}	$\pm 5.8\%$
$H \rightarrow \mu^+\mu^-$	2.18×10^{-4}	$\pm 1.7\%$

Table 1.1: The branching ratios and the relative uncertainty for a SM Higgs boson with $m_H = 125$ GeV [3].

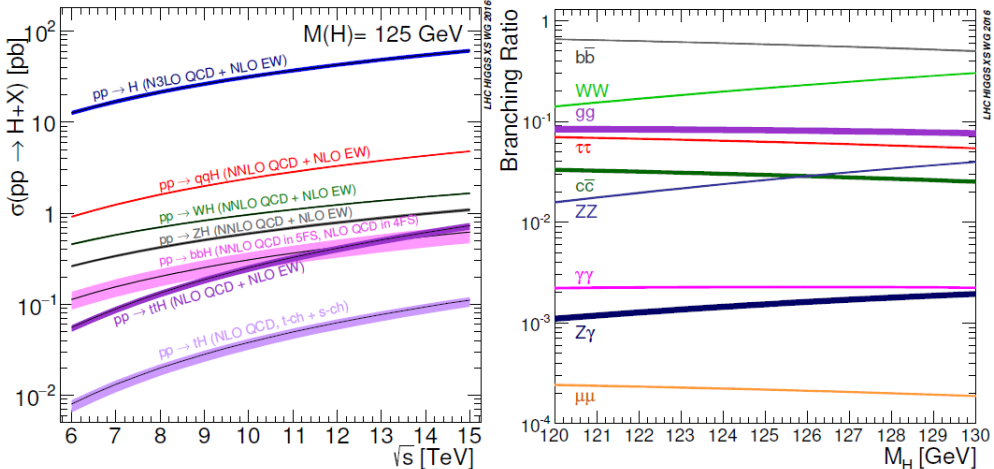


Figure 1.7: The SM Higgs boson production cross sections as a function of the center of mass energy for pp collisions (left) and the branching ratios for the main decays of the SM Higgs boson near $m_H = 125$ GeV (right). The VBF process is indicated here as qqH . The theoretical uncertainties are indicated as bands [3].

After the observation [5] [4] at LHC of a narrow resonance around 125 GeV in 2012, a detailed exploration of the Higgs boson properties started and took place in different runs of LHC at $\sqrt{s}=7, 8$ and 13 TeV. In particular, in the $H \rightarrow \gamma\gamma$ and $H \rightarrow ZZ^* \rightarrow 4l$ channels the reconstructed mass resolution is optimal (typically 1-2%) since all final state particles can be measured very precisely. The distribution of four-lepton and diphoton invariant masses with data collected during Run 2 at 13 TeV by CMS and ATLAS, are shown in Figure 1.8. The current estimate for the Higgs boson mass is $m_H = 125.10 \pm 0.14$ GeV.

As already observed, probing the Higgs couplings is of fundamental importance, in particular because Beyond SM (BSM) physics can largely change the

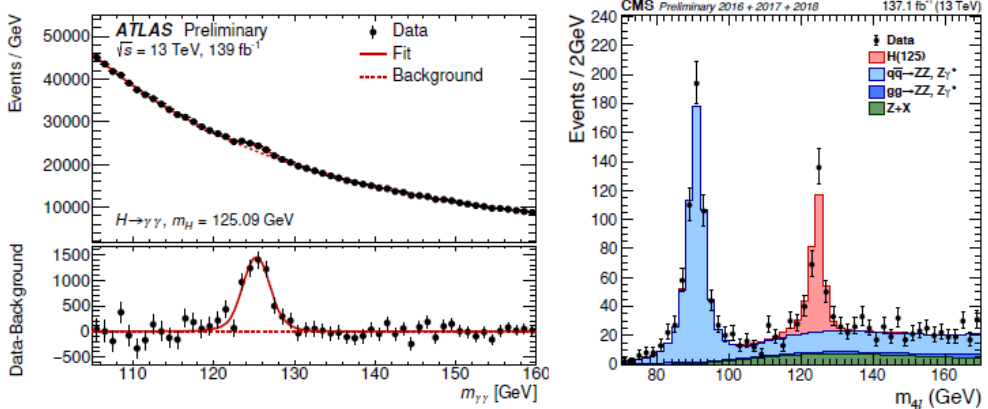


Figure 1.8: The invariant mass distribution of diphoton candidates observed by ATLAS at Run 2 (left). The residuals of the data with respect to the fitted background are displayed in the lower panel. The m_{4l} distribution from CMS Run 2 data (right)[3].

SM predictions. The discovery of the Higgs boson was made through bosonic final state, that probed mostly the couplings of the Higgs boson to vector bosons. One of the most prominent goals of LHC Run 2 was the direct observation of the Yukawa couplings of Higgs boson to the third generation fermions, i.e. bottom and top quarks and τ lepton. The coupling to bottom and τ is measured in decay, while the coupling to top is measured in the production of Higgs associated with top quarks.

In order to describe the characterization of the Higgs boson properties, the concept of signal strength must be introduced and the κ -framework must be outlined [15].

The signal strength modifier μ is defined as the ratio between the measured Higgs boson yield and its SM expectation. For a specific production and decay channel $i \rightarrow H \rightarrow f$, the signal strengths for the production μ_i and for the decay μ^f are defined as:

$$\mu_i = \frac{\sigma_i}{(\sigma_i)_{SM}}, \quad \mu^f = \frac{\mathcal{B}^f}{(\mathcal{B}^f)_{SM}} \quad (1.23)$$

Here σ_i ($i = ggH, VBF, VH$ or $t\bar{t}H$) and \mathcal{B}^f ($f = ZZ, W^+W^-, \gamma\gamma, \tau^+\tau^-$, $b\bar{b}$ or $\mu^+\mu^-$) are respectively the production cross section for $i \rightarrow H$ and the branching fraction for $H \rightarrow f$. The subscript SM stands for the SM prediction. Since σ_i and \mathcal{B}^f cannot be separately measured without additional assumptions, only the product of μ_i and μ^f can be extracted experimentally, μ_i^f . Figure 1.9 show the CMS results for μ_i^f and the 1σ confidence level (CL) intervals. All values are in agreement with the SM prediction within 2σ .

In order to test for deviations in the couplings of the Higgs boson to other particles, the κ -framework has been formalised. Firstly, it is assumed that there are no BSM contributions to the total Higgs boson width. With this assumption, the cross section times branching fraction for a production process

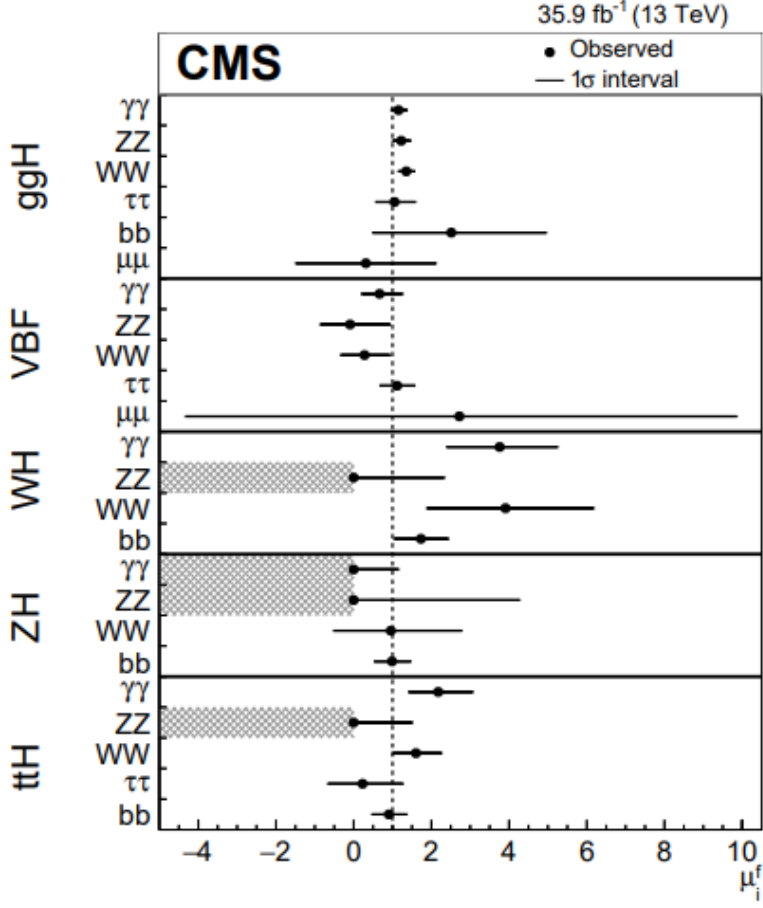


Figure 1.9: Summary plot of the fit to the production–decay signal strength products μ_i^f [15]. The points indicate the best fit values while the horizontal bars indicate the 1σ CL intervals. The hatched areas indicate signal strengths that are restricted to nonnegative values.

i and decay f can be expressed as:

$$\sigma_i \mathcal{B}^f = \frac{\sigma_i(\vec{\kappa}) \Gamma^f(\vec{\kappa})}{\Gamma_H(\vec{\kappa})} \quad (1.24)$$

where $\Gamma_H(\vec{\kappa})$ is the total width of the Higgs boson and $\Gamma^f(\vec{\kappa})$ is the partial width of the Higgs boson decay to the final state f . A set of coupling modifiers $\vec{\kappa}$ is introduced to parametrize potential deviations in the Higgs couplings from the SM predictions. For a given production process or decay mode j , a coupling modifier κ_j is defined as:

$$\kappa_j^2 = \frac{\sigma_j}{(\sigma_j)_{SM}} , \quad \kappa_j^2 = \frac{\Gamma^j}{(\Gamma^j)_{SM}} \quad (1.25)$$

In this way, the product in Eq. 1.24 can be expressed as a function of SM expectations and coupling strength modifiers:

$$\sigma_i \mathcal{B}^f = \frac{(\sigma_i)_{SM} \kappa_i^2 \cdot (\Gamma_{SM}^f) \kappa_f^2}{(\Gamma_H)_{SM} \kappa_H^2} \quad (1.26)$$

while μ_i^f becomes:

$$\mu_i^f = \frac{\kappa_i^2 \cdot \kappa_f^2}{\kappa_H^2} \quad (1.27)$$

where κ_H^2 is an expression that adjusts the SM Higgs width to take into account the modifications induced by the deformed Higgs boson couplings. When all κ_i are set to 1 the SM is reproduced. The κ -framework is the simplest parametrisation directly related to experimental measurements of the Higgs boson production and decay modes. For this reason, it has been widely used by the scientific community.

There are six free coupling parameters in this κ -framework: κ_W , κ_Z , κ_t , κ_τ , κ_b and κ_μ . A fit has been performed by CMS and ATLAS using a phenomenological parametrization relating the fermion and vector boson masses to the corresponding κ modifiers using two parameters, denoted M and ϵ . The parametrization reads:

$$\begin{aligned} \kappa_F &= v \frac{m_F^\epsilon}{M^{1+\epsilon}} \quad \text{for fermions} \\ \kappa_V &= v \frac{m_V^{2\epsilon}}{M^{1+2\epsilon}} \quad \text{for vector bosons} \end{aligned} \quad (1.28)$$

where v is the SM higgs boson vacuum expectation value. The SM is recovered when $(M, \epsilon) = (v, 0)$.

The results of the fit using the six parameter κ model are plotted versus the particle masses in Figure 1.10. In order to show both the Yukawa and vector boson couplings in the same plot, a *reduced* vector boson coupling $\sqrt{\kappa} m_V/v$ is shown. The SM expectation is reported in dashed blue line for a comparison. The fit result appears to be in agreement with the theory within the uncertainties.

Up to now the SM has proven its extraordinary predictive capability. Nonetheless, several channels are still out of reach experimentally and the Higgs couplings to light fermions as well as the self-couplings are still to be measured. For what concern the coupling to c quark, CMS has reported an observed upper limit on μ_i^f of 70 at 95% confidence level, in a direct search of Higgs boson produced in association with W or Z boson and decaying to a charm quark pair [18]. In the context of the Higgs boson self-interaction, ATLAS has performed a search for di-Higgs boson production in the $b\bar{b}\gamma\gamma$ final state, which has lead to the observed limit on the trilinear coupling modifier κ_λ of $[-1.5, 6.7]$ at 95 % CL [19].

A precise determination of the Higgs boson properties and couplings is one of the main goals at Future Colliders.

1.4 Higgs Boson Physics at Future Colliders

The upgrade of LHC, the High Luminosity LHC (HL-LHC), is scheduled to start operation from the end of 2027. The objective is to increase luminosity (and hence collision rate) by a factor of 10 beyond the LHC's design value.

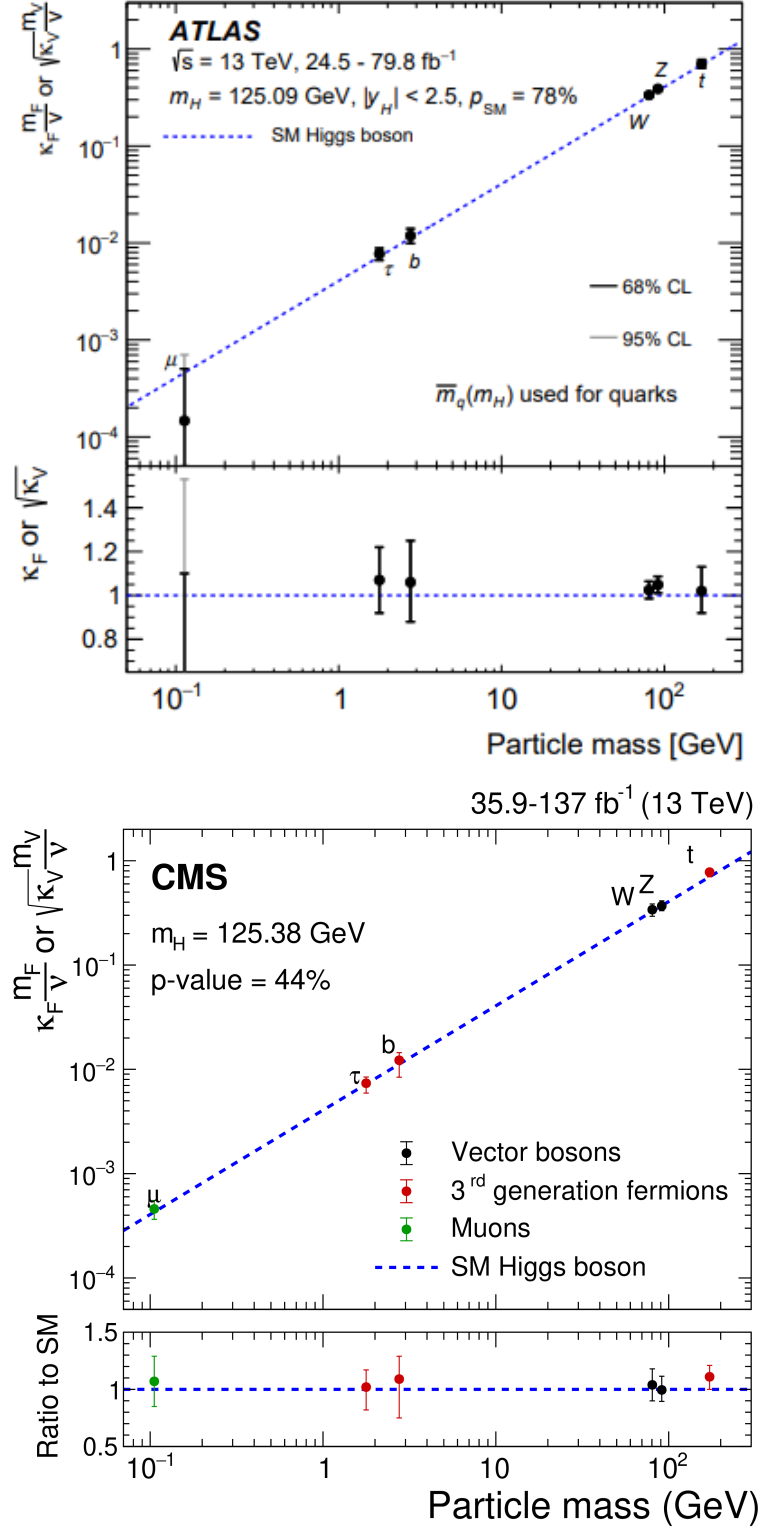


Figure 1.10: Result of the phenomenological (M, ϵ) fit overlayed with the SM expectation for ATLAS [16] and CMS [17]. The ratio of the fit result to SM prediction is shown in the bottom part of the figure. The linear trend is experimentally confirmed.

The increased luminosity will guarantee, for example, 15 million Higgs boson per year, compared to around three million from the LHC in 2017, allowing

improvement in the measurements of the Higgs-boson couplings [20].

One of the proposed options for a future collider at CERN, beyond HL-LHC, is the High Energy LHC (HE-LHC) [20], which would occupy the same tunnel but be built from advanced high-field dipole magnets that could support roughly double the LHC's energy. Such a machine would be expected to deliver an integrated proton–proton luminosity of $15,000 \text{ fb}^{-1}$ at a centre-of-mass energy of 27 TeV, increasing the discovery mass-reach beyond anything possible at the HL-LHC. The HE-LHC would provide precision access to rare Higgs boson production modes as well as an unambiguous observation of the double Higgs signal.

Other projects for future colliders have been proposed (see Table 1.2):

- The Future Circular Collider (FCC) [21] is a proposed post-LHC particle accelerator, hosted in a future 100 km tunnel at CERN, which developed and evaluated three accelerator concepts for its design report:
 - FCC-ee: a lepton collider which would operate at multiple centre of mass energies (from 91 GeV to 365 GeV);
 - FCC-hh: a proton-proton collider with the goal of reaching 100 TeV center of mass energy.
 - FCC-he: a proton-electron collider with a 50 TeV proton beam colliding with a 60 GeV electron-beam, for a center of mass energy of 3.5 TeV.
- The International Linear Collider (ILC) [22] is a proposed e^+e^- linear particle accelerator. It is planned to have a collision energy of 250 GeV, with the possibility for later upgrades up to 1 TeV. It will be between 30 km and 50 km long, more than 10 times as long as the 50 GeV Stanford Linear Accelerator, the longest existing linear particle accelerator. The facility should be hosted in Japan.
- The Compact Linear Collider (CLIC) [23] is a proposed accelerator that is being designed as an addition to CERN's accelerator complex. Its objective is to collide electrons and positrons at energies of up to several TeV, thus higher with respect to ILC experiment, although similar in length. For an optimal exploitation of its physics potential, CLIC is intended to be built and operated in three stages, at collision energies of 380 GeV, 1.5 TeV and 3 TeV respectively.
- The Circular Electron Positron Collider (CEPC) [24] is a large international scientific facility to be hosted in China in a circular underground tunnel of approximately 100 km in circumference. The CEPC would operate in three different modes: Higgs factory ($e^+e^- \rightarrow ZH$), Super Z factory($e^+e^- \rightarrow Z$) and W factory ($e^+e^- \rightarrow W^+W^-$), with center-of-mass energies of 240 GeV, 91 GeV and 160 GeV respectively.
- The Large Hadron Electron Collider (LHeC) [25] is an accelerator study for a possible upgrade of the existing LHC storage ring. In this project

a newly built electron beam of 60 GeV, up to possibly 140 GeV, collides with the intense hadron beams of the LHC.

A brief summary of the proposed Future Colliders and their characteristics is presented in Table 1.2. All the proposed Future Colliders are designed to be

Collider	Type	\sqrt{s}	\mathcal{L}_{inst} [10^{34}] $\text{cm}^{-2}\text{s}^{-1}$	\mathcal{L} [ab^{-1}]	Time [years]
HL-LHC	pp	14 TeV	5	6.0	12
HE-LHC	pp	27 TeV	16	15.0	20
FCC-hh	pp	100 TeV	30	30.0	25
FCC-ee	ee	M_Z	100/200	150	4
		$2M_W$	25	10	1-2
		240 GeV	7	5	3
		$2m_{top}$	0.8/1.4	1.5	5
					(+1)
ILC	ee	250 GeV	1.35/2.7	2.0	11.5
		350 GeV	1.6	0.2	1
		500 GeV	1.8/3.6	4.0	8.5
					(+1)
		1000 GeV	3.6/7.2	8.0	8.5
					(+1-2)
CEPC	ee	M_Z	17/32	16	2
		$2M_W$	10	2.6	1
		240 GeV	3	5.6	7
CLIC	ee	380 GeV	1.5	1.0	8
		1.5 TeV	3.7	2.5	7
		3.0 TeV	6.0	5.0	8
					(+4)
LHeC	ep	1.3 TeV	0.8	1.0	15
HE-LHeC	ep	1.8 TeV	1.5	2.0	20
FCC-eh	ep	3.5 TeV	1.5	2.0	25

Table 1.2: Summary of the Future Colliders considered in this section. The operative center of mass energy \sqrt{s} , the instantaneous \mathcal{L}_{inst} and integrated \mathcal{L} luminosity and data taking years are reported [2].

Higgs factories with the goal of a precise evaluation of the Higgs couplings to SM particles.

While the main Higgs production mechanism (illustration in Figure 1.7) at hadron colliders, as LHC, is the gluon-gluon fusion, at lepton colliders the Higgs boson is dominantly produced via Higgs-strahlung (ZH) at low energies and VBF at high ones (Figure 1.11), with WW fusion cross section roughly one order of magnitude larger than ZZ fusion one. At lepton-hadron colliders, the WW and ZZ fusion dominate.

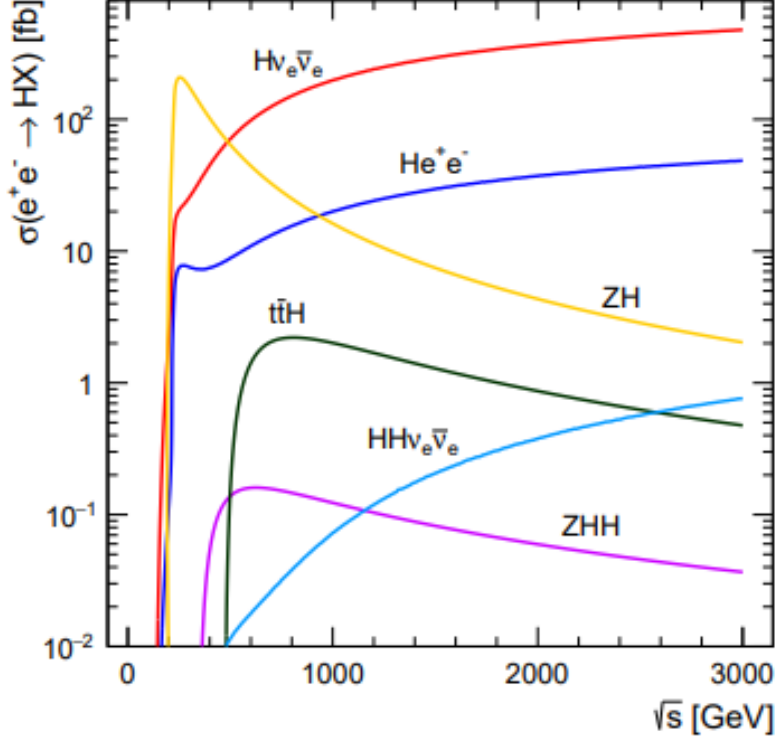


Figure 1.11: Higgs production cross sections in e^+e^- collisions. The cross section of different production processes for single and double Higgs production are shown as function of \sqrt{s} . The dominant processes for single Higgs production are Higgs-strahlung (ZH) for \sqrt{s} less than 500 GeV and VBF ($H\nu_e\bar{\nu}_e$ and He^+e^-) for greater values [1].

The extraction of the couplings of the Higgs boson relies on a simultaneous fit of all the projected measurements of $\sigma \times BR$, and their comparison to the SM values. As such, it is sensitive to both the experimental uncertainties as well as theoretical uncertainties on the production cross sections and branching ratios [2]. Table 1.3 shows the expected relative precisions at Future Colliders on the κ parameters, within the κ -framework discussed in the previous section.

In this case, the parameters are 10: κ_W , κ_Z , κ_c , κ_b , κ_t , κ_τ , κ_μ and the three effective coupling modifiers related to the loop-induced processes (e.g. $H \rightarrow \gamma\gamma$) κ_γ , κ_g and $\kappa_{Z\gamma}$. The couplings κ_s , κ_d , κ_u and κ_e that are only weakly constrained from very rare decays are not included in the combined k-framework fits presented here.

In the scenario considered here, no additional invisible or untagged branching ratio is allowed in the fits, i.e. BSM Higgs decays are not taken into account. This is the simplest possible scenario, nonetheless it clearly illustrates the potential to constrain new physics at the proposed new colliders. In general the precision is at the per cent level. In the final stage of the future colliders a precision of the order of a few per-mille would be reachable for several couplings, as κ_W and κ_Z . Cases in which a particular parameter has been fixed to the SM value due to lack of sensitivity are shown with a dash (-). Examples of this are κ_c , not accessible at HL-LHC and HE-LHC, and κ_t , only accessible above the threshold for Higgs associated production with t quarks. Not all colliders

reported results for all possible decay modes. In this case the corresponding parameters were left to float in the fits and are indicated with a \star in the tables.

κ	HL-LHC		LHeC		HE-LHC		ILC			CLIC			CEPC	FCC-ee/eh/hh
	S2	S2'			250	500	1000	380	15000	3000				
κ_W [%]	1.7		0.75	1.4	0.98	1.8	0.29	0.24	0.86	0.16	0.11	1.3		0.14
κ_Z [%]	1.5		1.2	1.3	0.9	0.29	0.23	0.22	0.5	0.26	0.23	0.14		0.12
κ_g [%]	2.3		3.6	1.9	1.2	2.3	0.97	0.66	2.5	1.3	0.9	1.5		0.49
κ_γ [%]	1.9		7.6	1.6	1.2	6.7	3.4	1.9	98 \star	5.0	2.2	3.7		0.29
$\kappa_{Z\gamma}$ [%]	10.		—	5.7	3.8	99 \star	86 \star	85 \star	120 \star	15	6.9	8.2		0.69
κ_c [%]	—		4.1	—	—	2.5	1.3	0.9	4.3	1.8	1.4	2.2		0.95
κ_t [%]	3.3		—	2.8	1.7	—	6.9	1.6	—	—	2.7	—		1.0
κ_b [%]	3.6		2.1	3.2	2.3	1.8	0.58	0.48	1.9	0.46	0.37	1.2		0.43
κ_μ [%]	4.6		—	2.5	1.7	15	9.4	6.2	320 \star	13	5.8	8.9		0.41
κ_τ [%]	1.9		3.3	1.5	1.1	1.9	0.70	0.57	3.0	1.3	0.88	1.3		0.44

Table 1.3: Expected relative precision (%) of the κ parameters in the scenario with no BSM Higgs width, for future accelerators[2]. Cases in which a particular parameter has been fixed to the SM value due to lack of sensitivity are shown with a dash (-). A star \star indicates the cases in which a parameter has been left free in the fit due to lack of input in the documentation. *FCC-ee/eh/hh* corresponds to the combined performance of FCC-ee at 240 and 365 GeV, FCC-eh and FCC-hh. In the case of HE-LHC, two theoretical uncertainty scenarios, S2 and S2', are given, with S2' theoretical uncertainty reduced by a factor two with respect to S2.

1.5 Muon Collider potential

So far, two main options have been discussed: a very energetic hadron collider and an e^+e^- collider, at either high energy (up to a few TeV) or ultra high luminosity. The former has a much higher discovery reach of new states, while the latter allows a precision-measurement campaign of the Higgs/EW sector providing a much cleaner environment. Furthermore e^+e^- colliders have the advantage of reaching higher energy final states than an equivalent hadron machine, since leptons undergo simple single-particle interactions. On the other hand extension of these colliders to multi-TeV energies is severely performance constrained by beamstrahlung, and cost-constrained because two full energy linear accelerators (*linacs*) are required to avoid the excessive synchrotron radiation that would occur in rings.

Accelerating muons would allow to gain the same advantages of electrons and at the same time have negligible beamstrahlung, since muons are more massive than electrons ($m_\mu/m_e = 207$) and the energy loss goes as the inverse of the fourth power of the mass. For this reason, muons could be accelerated and stored in rings, realizing higher energy collisions (tens of TeV) [26]. For example, if the LHC ring were used, with the proposed HE-LHC dipoles (Nb3Sn, 16 T), muons would collide at an energy close to $\sqrt{s} = 14$ TeV, compared to the 0.2 to 0.4 TeV of an electron-positron collider [2].

The possible center of mass energy under discussion ranges from 1.5 TeV to 30 TeV, with a representative benchmark target at 10 TeV. Very high luminosity is also envisioned. Working hypothesis are given in Table 1.4.

Collider	Type	\sqrt{s}	\mathcal{L}_{inst} [$10^{34} \text{ cm}^{-2} \text{s}^{-1}$]	\mathcal{L} [ab^{-1}]	Time s
Muon Collider	$\mu\mu$	1.5	1.25	0.5	$4 \cdot 10^7$
		3.0	4.4	1.3	$4 \cdot 10^7$
		10	20	8.0	$4 \cdot 10^7$

Table 1.4: Working hypothesis for the Muon Collider [27].

Since collision energies of tens of TeV are currently achievable only with proton-proton machines, it is useful to compare the muon collider with the hadronic option. As already quoted in the electron-positron case, the obvious advantage in colliding muons rather than protons is that the muon collider center of mass energy, $\sqrt{s_\mu}$ is entirely available to produce short-distance reactions. At a proton collider, instead, the relevant interactions occur between the proton constituents, which carry a small fraction of the collider energy, $\sqrt{s_p}$. The consequence is that equal muon and proton collider cross-sections are obtained for $\sqrt{s_\mu} \ll \sqrt{s_p}$, as illustrated in Figure 1.12. The plot shows the energy at which the proton collider cross-section equals that of a muon collider, an estimate that generically applies to any $2 \rightarrow 2$ reaction with a high energy threshold.

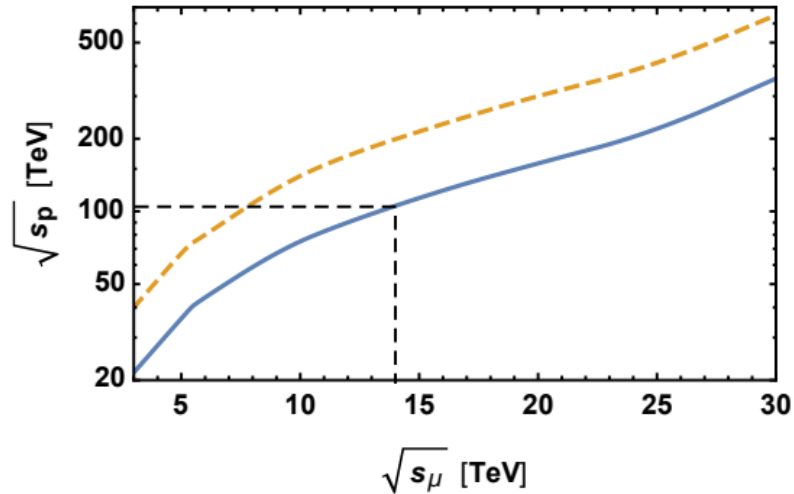


Figure 1.12: The energy at which the proton collider cross-section equals that of a muon collider. The dashed line assumes comparable Feynman amplitudes for the muon and the proton production processes. A factor of ten enhancement of the proton production amplitude squared, possibly due to QCD production, is considered in the continuous line [28].

Figure 1.12 suggests that a 14 TeV muon collider with sufficient luminosity might be very effective as a direct exploration machine, with a physics motivation and potential similar to that of a 100 TeV proton-proton collider (as

FCC-hh) [28]. For this dream-like machine, sensitivity to new resonances beyond present experiment goes with high accuracy in EW and Higgs coupling measurements. For instance [29] with an integrated luminosity of 10 ab^{-1} , a 10 TeV muon collider would produce about 10^7 Higgs bosons and 3.6×10^4 Higgs pairs (diagrams in Figure 1.13), some of them generated through the pair production mechanism ((a) diagram) that is sensitive to the trilinear Higgs coupling.

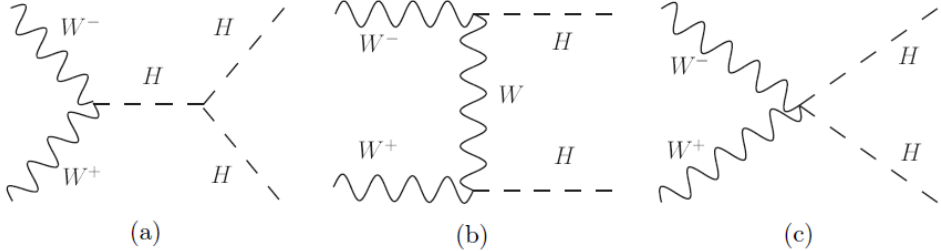


Figure 1.13: Double Higgs production at a high energy muon collider via W^+W^- fusion. The production goes through the VBF topology.

The high rate of Higgs boson production is due to the large cross-section of VBF at a muon collider. In the high energy limit, indeed, VBF cross section is larger than the analogous s-channel annihilation rate, as clear from Figure 1.14 where the single, double and triple Higgs production are considered.

One would expect that another advantage of a muon collider relative to hadronic machines is the lower background level. However, it is unclear to what extent this is the case because of the large beam background originated by muons weakly decaying into electrons and neutrinos (see discussion in Section 2.3).

A massive program of Higgs coupling accuracy determination is needed to fully assess the Muon Collider potential and physics reach.

The only study about precision achievable at the Muon Collider on Higgs coupling was performed very recently in Ref. [31].

The results obtained on the relative precision on Higgs boson coupling to b quark are reported in Table 1.5, compared with the CLIC estimation [32].

The muon collider results are not complete, since not all the necessary parameters are determined. Data samples at the three center-of-mass energies are treated as independent, and not taken successively into account, while each CLIC new stage includes all measurements of the previous ones.

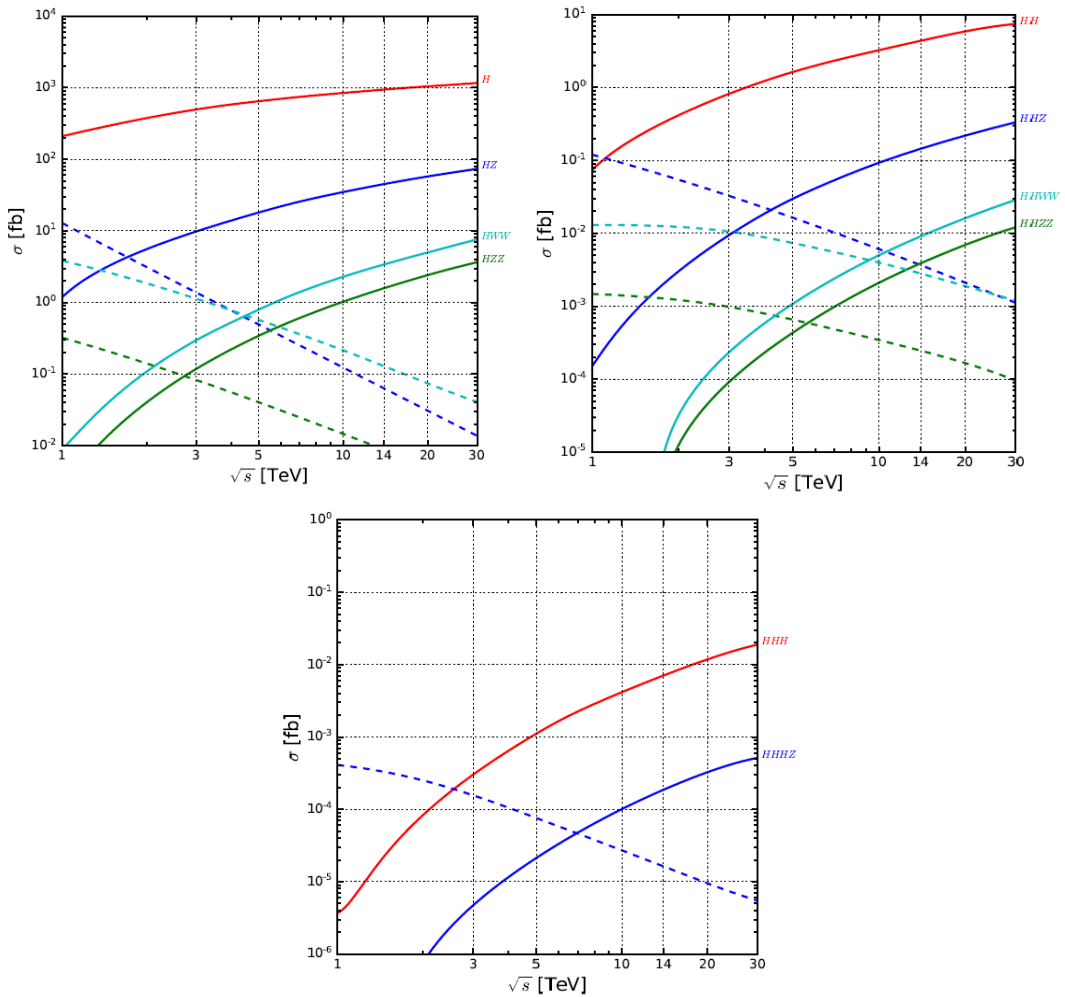


Figure 1.14: W^+W^- fusion (solid) and analogous s-channel annihilation (dashed) cross sections for HX (left), HHX (middle) and $HHHX$ (right) [30].

	\sqrt{s} [TeV]	\mathcal{L}_{int} [ab^{-1}]	$\frac{\Delta g_{Hbb}}{g_{Hbb}}$ [%]
Muon Collider	1.5	0.5	1.9
	3.0	1.3	1.0
	10	8.0	0.91
CLIC	0.35	0.5	3.0
	1.4	+1.5	1.0
	3.0	+2.0	0.9

Table 1.5: Relative precision on Higgs boson coupling to b quark at Muon Collider [31] and at CLIC [32].

Chapter 2

Muon Collider machine and detector

The idea of a muon collider has been discussed since '80s and its design was developed over the years, up to the creation of the Muon Accelerator Program (MAP) in the US [33], whose activities were suspended in 2015. Recently, the scientific community has seen a renewed interest in muon collider, which takes a place in the European Strategy for Particle Physics 2020 [1] as a promising unconventional machine, although not mature enough to be considered for construction today.

A muon collider has the potential to provide excellent performance (see Section 1.5) at reasonable power consumption. A figure of merit for energy-frontier facilities can be defined as the luminosity per unit power. This figure of merit appears to be substantially larger for the muon collider than for any other lepton collider technology in the multi-TeV range [34].

However, a muon collider accelerator presents several technical challenges [28]:

- Muons decay with a lifetime of $\tau = 2.2 \mu s$. This problem is partially overcome by rapidly increasing the energy of the muons, and thus benefiting from their relativistic γ factor. Indeed, their lifetime is the laboratory frame is $\tau_{lab} = \gamma \cdot \tau$, where $\gamma = E/m_\mu$.
- Electrons from muon decay, $\mu \rightarrow e\nu\bar{\nu}$, travel to the inside of the ring magnets, and radiate energetic synchrotron photons tangent to the electron trajectory. Electromagnetic showers induced by these electrons and photons in the collider components generate intense fluxes of muons, hadrons and daughter electrons and photons, which create high background and radiation levels both in the detector and in the storage ring. Considering the design chosen by MAP for the facility (see Table 2.1), there would be 1.28×10^{10} muon decays per meter per second for two 0.75 TeV muon beams. This would result in ~ 250 GeV electrons producing an overall background at the rate of 0.5-1 kW/m, to be compared with the acceptable limit of few W/m [35].

Machine and detector design must take into account this Beam Induced Background (BIB), otherwise this would affect the performance, damaging the detector components, worsening the object reconstruction and deteriorating the detector resolution.

- If muons are produced through pion decay (see Section 2.1), they are created into a diffuse phase space, thus in order to obtain high collimated beams some form of cooling is essential.

In the following, the two schemes proposed for the muon production and acceleration are outlined. Afterwards, the detector description is presented and, finally, the BIB issue is addressed together with the main mitigation strategies under analysis.

2.1 Muon Accelerator Complex

The basic layouts of the two schemes proposed for muon beam production are shown in Figure 2.1.

The top one is the *proton driver scheme* developed by MAP and based on the production of pions which subsequently decay into muons.

The bottom one is the novel approach of the *Low Emittance Muon Accelerator* (LEMMA) [36] recently proposed and now under study for application at the Muon Collider [37], which is based on muon pair production with a positron beam impinging on electrons at rest in a target.

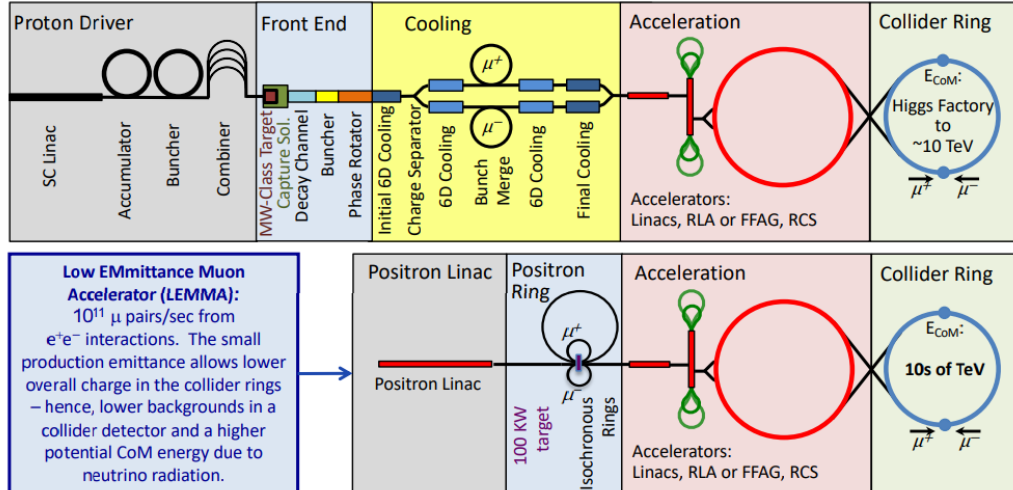


Figure 2.1: Schematic layouts of Muon Collider complexes based on the proton driver scheme (top) and on the low emittance positron driver scheme (bottom).

In the MAP scheme, muons are produced as tertiary particles from decay of pions created by a high-power proton beam impinging on a high-Z material target. The majority of the produced pions have momenta of a few hundred MeV/c, with a large momentum spread and transverse momentum component comparable to longitudinal one. Hence daughter muons are produced with low energy and large spread in phase space. They need to be cooled down rapidly before decay. The facility in the *proton driver scheme* is specifically designed to address this issue. It is divided in five different sections [28]:

- *Proton driver*

It produces a high-power multi-GeV bunched ($\simeq 2$ ns) proton beam.

The fundamental requirement is the number of useful muons produced at the end of the decay channel, which is approximately proportional to the primary proton beam power. Considering a conversion efficiency of about 0.013 muons per proton-GeV a proton beam in the 1-4 MW power range at an energy of 6.75 GeV provides the number of muons of each kind required for the Muon Collider.

- *Front End*

It contains a pion production target, capable of withstanding the high proton beam power, inserted in a high field solenoid to capture the pions and guide them into a decay channel. The decay channel, equipped with radiofrequency (RF) cavities, captures the muons into a bunch train and then applies a time-dependent acceleration that increases the energy of the slower bunches and decreases the energy of the faster bunches.

- *Cooling*

An initial cooling channel uses a moderate amount of ionization cooling to reduce the 6D phase space occupied by the beam by a factor of 50 (5 in each transverse plane and 2 in the longitudinal plane), so that it fits within the acceptance of the first acceleration stage.

Ionization cooling [38] (see Figure 2.2) simply consist of passing a focused beam through an energy absorber, where the muon initial momentum (p_{in}) is reduced (of Δp_{abs}) in all the directions, and subsequently through RF cavities, where only the longitudinal component is regenerated (of Δp_{RF}). The longitudinal emittance is later reduced through emittance exchange: a bending magnet separates different momentum particles, which, then, pass through an absorber properly designing to have greater energy loss at higher momenta. In this process longitudinal emittance is reduced at the expense of increasing transverse emittance.

Afterwards muons of opposite charge are separated. For high luminosity collider applications, further ionization cooling stages interest muons of both sign, in order to reduce the 6D phase space occupied by the beam by up to five orders of magnitude.

- *Acceleration*

The beam is accelerated with a series of fast acceleration stages, which may include Recirculating Linear Accelerators (RLA) [39], Fixed Field Alternating Gradient (FFAG) machines [40], and/or Rapid Cycling Synchrotrons (RCS) [41]. The accelerator chain takes the muon beams to the desired energy before injection in the Muon Collider ring.

- *Collider Ring*

In this stage, muon beams finally collide at a center of mass energy up to few tens of TeV (at the beginning the hypothesis of a Higgs factory working at 125 GeV was also taken into account by MAP, although later discarded).

Table 2.1 reports the main parameters of the Muon collider facility at the different working hypothesis studied by MAP [34].

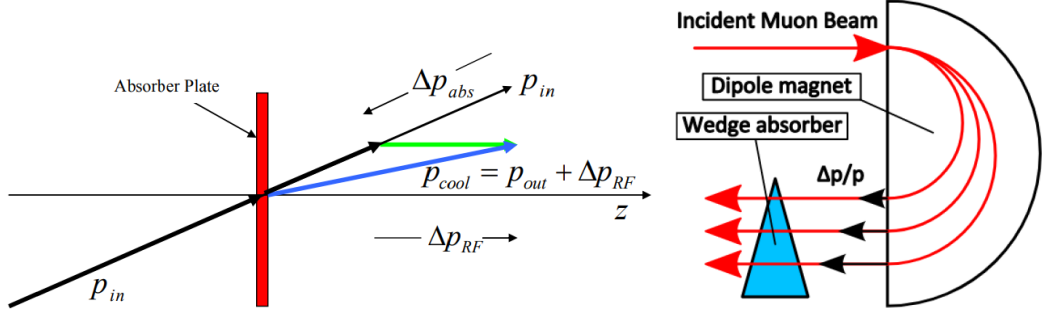


Figure 2.2: Conceptual picture of the principle of ionization cooling. A particle loses momentum by ionizing an energy absorber, where only the longitudinal momentum is restored by RF cavities (left). Longitudinal cooling is achieved through the process of emittance exchange (right).

Parameter	Units	Higgs	Multi-TeV		
CoM Energy	TeV	0.126	1.5	3.0	6.0
Avg. Luminosity	$10^{34} \text{cm}^{-2}\text{s}^{-1}$	0.008	1.25	4.4	12
Beam Energy Spread	%	0.004	0.1	0.1	0.1
Higgs Production/ 10^7 sec		13'500	37'500	200'000	820'000
Circumference	km	0.3	2.5	4.5	6
No. of IP's		1	2	2	2
Repetition Rate	Hz	15	15	12	6
$\beta_{x,y}^*$	cm	1.7	1	0.5	0.25
No. muons/bunch	10^{12}	4	2	2	2
Norm. Trans. Emittance, ε_{TN}	$\mu\text{m-rad}$	200	25	25	25
Norm. Long. Emittance, ε_{LN}	$\mu\text{m-rad}$	1.5	70	70	70
Proton Driver Power	MW	4	4	4	1.6
Wall Plug Power	MW	200	216	230	270

Table 2.1: Main parameters of the MAP proton driver muon facility working at different center of mass energies.

The proton driver muon source generates beams with relatively large emittance. This is due to the multiple scattering, that occurs in the absorber, which limits the capacity to cool the initial large emittance muon beams by ionization. Therefore relatively larger muon beam currents in the collider are necessary to reach high luminosities. When the muons decay while circulating in the collider ring, they generate a large background in the detector and also lead to significant radiation at the surface (neutrino induced hazard is a well known problem in this context [42]). This ultimately limits the energy and luminosity that can be reached at the Muon Collider.

The LEMMA concept proposes to overcome this limitation by generating very small emittance muon beams, without any need for muon cooling. This would allow high luminosities with much smaller beam currents and consequently reduced detector background and surface radiation.

In this scheme, muon production occurs by the interaction of a 45 GeV positron beam with electrons in a target right above the threshold for the muon pair creation. In this way, muon beams with low enough transverse emittance are generated.

The main limitation of this idea is the low muon conversion efficiency, for

instance $9 \cdot 10^{-8}$ muons per positron are produced using a 3 mm Beryllium target. A solution could be that of a positron storage ring (see bottom picture in Figure 2.1) with an internal target, in order to allow multiple interactions of the positrons with the electrons at rest in the target. Nonetheless the required intensity of the positron beam is very high and this would induce a high stress on the target system.

Presently the feasibility of this scheme is still under study, as it is less mature than the MAP project.

2.2 Detector description

Before starting the detailed description on the Muon Collider detector, a review of the coordinate convention is useful.

The Muon Collider coordinate system is right-handed and its origin is at the center of the detector, which is the nominal interaction point (IP). The z -axis has the direction of the beam pipe, the x -axis points radially inward to the center of the ring and the y -axis points vertically upward.

Since the experiment has a cylindrical symmetry, it is useful to define cylindrical coordinates to label the position of particles. In particular, a radial coordinate r and two angles are used. The r coordinate is measured in the x - y plane, the azimuthal angle ϕ is defined as the angle measured from the x -axis in the same plane, while the polar angle θ is measured from the z -axis.

Usually, θ is substituted by the pseudorapidity η , defined as:

$$\eta = -\ln \left(\tan \frac{\theta}{2} \right) \quad (2.1)$$

The Muon Collider detector is divided in three regions based on pseudorapidity:

- The *barrel* that corresponds to the region with $|\eta| < 1.1$.
- Two *endcaps* (one forward, one backward), characterized by $1.1 < |\eta| < 2.4$.

The original design of the detector has been provided by the CLIC collaboration [43] and few components were changed, according to the MAP studies [35] [44]. Moreover, the Interaction Region (IR) and the Machine-Detector Interface (MDI) (Figure 2.3) was carefully designed to reduce the deleterious effects of the background and radiation environment produced by muon decays. For this purpose, two additions are implemented:

- High-field superconducting (SC) dipoles, interlaced with the quadrupoles, are added with the aim of sweep decay electrons away from the detector. A tungsten shield (coloured in yellow in Figure 2.3) is designed to protect magnets in the final focus region.
- Sophisticated tungsten cones (*nozzles*) are inserted inside the detector (always in yellow in Figure 2.3) in order to shield the detector components.

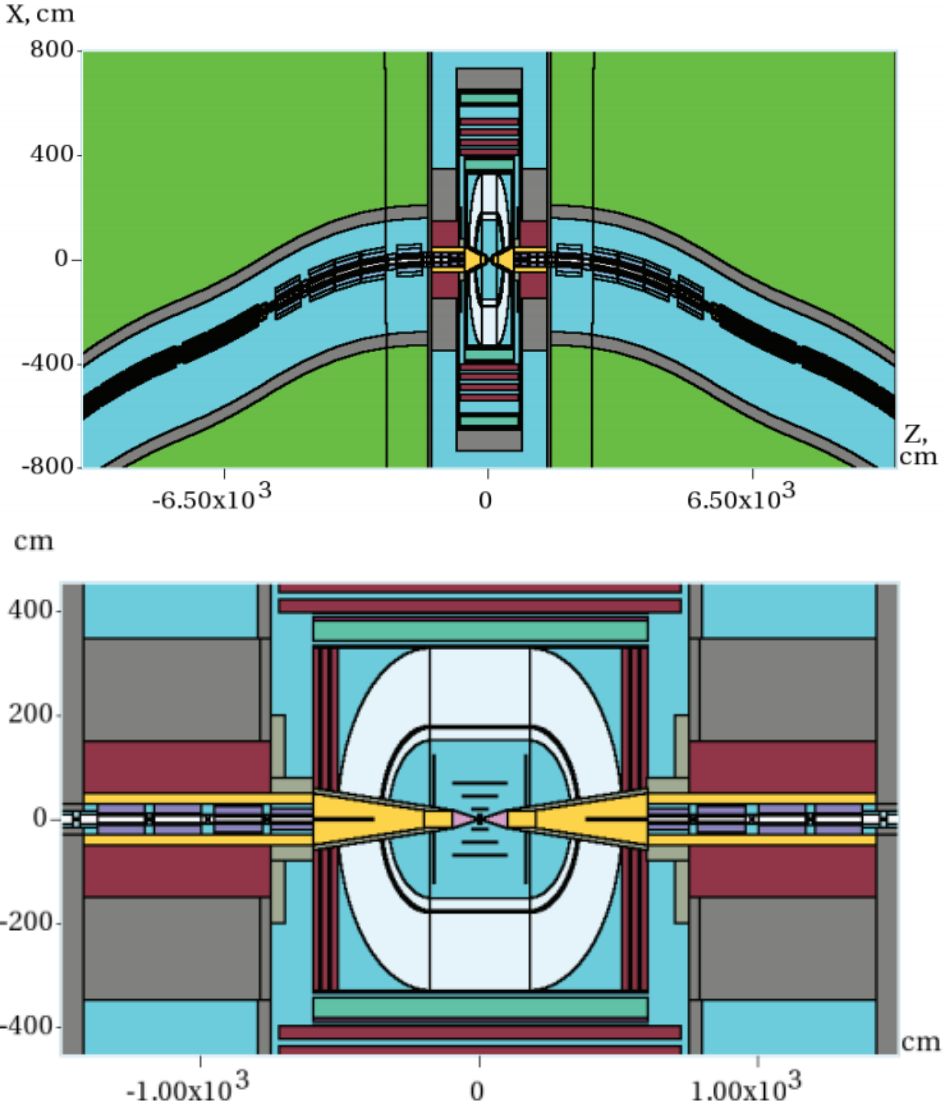


Figure 2.3: Plan views of MARS (simulation code [45]) for the Interaction Region (top) and the detector with the MDI (bottom). The tungsten components are coloured in yellow, empty spaces in light blue, iron components in red and concrete supports in grey.

According to MAP studies, the dipoles close to the IP and tungsten masks in each interconnect region help reduce background particle fluxes in the detector by a substantial factor.

Moreover, the tungsten nozzles, assisted by the detector solenoid field, trap most of the decay electrons created close to IP as well as most of the incoherent pairs e^+e^- generated in the IP. The opening angle of the nozzles in the region closest to the IP (z from 6 to 100 cm) is the most critical parameter to optimize, since the larger the angle the better background suppression but the poorer is the detector performance in the forward region. For instance, the total number of photons and electrons entering the detector per bunch crossing is 1.5×10^{11} and 1.4×10^9 respectively for a 0.6 degrees nozzle, while it is reduced by a three order of magnitude for an opening angle of 10 degrees. Currently, this 10-degree configuration is adopted, while in the z -region be-

tween 100 and 600 cm the angle is reduced to 6 degrees. In this more distant region the tungsten is also encapsulated in a borated polyethylene cladding to reduce the flux of low-energy neutrons.

Figure 2.4 shows a sketch of the detector together with the indication of each sub-detector system and relative characteristics. From the inside to the outside, the detector is composed of:

- A tracking system consisting of a vertex detector (close to the beam pipe) and inner and outer trackers.
- An electromagnetic calorimeter (ECAL).
- An hadronic calorimeter (HCAL).
- A superconducting solenoid which provides a magnetic field of 3.57 T.
- An iron yoke instrumented with detectors for muon identification.

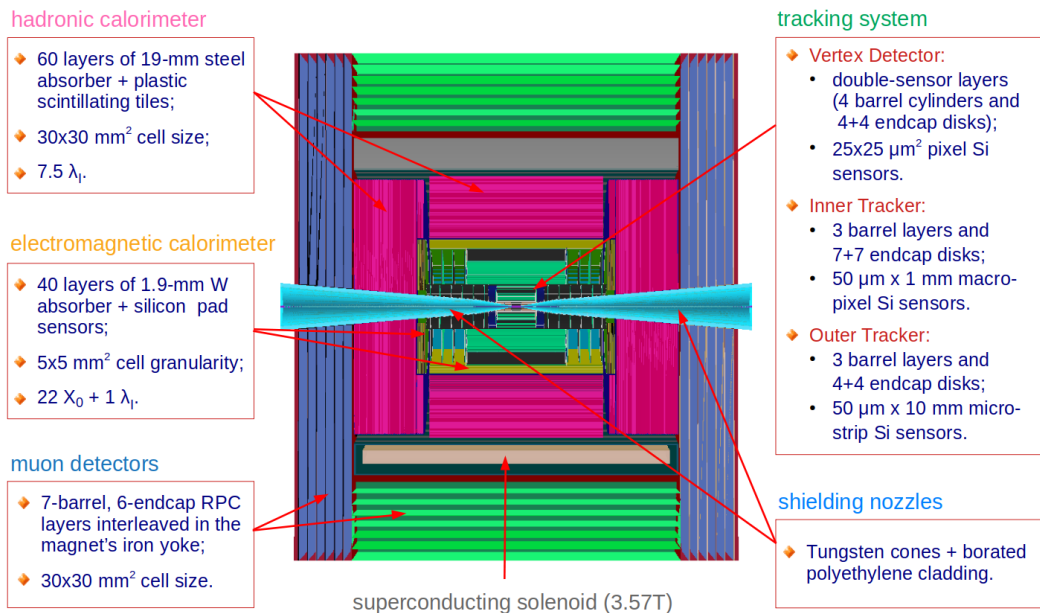


Figure 2.4: Longitudinal section of the detector at the Muon Collider. Each sub-detector system is indicated and briefly described in terms of its components.

2.2.1 Tracking system

The transverse momenta of charged particles are measured by the tracker system (Figure 2.5), which is composed of a vertex detector (Figure 2.6), the closest to the beam pipe, a inner tracker and an outer tracker detector.

The vertex detector (VTX) needs to be close to the IP in order to identify secondary vertices, that are signature of b and c hadron decay.

In the barrel, VTX is made up of four cylindrical shells placed at different

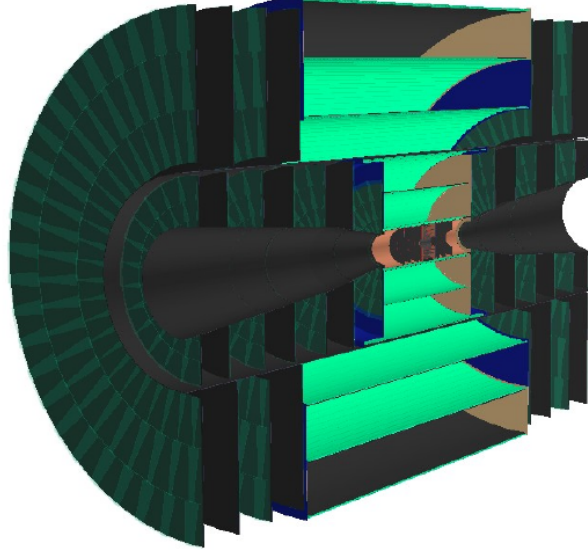


Figure 2.5: Longitudinal section of the full tracker system.

radii. Each shell consists of rectangular double-layer modules (or *staves*), i.e. two sensitive layers fixed on one support structure with 2 mm gap. In each endcap, instead, there are four disks at different z which consist of sixteen trapezoidal modules of double-layer sensors arranged as "petal". Pixels in the vertex detector are made of silicon with a $25 \times 25 \mu\text{m}^2$ area and a $50 \mu\text{m}$ thickness. The time resolution is 30 ps and the spatial one is $5 \mu\text{m} \times 5 \mu\text{m}$. Table 2.2 summarizes the layer geometrical characteristics for barrel and endcap regions of the vertex detector.

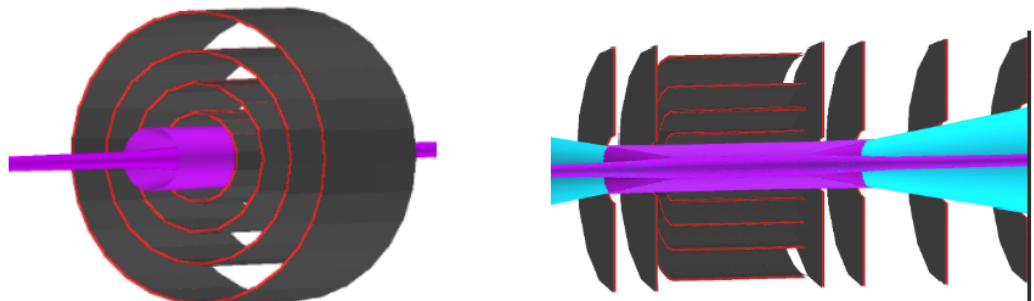


Figure 2.6: The VTX barrel detector (left), and longitudinal view of the entire VTX (right) where endcap detectors are visible as half disks.

Right after the vertex detector, the inner tracker (IT) follows. It is composed of three cylindrical shells in the barrel and seven disks in both endcaps (each disk is composed of 26 modules). The double-layer structure is not employed. Each macropixel is made of silicon with a thickness of $100 \mu\text{m}$ and an area of $50 \mu\text{m} \times 1 \text{ mm}$. The time resolution is 60 ps and the spatial one is $7 \mu\text{m} \times 90 \mu\text{m}$. Table 2.3 summarizes the layer geometrical characteristics for barrel and endcap regions of the inner tracker.

Barrel Layer	R (cm)	$ z_{max} $ (cm)	N. of staves
1	3.0	6.5	16
2	5.1	6.5	15
3	7.4	6.5	21
4	10.2	6.5	29

Endcap Layer	$ z $ (cm)	R_{min} (cm)	R_{max} (cm)
1	8.0	2.5	11.2
2	12.0	3.1	11.2
3	20.0	3.8	11.2
4	28.0	5.3	11.2

Table 2.2: VTX barrel (top) and VTX endcap (bottom) layer geometrical characteristics [46].

Barrel Layer	R (cm)	$ z_{max} $ (cm)	N. of staves
1	12.7	48.2	28
2	34.0	48.2	76
3	55.4	69.2	124

Endcap Layer	$ z $ (cm)	R_{min} (cm)	R_{max} (cm)
1	52.4	9.5	40.5
2	80.8	14.7	55.5
3	109.3	19.0	55.5
4	137.7	21.2	55.5
5	166.1	23.7	55.5
6	194.6	26.4	55.5
7	219.0	28.4	55.5

Table 2.3: IT barrel (top) and IT endcap (bottom) layer geometrical characteristics [46].

The latest sub-detector in the tracker system is the outer tracker (OT). It is composed of three cylindrical shells in the barrel and four disks in both end-caps (each disk is composed of 48 modules). The double-layer structure is not employed. Each microstrip is made of silicon with a thickness of $100 \mu m$ and an area of $50 \mu m \times 10 mm$. The time resolution is 60 ps and the spatial one is $7 \mu m \times 90 \mu m$. Table 2.4 summarizes the layer geometrical characteristics for barrel and endcap regions of the outer tracker.

Cell size and thickness together with the time and spatial resolution for each stage of the tracker system are summarized in Table 2.5.

2.2.2 Calorimetry

Calorimetry has the aim of measuring a particle energy by exploiting the electromagnetic or hadronic shower initiated in matter by the particle.

Barrel Layer	R (cm)	$ z_{max} $ (cm)	N. of staves
1	81.9	124.9	184
2	115.3	124.9	256
3	148.6	124.9	328

Endcap Layer	$ z $ (cm)	R_{min} (cm)	R_{max} (cm)
1	131.0	61.75	143.0
2	161.7	61.75	143.0
3	188.3	61.75	143.0
4	219.0	61.75	143.0

Table 2.4: OT barrel (top) and OT endcap (bottom) layer geometrical characteristics [46].

Detector	Cell size	Sensor thickness	Time resolution	Spatial resolution
Vertex	$25 \mu m \times 25 \mu m$ pixels	$50 \mu m$	30 ps	$5 \mu m \times 5 \mu m$
Inner Tracker	$50 \mu m \times 1 mm$ macropixels	$100 \mu m$	60 ps	$7 \mu m \times 90 \mu m$
Outer Tracker	$50 \mu m \times 10 mm$ microstrips	$100 \mu m$	60 ps	$7 \mu m \times 90 \mu m$

Table 2.5: Cell dimensions and resolutions for the three sub-detectors making up the tracker system.

An electromagnetic calorimeter is specifically designed to measure the energy of particles that interact primarily via the electromagnetic interaction, i.e. particles that develop electromagnetic showers, while a hadronic calorimeter is designed to measure particles that interact via the strong nuclear force, i.e. particles that develop hadronic showers.

Usually the material in which the particle shower takes place is distinct from the material that measures the deposited energy. This is the case of the *sampling calorimeter*. Typically the sensitive material and the absorber alternate.

Electromagnetic and hadronic calorimeters at the Muon Collider follows the CLIC design. Figure 2.7 shows the ECAL in yellow and the HCAL in magenta.

The ECAL and HCAL barrel are arranged in dodecagons around the tracker volume. The endcap calorimeters are arranged to provide good coverage in the transition region, and maximum coverage to small polar angles up to the nozzle location.

The ECAL is a highly granular array of 40 layers of silicon sensors and tungsten plates. The 1.9 mm tungsten plates, together with sensors and readout, add up to 22 radiation lengths. The lateral segmentation of the $300 \mu m$ thick sensors is chosen to be $5 \times 5 mm^2$.

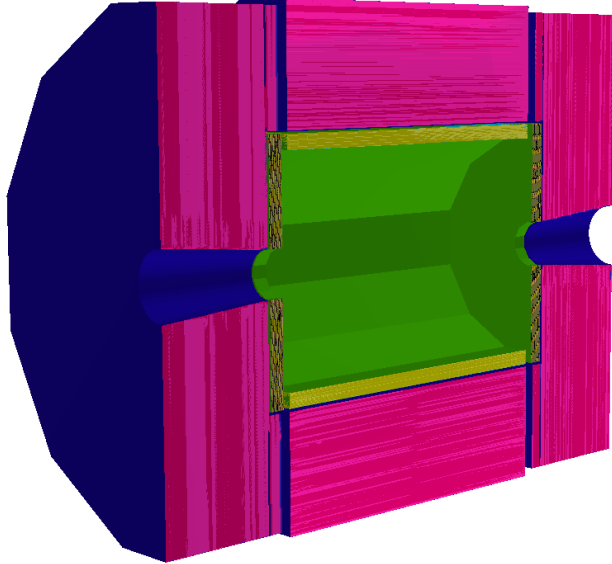


Figure 2.7: Longitudinal section of the calorimeter system.

The HCAL is built from 60 layers of plastic scintillator tiles, read out by silicon photomultipliers, interleaved with 20 mm thick steel absorber plates. The scintillator tiles are 3 mm thick and have lateral dimensions of $3 \times 3 \text{ cm}^2$. In terms of nuclear interaction lengths the endcap and the barrel HCAL are long 7.5, which adds up to the one interaction length from the ECAL. Table 2.6 and 2.7 report the ECAL and HCAL dimensions in the barrel and endcap region, respectively. The materials used for absorption and detection are also specified.

Barrel Detector	R_{min} (cm)	R_{max} (cm)	$ z_{max} $ (cm)	Radiator	Sensor
ECAL	150.0	170.2	221.0	Tungsten	Silicon
HCAL	174.0	333.0	221.0	Steel	Polystyrene

Table 2.6: ECAL and HCAL dimensions in the barrel region. Absorber and sensor materials employed are also reported [46].

Endcap Detector	R_{min} (cm)	R_{max} (cm)	$ z_{min} $ (cm)	$ z_{max} $ (cm)	Radiator	Sensor
ECAL	26.0	170.0	230.7	250.9	Tungsten	Silicon
HCAL	30.7	324.6	253.9	412.9	Steel	Polystyrene
HCAL Ring	173.8	324.6	235.4	253.9	Steel	Polystyrene

Table 2.7: ECAL and HCAL dimensions in the endcap region. The HCAL ring connects the endcap to the barrel section, providing a good coverage in the transition region. Absorber and sensor materials employed are also reported [46].

2.2.3 Muon detector system

A large superconducting solenoid of 382 cm radius is located outside the calorimeters, producing a nominal 3.57 T magnetic field inside it.

The muon system is placed outside the magnet, and the detector stations are integrated into the iron return yokes so that the 3.57 T magnetic field inside the solenoid and the 1.34 T average return field bend the muon tracks in the transverse plane.

The muon system consists of Resistive Plate Chambers (RPC). There are seven RPC layers in the barrel and six layers in the endcaps, with $30 \times 30 \text{ mm}^2$ cell size. The free space between yoke steel layers is 40 mm.

Figure 2.8 displays a longitudinal section of the outer part of the Muon Collider detector, showing the solenoid and the muon chambers.

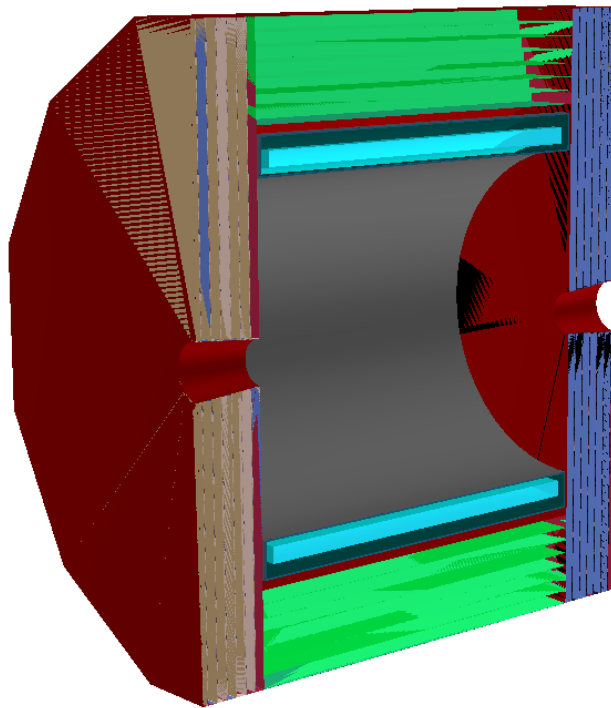


Figure 2.8: Longitudinal section of the solenoid (cyan) and muon detectors (in blue and green).

2.3 Data taking conditions: the Beam Induced Background issue

The composition and the characteristics of the BIB in a muon collider have been studied in detail in Ref. [35] for $\mu^+\mu^-$ collision at 1.5 TeV. The main source of the BIB (Figure 2.9) are the electrons and positrons, generated in muon decays, and the synchrotron photons, successively radiated by the primary e^\pm , which interact with the machine components and the surrounding environment producing secondary particles (charged and neutral hadrons, Bethe-Heitler muons, electrons and photons) that eventually may reach the detector.

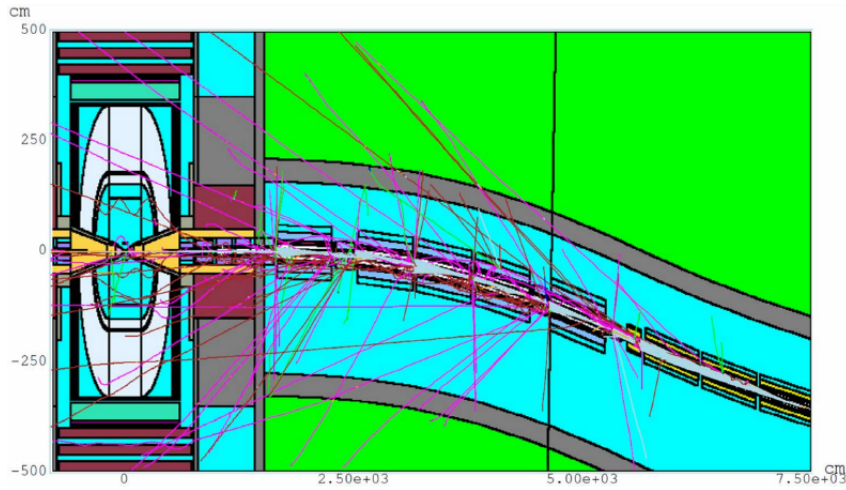


Figure 2.9: MARS [45] model of the IR and detector. Several BIB tracks are also shown [47].

Figure 2.10 shows the distributions of the different species of background particles as a function of the decay point of the parent muon. The BIB primarily consist of particle produced by muons decaying in a range of ± 25 m around the IP. Outside that range the detector background contributions become negligible.

Table 2.8 reports the expected average number of muon decays per meter and the estimated yields of background particles entering the detector per bunch crossing when a bunch intensity of 2×10^{12} muons is assumed. The suppression factor of the BIB due to the shielding nozzles and the protective masks in between the IR SC magnets (see Section 2.2) is estimated to be of the order of $\sim 1/500$. Nevertheless, the absolute flux of particles is still high and poses a serious challenge for the detector readout and particle reconstruction.

The momentum spectra of the BIB is reported in Figure 2.11.

Photons and electrons are characterized by a soft momentum spectra with $\langle p_\gamma \rangle = 1.7 \text{ MeV}$ and $\langle p_e \rangle = 6.4 \text{ MeV}$. Hadrons are on average more energetic with a momentum of about half a GeV. Muons have much higher momenta with $\langle p_\mu \rangle = 14 \text{ GeV}$.

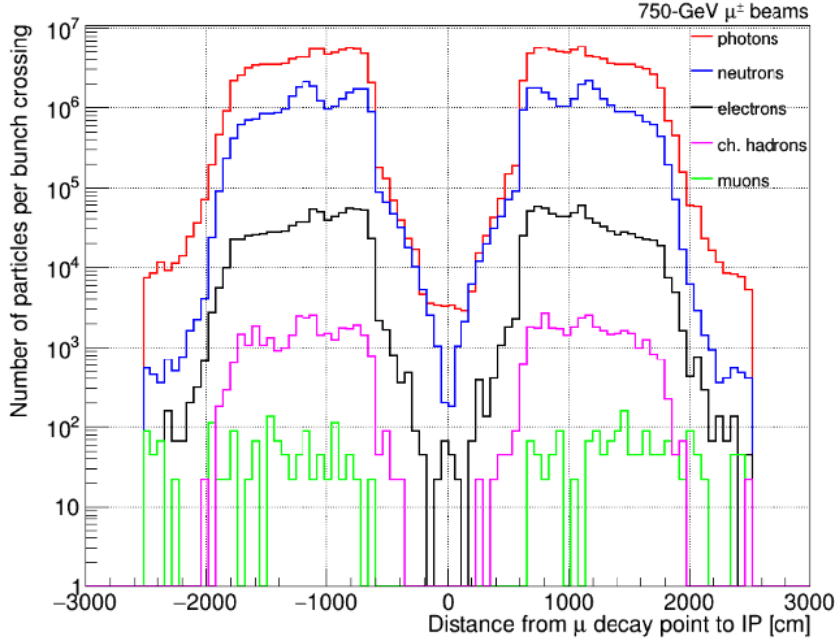


Figure 2.10: Particle composition of the beam-induced background as a function of the muon decay distance from the interaction point [48].

μ decay/m per beam	photons (0.2MeV)	neutrons (0.1MeV)	electrons (0.2MeV)	ch. hadrons (1MeV)	muons (1MeV)
4.3×10^5	1.6×10^8	4.8×10^7	1.5×10^6	6.2×10^4	2.7×10^3

Table 2.8: Expected average number of muon decays per meter and estimated number of background particles entering the detector per bunch crossing. In parentheses the thresholds set on the particle kinetic energy in simulation (MARS code used [45]) are shown [48].

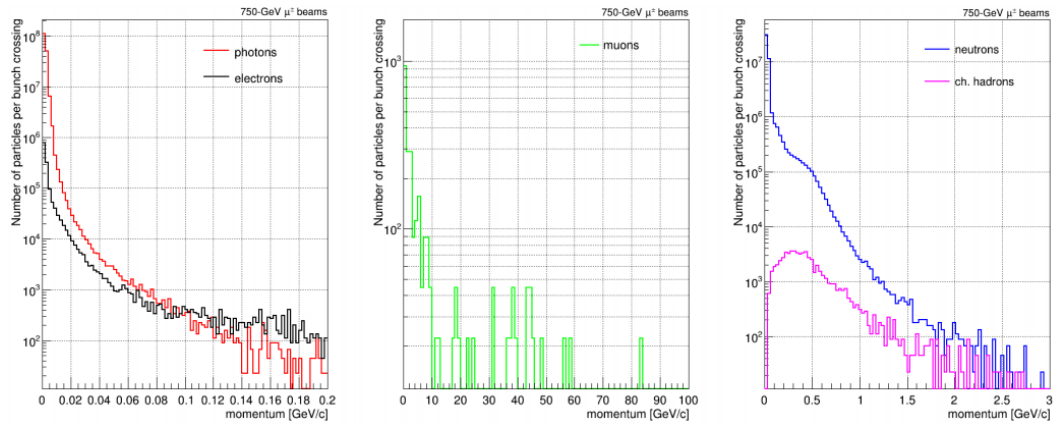


Figure 2.11: Momentum spectra of the beam-induced background particles at the detector entry point [48].

An important feature of the BIB particles is represented by their timing. The time of arrival at the detector entry point of background particles has a significant spread with respect to the bunch crossing time, as can be seen in Figure 2.12. The peaks around zero are due to leakages of mainly photons and electrons nearby the IP, where the shielding is minimal.

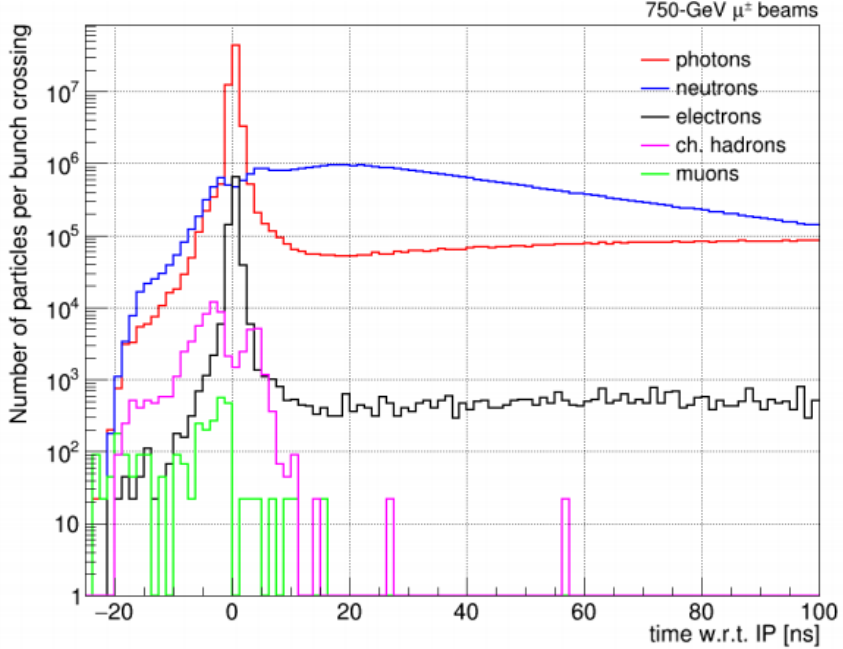


Figure 2.12: Time of arrival of the background particles at the detector entry point with respect to the bunch crossing time [48].

Figure 2.13 shows the simulated arrival time of BIB particles and prompt muons (i.e. from IP) to the tracker modules, with respect to the expected arrival time of a photon radiated from the interaction point.

The asynchrony of the BIB particles, visible in Figure 2.13, is at the base of the mitigation strategy implemented at the Muon Collider. The timing cut is highly effective in reducing hit occupancy, which is a serious problem in the tracker system, especially in the vertex detector.

Figure 2.14 shows the reduction in hit density in the tracker system when the time window $[-3\sigma_T, +5\sigma_T]$ (σ_T is the time resolution of the detector) is applied to reconstructed hits. The bottom part in the same figure shows the polar distribution of all BIB hits before and after the time cut, proving that the background particles are more abundant in the backward and forward regions with respect to the central one.

The high occupancy issue is also a computational problem for the tracking stage. Although the time cut provides a substantial reduction of hit density, it is still unsatisfactory, as the track reconstruction of an event with full BIB overlay takes more than one day. A new strategy based on the double-layer sensor arrangement is currently under development and aim to reduce the reconstruction time to few minutes [50].

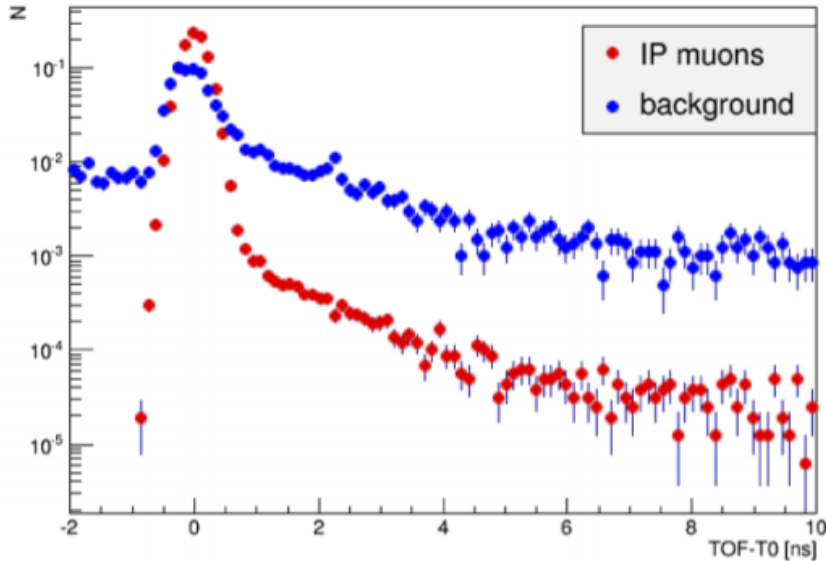


Figure 2.13: Simulated time of arrival (TOF) of the beam background particles to the tracker modules, summing up all the modules, with respect to the expected time (T_0) of a photon emitted from the interaction point and arriving at the same module [48].

For what concern the calorimeters, BIB generates an almost flat noise distribution in each tower, as visible on top of Figure 2.15. This noise can be reduced by applying an energy correction in the process of jet reconstruction [51]. The time of the energy deposition in each tower can be exploited to suppress the BIB. On bottom of Figure 2.15, the time distribution of BIB clusters is shown in black and compared to that of prompt muons in red.

The late component can be removed by applying a proper time window that has to be optimized tower by tower. This strategy is currently under optimization. For the analysis performed in this thesis the time window is fixed at 10 ns for each cell.

Finally, recent studies proved that the BIB does not affect the muon chambers in the barrel region, while in the endcap few geometrical and kinematic requirements can remove completely the BIB tracks [52].

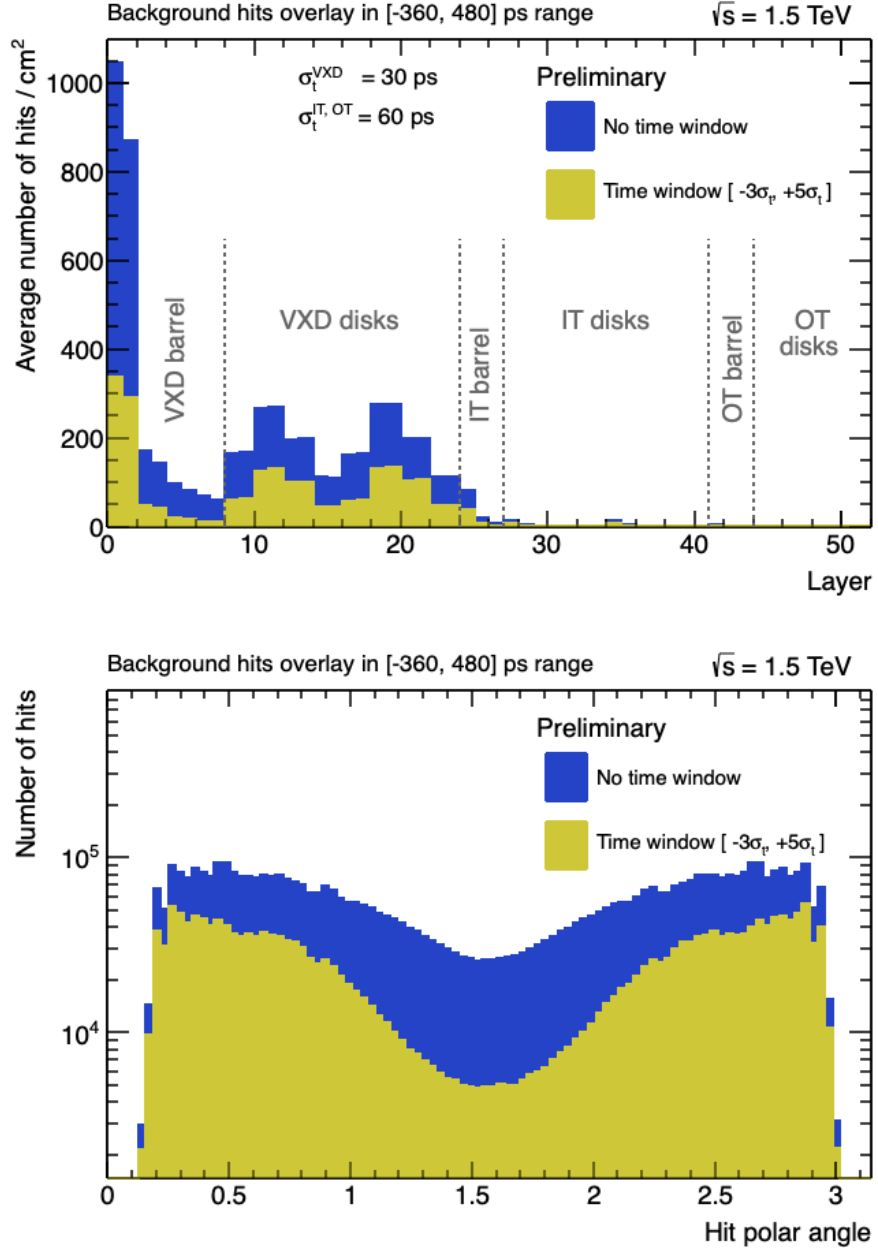


Figure 2.14: Average density of BIB hits in the tracker layers per bunch-crossing (top) and polar angle distribution of the BIB hits for one bunch-crossing (bottom) [49].

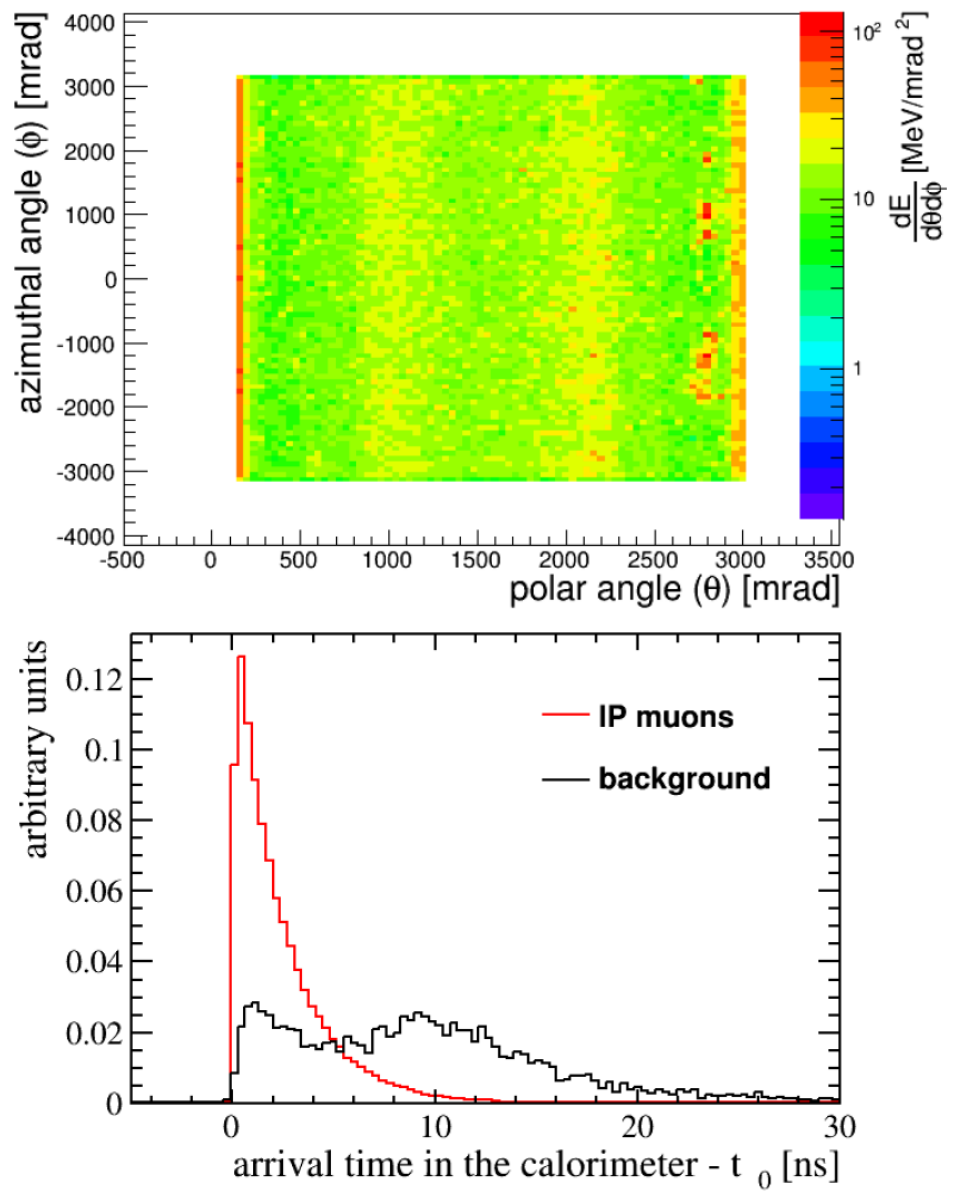


Figure 2.15: BIB energy distribution in the calorimeter (top) and distribution of the arrival time at a given calorimetry position of BIB particles and prompt muons (bottom). Particle arrival time is measured with respect to t_0 , defined as the arrival time in the given position of a photon produced in the primary vertex at the collision time [31].

Chapter 3

Event reconstruction at Muon Collider

In this chapter the steps of the full event reconstruction are described with a focus on complex objects as jets and secondary vertices (SV), since they represent the building blocks of the work in this thesis.

After a brief overview of the software tools needed to perform the complete analysis, the chapter follows the reconstruction flow step by step:

- Track reconstruction in the tracking system.
- Identification of hadrons, muons, electrons and photons via Particle Flow.
- Jet reconstruction with FastJet software package [53].
- Secondary vertex finding with LCFIPlus software [54].

In particular, in this work I have evaluated the jet reconstruction efficiency and resolution as a function of the jet transverse momentum and pseudorapidity. Furthermore, I have carried out an optimization procedure to choose the configuration parameters for the vertex finder, as it has never been used in Muon Collider studies before.

3.1 Software tools

Event simulation and reconstruction for Muon Collider studies are performed with ILCSoft [55]. ILCSoft is a sophisticated modular software developed for the International Linear Collider (ILC), whose key core components are:

- LCIO [56], a complete persistency framework which provides a common data model, a user interface and a file format for the simulation and reconstruction stages.
- DD4HEP [57], a general detector description toolkit, that uses the ROOT geometry package [58] to provide 3D visualization functionality (useful for building detector and event displays) together with the Geant4 package [59] to simulate the detector response from particle collisions in complex designs.

- Marlin [60], the application framework, which handles the digitisation of simulated data, event reconstruction as well as analysis tools, by means of different modules called *processors*. The framework reads data event by event creating an *LCEvent*, a set of collections holding objects like hits, tracks, cluster etc., which is used to hand the data from processor to processor during a Marlin run. The most important and complex package is *MarlinReco*, a specific set of processors for a complete event reconstruction system, based on the Particle Flow concept.

In the next paragraphs the main steps of the reconstruction are outlined.

3.2 Track reconstruction

Track reconstruction consists of using a sequence of algorithms to estimate momentum and position parameters of a charged particle crossing the detector. In this section the track parametrization is firstly presented with a description of the variables needed to define uniquely a track in space. Then the algorithms used for reconstruction are outlined, describing separately the two main processes of track finding and fitting.

3.2.1 Track parametrization

Whenever a charged particle is affected by a constant magnetic field, B , it moves on a helicoidal trajectory, if energy loss and multiple scattering are neglected. This is the case in the Muon Collider detector, where the magnetic field is practically constant and parallel to the beam axis.

In this conditions, the parametrization of a charged particle trajectory can be defined by [61] a reference point $P^r = (P_x^r, P_y^r, P_z^r)$, generally taken as $(0,0,0)$, and five track parameters $(\Omega, \phi_0, D_0, Z_0, \tan\lambda)$. These parameters are evaluated in a specific point $P^0 = (P_x^0, P_y^0, P_z^0)$ along the helix, usually chosen as the point of closest approach (p.c.a.) to the P^r in the xy plane.

In order to explain this parametrization, the trajectory of a particle is projected in two planes: the xy projection is an arc of a circle, while the displacement along z is a linear function of the arc length, s , such that the sz projection is a straight line (Figure 3.1).

In the xy plane the trajectory is specified by the point $P^r = (P_x^r, P_y^r)$ and the parameters Ω , ϕ_0 and D_0 , where:

- ϕ_0 is the azimuthal angle of the track tangent (i.e. of the track momentum) at p.c.a. P^0 .
- Ω is the curvature of the track with a sign defined according to the following convention: when moving along the track in the direction of the particle's momentum if the arc is travelled in the clock-wise direction the sign is positive, negative otherwise.

- D_0 is the signed impact parameter in the xy plane. It is defined as the projection in the transverse plane of the vector pointing from the reference point P^r to the p.c.a. P^0 :

$$D_0 = -(P_x^r - P_x^0) \sin \phi_0 + (P_y^r - P_y^0) \cos \phi_0 \quad (3.1)$$

The signing convention is defined as follows: looking from the P^r to P^0 if the particle travels from left to right the parameter is taken as positive, negative otherwise.

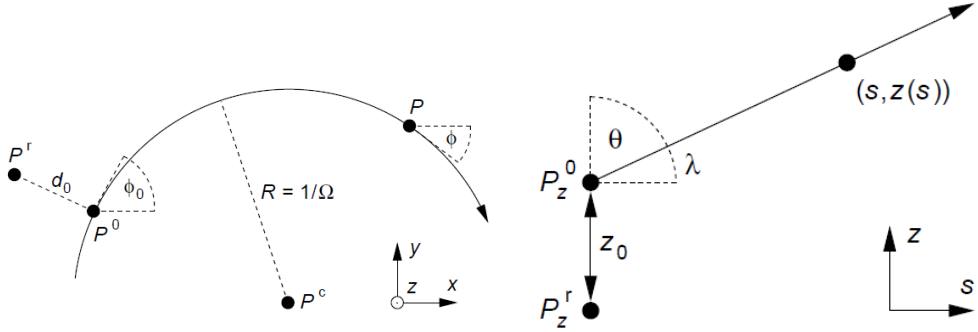


Figure 3.1: Projection of a helix in the xy (left) and sz (right) plane.

In the sz plane the trajectory is a straight line described by the parameters $\tan\lambda$ and Z_0 , where:

- $\tan\lambda$ is the slope of the straight line. It is related to the polar angle θ of the track momentum $p = (p_x, p_y, p_z)$:

$$\tan\lambda = \frac{p_z}{\sqrt{p_x^2 + p_y^2}} = \cot\theta \quad (3.2)$$

- Z_0 is the longitudinal impact parameter define simply as:

$$Z_0 = P_z^0 - P_z^r \quad (3.3)$$

These geometrical parameters are used to get the physics track variables (momentum and charge). In particular, the curvature gives hint on the charge (Eq. 3.4) and on the transverse momentum, p_T (Eq. 3.11):

$$q = \text{sgn} \left(\frac{B_z}{\Omega} \right) \quad (3.4)$$

$$p_T = a \left| \frac{B_z}{\Omega} \right| \quad (3.5)$$

where $a = 3 \times 10^{-4}$, if p_T is measured in GeV, B_z in Tesla, Ω in mm^{-1} . Then the p_T is used to compute the total momentum magnitude (Eq. 3.6) and the three momentum components (Eq. 3.7) using $\tan\lambda$ and ϕ :

$$p = \frac{p_T}{\cos\lambda} = p_T \sqrt{1 + \tan^2\lambda} \quad (3.6)$$

$$\begin{aligned} p_x &= p_T \cos\phi_0 \\ p_y &= p_T \sin\phi_0 \\ p_z &= p_T \tan\lambda \end{aligned} \quad (3.7)$$

3.2.2 Track finding

The track finder algorithm takes the reconstructed hits as input and groups them into track candidates. At Muon Collider the track finding procedure is particularly challenging in terms of required computational time since the hit density is dramatically high due to the Beam Induced Background. In order to reduce the occupancy in the tracking system, only hits detected in the $[-3 \sigma_T, +5 \sigma_T]$ time window are selected (time window depends on detector time resolution, σ_T , see section 2.2.1). Moreover few spacial requirements are also added through the Double Layer Filter. This processor uses the double-layer sensor arrangement for selecting hits that are close-by on the two sublayers, setting a threshold on the maximum allowed distance in the local and global coordinates between pairs of hits at the inner and outer layer [62].

Many different track finding techniques exist. The strategy adopted for the Muon Collider is the Conformal Tracking [63].

The Conformal Tracking algorithm is based on the conformal mapping method and the cellular automaton-based track finding which will be now explained.

In the conformal mapping, Euclidean coordinates (x, y) are transformed into Conformal ones (u, v) defined by the following transformation:

$$u = \frac{x}{x^2 + y^2}, \quad v = \frac{y}{x^2 + y^2} \quad (3.8)$$

The idea is that with this transformation, circumferences passing through the origin in the Euclidean space become straight lines in the new coordinate system. In this way finding bent tracks now becomes a matter of searching straight lines. The radial order of the hit positions is inverted in the conformal space with respect to the global space: hits on the innermost part of the detector are mapped to outer regions in the (u, v) plane and vice versa.

A pattern recognition technique cannot simply group hits aligned in the same direction in the conformal plane, because of deviations from straight line path that can occur for example in the case of displaced tracks or multiple-scattered tracks. By performing the pattern recognition in the conformal space with a cellular automaton (CA), these deviations are taken into account.

Full tracks are then created by the CA algorithm [64] in two steps:

1. *Cellular track candidates are built*

Each hit of the selected collection is taken as a seed. From each seed, a search for neighbouring hits is performed in polar angle¹: hits with a polar angle within the window $[\Theta_{seed} - \Delta\Theta_{neighbours}, \Theta_{seed} + \Delta\Theta_{neighbours}]$ are considered, where $\Delta\Theta_{neighbours}$ is a fixed parameter and Θ_{seed} is the polar coordinate of the seed hit. Segments connecting the seed to each neighbour hit are called *seed cells*. These cells are allowed to have up to a maximum length defined by the l_{max} parameter.

¹Defined as $\Theta = \arctan(u/v) + \pi$

Once all *seed cells* are created from one seed hit, they are extrapolated along the cell direction for a given distance, before a new nearest-neighbour search is performed from the extrapolated points. This time the search is performed in magnitude of conformal radius, i.e. within the search window $[R_{\text{seed_hit}} - \Delta R_{\text{neighbours}}, R_{\text{seed_hit}} + \Delta R_{\text{neighbours}}]$, where $\Delta R_{\text{neighbours}}$ is a fixed parameter. New cells connecting the end point of the *seed cell* and the new neighbours are created. They are allowed to have up to a maximum angle separation from the seed cell of α_{\max} . A cell contains information about its start and its end point as well as a *weight* that tells how many other cells are further connected to it. Each subsequent link increments the cell weight by 1 unit, such that the higher the weight, the higher the potential of the cell to make a track. *Cellular tracks* are chains of cells, made by following the paths leading from the highest-weighted cells back to the seed hit. If more than one path is available, the *cellular tracks* are branched and all possible paths are kept at this level. A minimum number of hits, N_{\min}^{hits} , for each candidate is required.

Once all *cellular tracks* stemming from the seed hit are found, they are fitted with a linear regression in *uv* and *sz* plane, obtaining $\chi^2_{(u,v)}$ and $\chi^2_{(z,s)}$. Only the *cellular tracks* for which neither of the two reduced χ^2 values exceeds a threshold χ^2_{\max} are considered as valid track candidates. The χ^2_{tot} is calculated as the sum of $\chi^2_{(u,v)}$ and $\chi^2_{(z,s)}$.

At this point a further attempt to recover good *cellular tracks* containing a spurious hit is made by removing, one by one, each hit on the track, refitting and recomputing the reduced $\chi^2_{(u,v)}$ and $\chi^2_{(z,s)}$.

Per seed hit, the best track is chosen as the one with best $\chi^2_{\text{tot}}/\text{ndf}$.

A check for clones, i.e. *cellular tracks* with at least two overlapping hits, allows the longest track to be retained by preference, unless the $\chi^2_{\text{tot}}/\text{ndf}$ is too large and the shortest is preferred.

Hits in the *cellular track* are marked as used and the pattern recognition is repeated with the other hits in the collection.

2. Extension of cellular track candidates

For each *cellular track candidate* an estimation of the particle transverse momentum is obtained using the parameters extracted from the linear regression fit. Slightly different approaches are followed for track candidates with an estimated transverse momentum above or below a given threshold $p_{T_{\text{cut}}}$. The extension of the higher- p_T tracks is performed first. The endpoints of the previously formed *cellular tracks* are used as seed hits and a search for nearest neighbours in polar angle is performed, although limited to hits in the adjacent detector layer.

New *cellular tracks* are created as the track candidates are extended to every valid neighbour, among which the best track candidate is chosen based on the smallest reduced χ^2_{tot} . Such extension of the track candidate with the best hit per layer is repeated until the last detector layer.

Finally, the extension procedure is performed with the unused hits for finding lower- p_T tracks. Since their trajectories deviate from the straight lines in conformal space due to multiple scattering, the nearest neigh-

bour search is avoided at this point. All the unused hits are considered for track extension, provided that they are not located on the other side of the detector in z with respect to the seed hit. The subsequent steps remain basically the same.

Table 3.1 summarizes the full pattern recognition chain and reports the values of the parameters used in the CA-based track finding. For all the steps, $\Delta\Theta_{neighbours}$ is fixed at 0.05 rad, $\Delta R_{neighbours}$ is set to 70% of the l_{max} of the current step and p_T at 1.0 GeV.

The pattern recognition is one of the main challenges at a Muon Collider, due to the high occupancy in the innermost layers generated by the Beam Induced Background. Effort is focused on reaching an optimized and final configuration for the steps and parameters of the Conformal Tracking.

Step	Algorithm	Hit Collection	Parameters			
			α_{max} [rad]	l_{max} [mm ⁻¹]	N_{min}^{hits}	χ^2_{max}
1	Build	VTX B(w/o I-L)+E(I-L only)	0.01	0.01	4	60
2	Extend	VTX E (w/o O-L)	0.01	0.006	4	60
3	Build	VTX B+E (w/o O-L)	0.015	0.02	4	60
4	Extend	VTX E (O-L only)	0.02	0.01	4	60
5	Build	VTX E	0.03	0.02	4	60
6	Extend	VTX B (I-L only)	0.015	0.015	5	60
7	Extend	Tracker	0.04	0.02	6	200

Table 3.1: Overview of the pattern recognition steps and parameters. VTX stands for Vertex Detector, B for Barrel and E for Endcap. I-L and O-L are respectively the Inner and Outer layers of the Vertex Detectors.

3.2.3 Track fitting

For each *cellular* track candidate reconstructed during the pattern recognition stage, the track fit is run with the aim of obtaining a precise estimation of the track parameters. It consists of two steps:

1. A pre-fit process, in which a simple helix is fitted to three hits of the track to obtain a first estimation of the trajectory parameters.
2. Kalman filter [65][66] application, initialized with the pre-fit parameters. Starting from the innermost to the outermost layer of the detector the Kalman filter proceeds through the full list of hits on the track, and updates track vector parameters every time an hit is added. It also takes into account multiple scattering and energy loss effect which prevent the tracks to be a perfect helix.

3.3 Particle Flow

Particle reconstruction at Muon Collider makes use of a novel approach to calorimetry that aims to improve the jet energy resolution: the Pandora Par-

ticle Flow algorithm [67].

A traditional approach would measure the jet energy through information of energy deposit in electromagnetic (ECAL) and hadronic (HCAL) calorimeters. This implies that, considering the average composition of jets, about 72% of the energy is deposited in the HCAL. A typical resolution for this detector is about $55\%/\sqrt{E/GeV}$ or more, clearly representing the major limitation to the achievable energy resolution.

The idea of particle flow calorimetry is that the energy and momentum for each particle can be extracted from the subdetector system in which the measurement is expected to be the most accurate. In this way, the inner tracker can be exploited for measuring with precision charged particle momenta (resolution of the order of percent), the ECAL gives information on photon energy with a typical resolution of less than $20\%/\sqrt{E/GeV}$, while the HCAL is only used to measure the 10% of jet energy that is carried out by neutral hadrons (Figure 3.2).

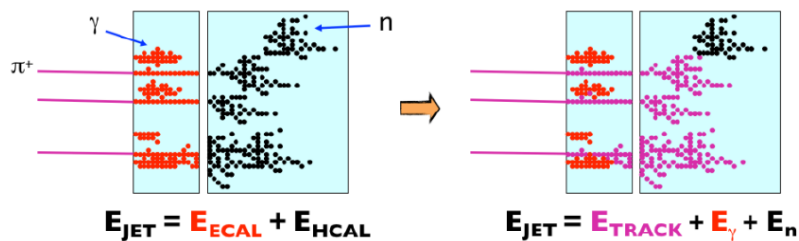


Figure 3.2: Schematic representation of a traditional energy reconstruction algorithm (left) opposed to a the new particle flow approach (right).

Particle Flow Calorimetry requires both fine granularity calorimeters, to cleanly separate depositions of different particles, and sophisticated software algorithms for pattern recognition. Failure to provide these requirements will likely lead to *confusion* in the particle reconstruction. This *confusion* represents the limiting factor in the process.

There could be three types of mistakes, schematically represented in Figure 3.3:

- Failure to resolve photons from nearby charged hadrons. In this case the photon energy deposit is added to that of the charged particle but the four-momentum is calculated from tracker measurements, thus energy loss occur.
- Failure to resolve neutrons. Same considerations of previous point hold.
- Failure to link all the calorimeter energy deposits to the corresponding track, in case of charged particles. This mistake leads to double counting of energy: while the track is used to provide the four-momentum vector for the charged particle, the unassociated fragment in the calorimeter is reconstructed as a separate neutral hadron.

In order to fully exploit particle flow calorimetry, the *confusion* is reduced to the lowest possible level, by using fine granularity calorimeters and an accurate

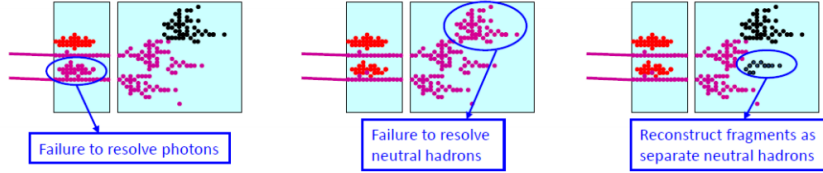


Figure 3.3: Schematic representation of the three main types of failures in the Particle Flow Calorimetry.

tracker system.

Moreover, the request for an efficient pattern reconstruction algorithm is satisfied by using the *PandoraPFA* processor [68], implemented in the framework of the ILCSoft.

The main reconstruction steps performed by *PandoraPFA* are the following:

1. *Cone clustering of the calorimeter hits*

Clusters are seeded by projections of inner detector tracks to the surface of the ECAL. Starting from the innermost layers and working outward, each calorimeter hit is considered in turn: if the hit lies within the cone defined by the existing cluster it is added to the cluster, otherwise it is used to form a new cluster (Figure 3.4).

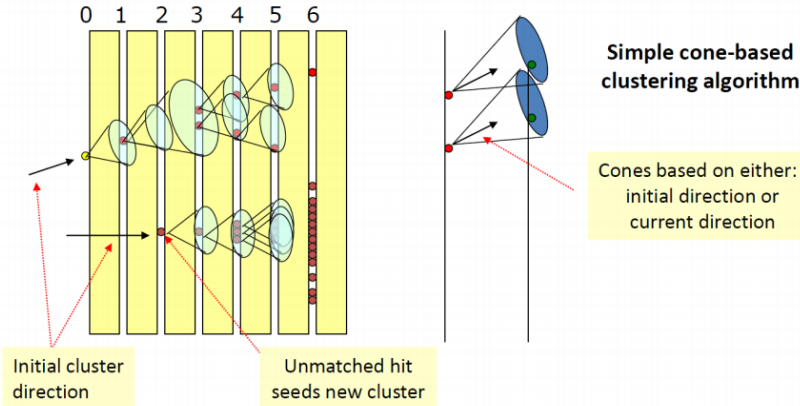


Figure 3.4: The cone clustering algorithm explained [69].

2. *Topological cluster association*

Proto-clusters built in the previous step are merged together by a series of algorithms that implement well-motivated topological rules (recurring topologies are illustrated in Figure 3.5).

3. *Track-Cluster association*

Calorimeter clusters are associated to inner tracks, by looking for consistency between cluster features and the helix-projected track state at the front face of the calorimeter.

4. *Statistical reclustering*

If significant discrepancy between energy of a cluster and momentum of the associated track is found, a reclustering is performed. The algorithm

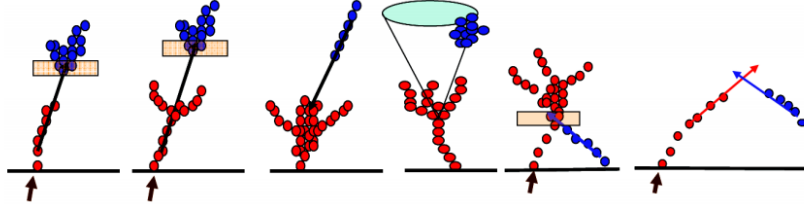


Figure 3.5: Some clear recurring topologies [69].

check if different clustering configurations with a better track-cluster compatibility exist.

5. Fragment removal

This algorithm tries to remove neutral clusters that are erroneously unmatched fragments of charged clusters. It searches for evidence of association between these clusters and evaluates the changes in track-cluster compatibility that would occur if the clusters were merged. Some examples of recurring situations are shown in Figure 3.6.

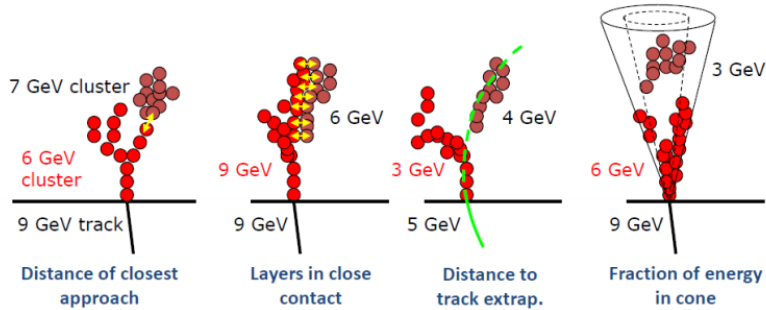


Figure 3.6: Fragment removal examples [69].

6. Particle Flow object formation

Particle objects are built from track and associated clusters.

Finally, specific algorithms for particle identification combines the information in all the above mentioned sub-detectors, in order to unambiguously flag possible candidates for muons, electrons, photons, neutrons and charged hadrons.

At the end, the energy resolution appears to be not critical, since most of the information comes from the track system. The error is dominated by the precision of the track-cluster association.

The particle flow approach to calorimetry is the key point for reaching the jet energy resolution needed to accomplish relevant physics goals at future collider machines.

In the next paragraph, the jet reconstruction itself is outlined in detail, together with a presentation of resolution studies carried out on a sample of c jets at $\sqrt{s} = 1.5$ TeV.

3.4 Jet Reconstruction

When studying high-energy collisions, it is often necessary to consider processes where quarks and gluons are produced in the final-state. For example, in the LEP (Large Electron-Positron Collider) era, the study of hadronic final-states was essential to establish QCD as the fundamental theory of strong interactions. Today at the LHC, the list of processes involving high-energy quarks and/or gluons in their final state is even longer.

As mentioned in section 1.1, only colorless final states are directly observable, as quarks and gluons hadronize producing jets.

Jets are defined on the basis of the clustering algorithm and recombination scheme adopted [70]:

- The clustering algorithm is the recipe and the set of parameters needed for combining together reconstructed particles into jet objects. A typical parameter is the jet radius which provides a distance in the rapidity-azimuth ($y - \phi$) plane above which two particles are no longer considered as collinear.
- The recombination scheme is the rule for evaluating the kinematic properties of the jet from its constituents. A well-known example, which is also used in this work, is the *E-scheme* that sums up the components of the hadron four-momenta to calculate the four-momentum of the jet.

Several jet finding algorithms exist and, in the framework of the ILCSoft, they are provided by the FastJet processor [53]. In this analysis a sequential recombination algorithm is chosen, the *longitudinally invariant k_T algorithm*, in its inclusive form.

This kind of algorithm tries to invert the process that leads to parton shower, by successively recombining two particles into one on the base of a specifically customized metric.

The inclusive k_T algorithm is formulated as follows:

1. The reconstructed particles in the event are taken in input as initial list of objects.
2. From the list of objects, two sets of distances are built:
 - an *inter-particle distance*

$$d_{ij} = \min(p_{T_i}^2, p_{T_j}^2) \frac{\Delta R_{ij}^2}{R^2} \quad (3.9)$$

with $\Delta R_{ij}^2 = (y_i - y_j)^2 + (\phi_i - \phi_j)^2$, where p_{T_i} , y_i and ϕ_i are the transverse momentum, rapidity and azimuth of the i -th particle while R is the radius parameter

- a *beam distance*

$$d_{iB} = p_{T_i}^2 \quad (3.10)$$

3. The smallest distance among all the d_{ij} and d_{iB} is found.
If the smallest distance is a d_{ij} then objects i and j are removed from the list and recombined into a new object k (using the recombination scheme) which is itself added to the list.
Otherwise if the smallest distance is a d_{iB} then the object i is called a *jet* and removed from the list.
4. Steps 2 and 3 are repeated until all the objects in the initial list are exhausted.

For this analysis the R parameter is chosen to be 1.0, the clustering mode is inclusive, as already stated, since the entire event is used to build up jets, and a minimum transverse momentum of 5 GeV is required for the final jet object.

3.4.1 Jet reconstruction efficiency

I have evaluated the jet reconstruction performance using a simulated sample of 10^4 events of $\mu^+\mu^- \rightarrow H\nu\bar{\nu} \rightarrow c\bar{c}\nu\bar{\nu}$ at $\sqrt{s} = 1.5 \text{ TeV}$, without the BIB overlay.

The reconstructed jets, *RECO-jets*, are formed feeding the algorithm explained in section 3.4 with the output collection of Particle Flow (section 3.3). In order to assess the goodness of this reconstruction, the Monte Carlo jets, *MC-jets*, are also formed by clustering the stable truth-level particles (lifetime $> 10^{-8} \text{ s}$) excluding neutrinos. Since these particles have the true kinematic quantities, they are useful to determine how the detector efficiency affects the jet reconstruction.

Firstly, *MC-jets* are flagged as:

- b jets, if they contain at least a b hadron at Monte Carlo level, i.e. $\Delta R = \sqrt{\Delta\eta^2 + \Delta\phi^2}$ between jet axis² and b hadron momentum is less than 1.0.
- c jets, if they contain no b hadron but at least a c hadron.
- light-flavour jets, if they contain neither b nor c hadron.

Then, *RECO-jets* are matched with c-tagged *MC-jets* by choosing the closest *RECO-MC* jet pair in the (η, ϕ) plane within $\Delta R < 0.5$.

The jet reconstruction efficiency is defined as the ratio between the number of c-tagged *MC-jets* matched with a *RECO-jet* and the total number of c-tagged *MC-jets*. In Figure 3.7 the efficiency is reported as a function of jet p_T and η . It increases with increasing momentum, exceeding 90% for $p_T > 20 \text{ GeV}$ and approaching 100% for $p_T > 80 \text{ GeV}$. The efficiency is almost constant in η , above 98%, but a slight decrease for $\eta > 2$ is visible and expected since the maximum acceptance of the detector is reached.

For each pair (*MC-jet*, *RECO-jet*) the following ratios are evaluated:

$$\frac{\Delta p_T}{p_{T_{MC}}} = \frac{p_{T_{MC}} - p_{T_{RECO}}}{p_{T_{MC}}} \quad (3.11)$$

²The jet axis is defined by the primary vertex and the direction of the jet momentum.

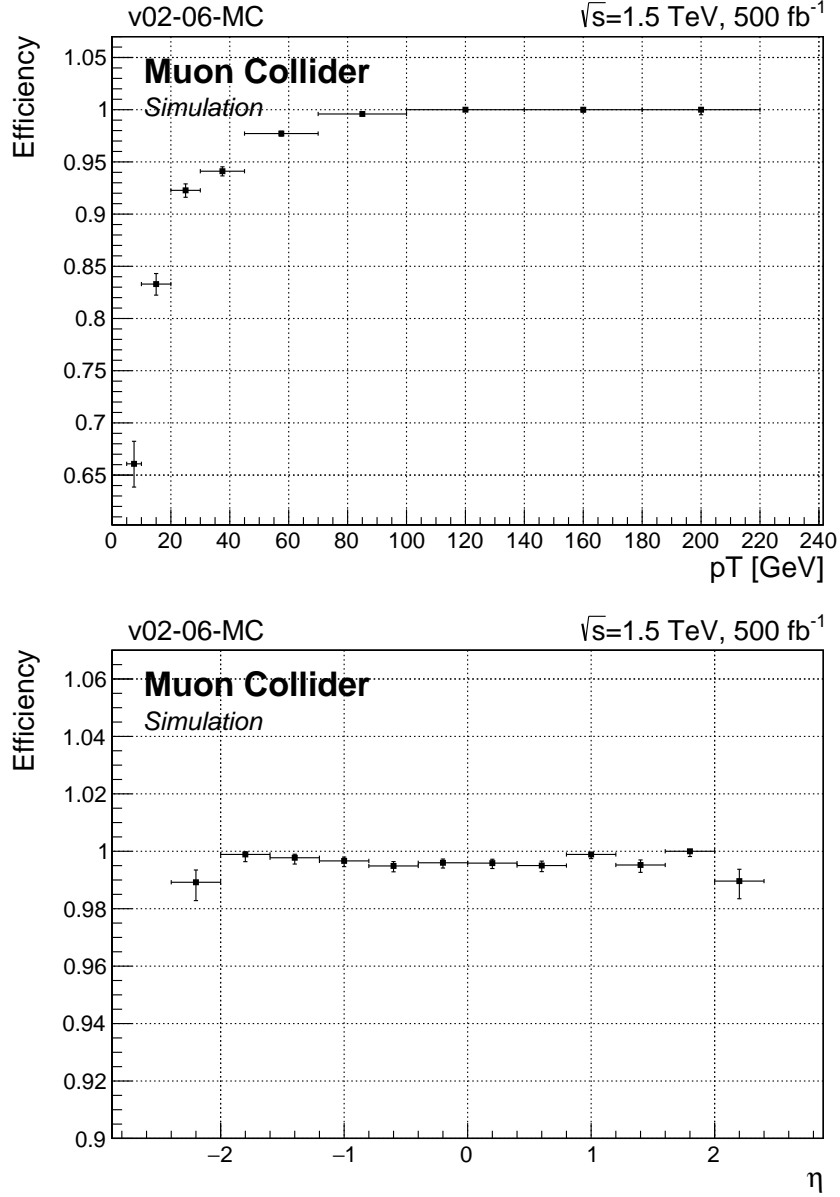


Figure 3.7: Jet reconstruction efficiency versus transverse momentum (top) and pseudorapidity (bottom).

$$\frac{\Delta E}{E_{MC}} = \frac{E_{MC} - E_{RECO}}{E_{MC}} \quad (3.12)$$

where $p_{T_{MC}}$ and E_{MC} are the transverse momentum and the energy of the *MC-jets*, while $p_{T_{RECO}}$ and E_{RECO} are the transverse momentum and the energy of the *RECO-jets*. The distributions of the variables in Eq. 3.11 and 3.12 are considered in different ranges of *MC-jet* p_T and η (examples in Figures 3.8 and 3.9). The distributions are then fitted with a gaussian function, whose width is taken as the final transverse momentum and energy resolution. These values are quoted in Figures 3.10 and 3.11.

The energy and transverse momentum resolutions are $\lesssim 10\%$ for $p_T > 10$ GeV and $\lesssim 5\%$ for $p_T > 80$ GeV. The behaviour in η shows a little degradation in resolution for the $\eta = 0$ region, as quasi-vertical particles cross less material

budget with respect to oblique ones and can be not completely absorbed by the detector. In addition, a higher degradation for η approaching the detector maximum acceptance can be seen.

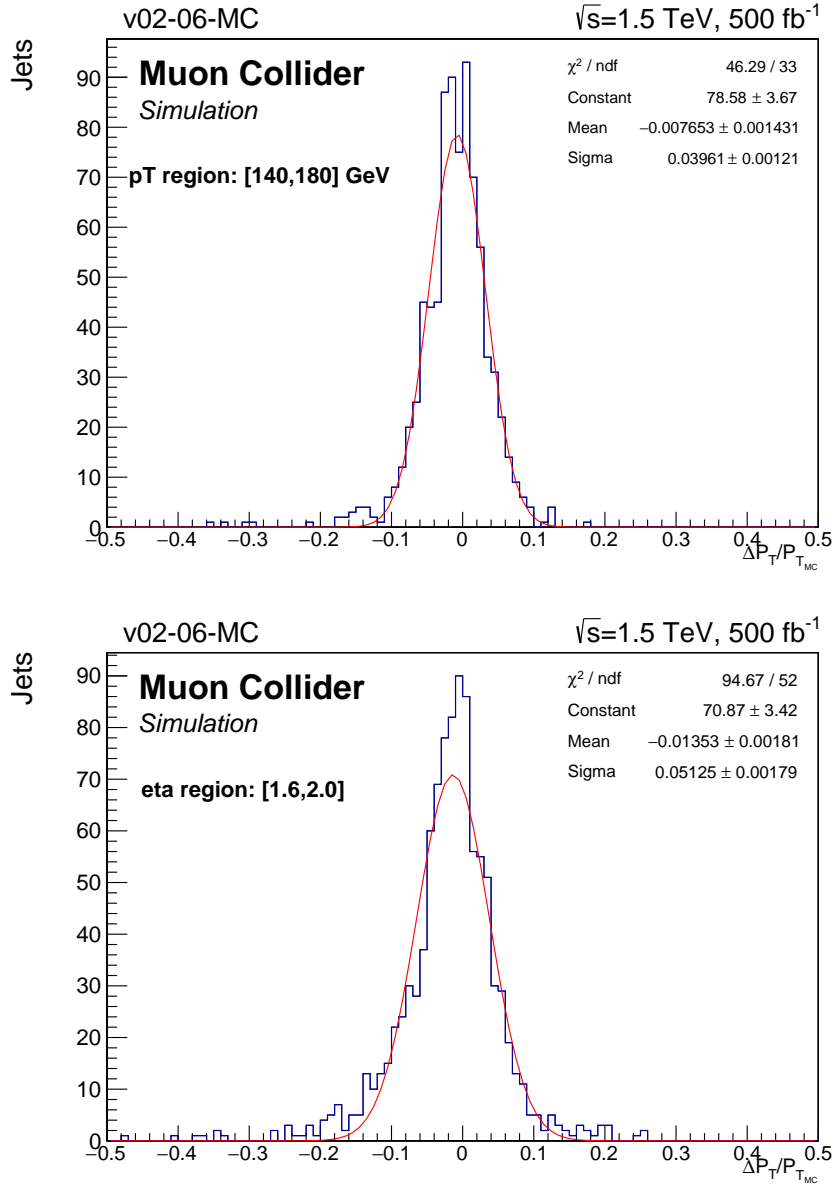


Figure 3.8: Distribution of the variable $\Delta p_T / p_{T_{MC}}$ in the *MC-jet* transverse momentum region [140, 180] GeV (top) and *MC-jet* pseudorapidity region [1.6, 2.0] (bottom). The gaussian fit is overlaid in red.

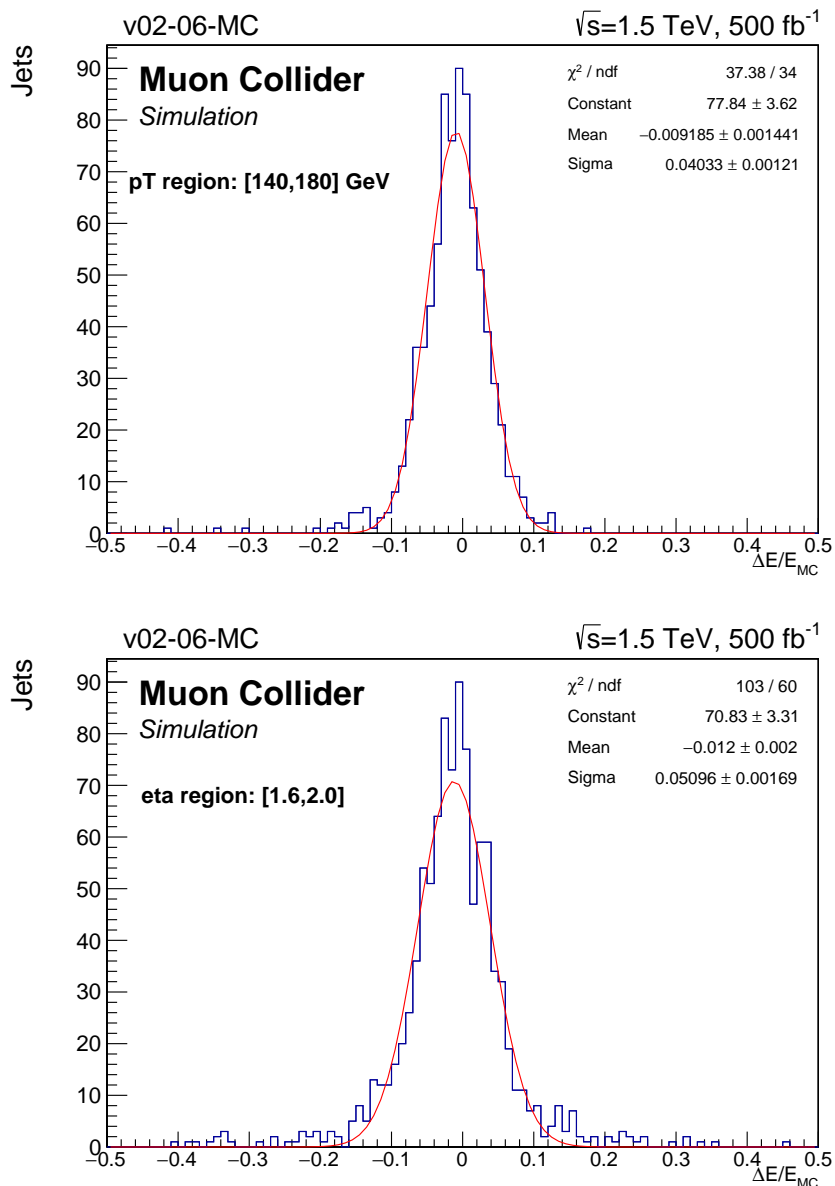


Figure 3.9: Distribution of the variable $\Delta E/E_{MC}$ in the *MC-jet* transverse momentum region [140, 180] GeV (left) and *MC-jet* pseudorapidity region [1.6, 2.0] (right). The gaussian fit is overlaid in red.

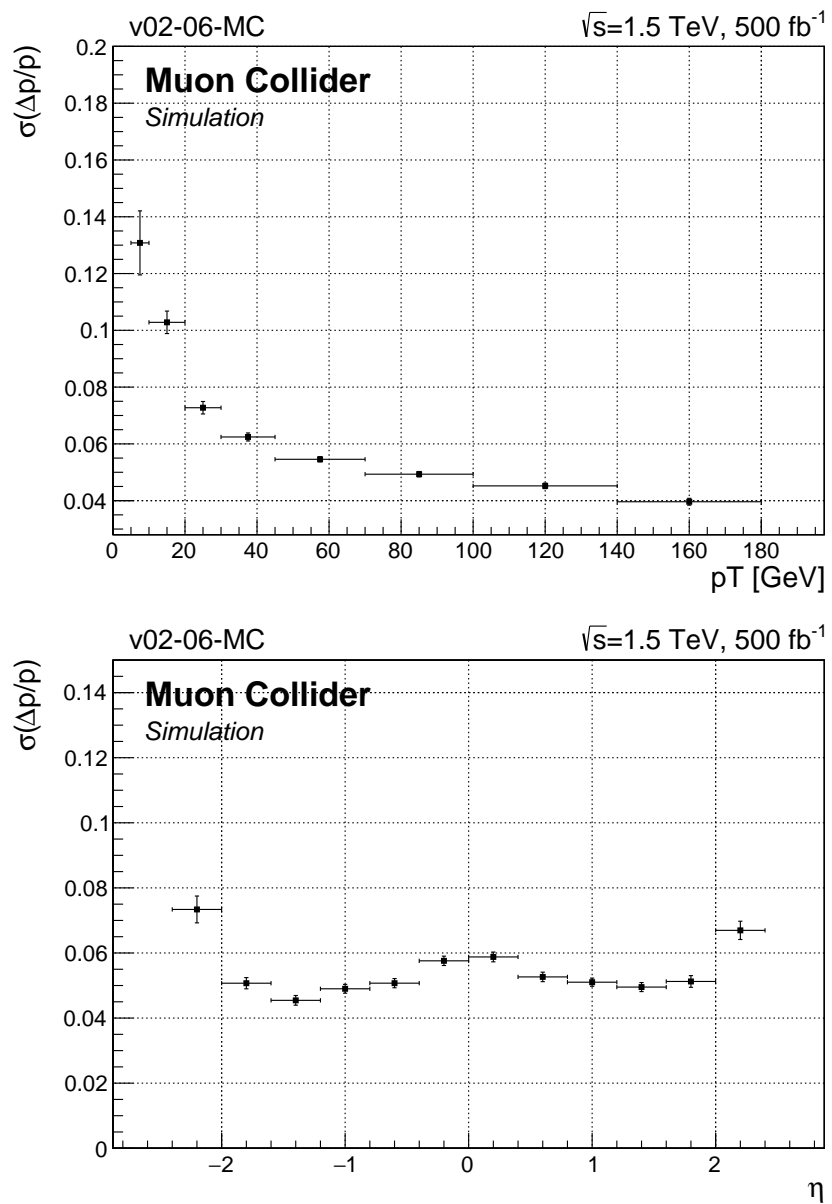


Figure 3.10: Jet transverse momentum resolution versus transverse momentum (top) and pseudorapidity (bottom).

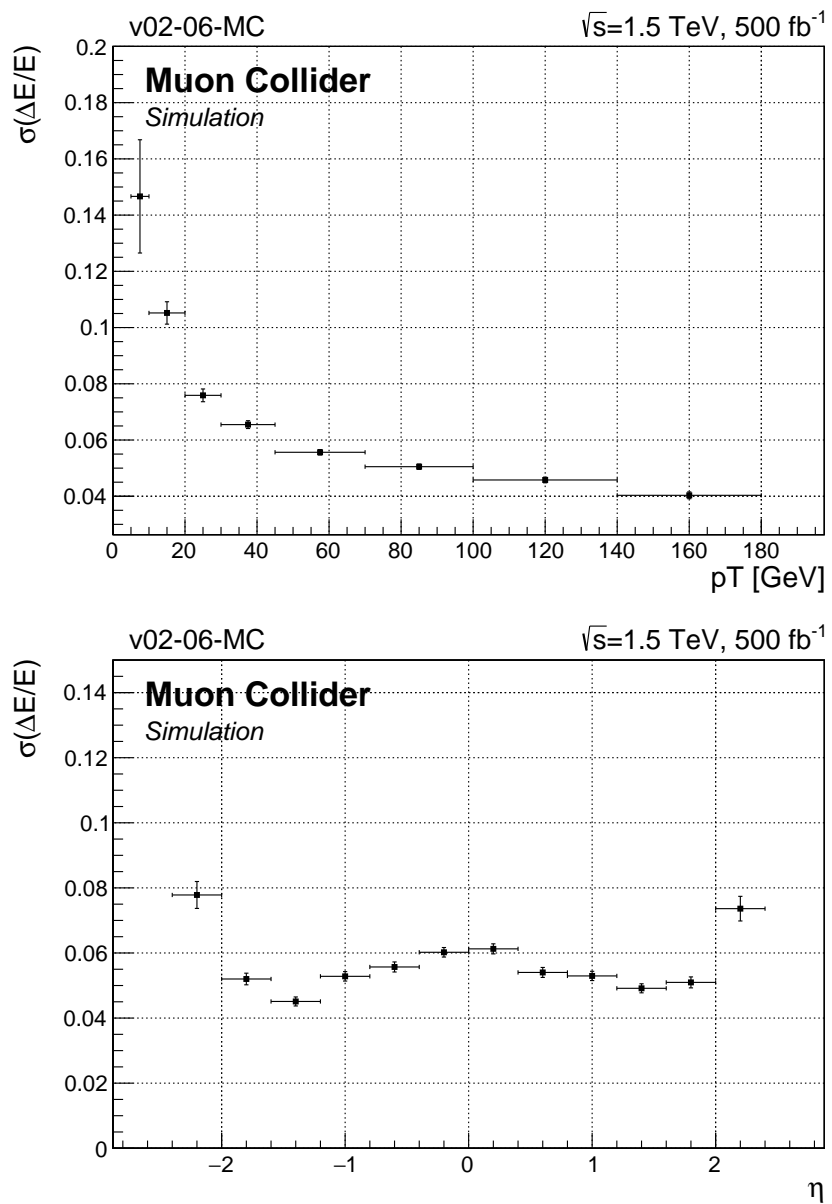


Figure 3.11: Jet energy resolution versus transverse momentum (top) and pseudorapidity (bottom).

3.5 Secondary Vertex Reconstruction

The main feature of jets arising from hadronization of heavy quarks is the presence of secondary vertices related to heavy-hadron decay, since the hadrons containing bottom or charm quarks have sizable lifetimes which can be measured inside the detector. The characteristic flight length, measured in terms of the lifetime at rest τ , is $c\tau = 400 - 500 \mu m$ for bottom hadrons and $c\tau = 20 - 300 \mu m$ for charm hadrons [3]. This leads to typical secondary-to-primary vertex displacements of the order of millimetres or more, depending on the hadron Lorentz factor ($\gamma = E/m$).

In Figure 3.12 the Lorentz factor distribution is reported for c hadrons in the $\mu^+\mu^- \rightarrow H\nu\bar{\nu} \rightarrow c\bar{c}\nu\bar{\nu}$ sample (on the left) and for b hadrons in the $\mu^+\mu^- \rightarrow H\nu\bar{\nu} \rightarrow b\bar{b}\nu\bar{\nu}$ sample (on the right). Both processes are generated at $\sqrt{s} = 1.5$ TeV. The average c hadron boost in $H \rightarrow c\bar{c}$ is 30 while the b hadron boost in $H \rightarrow b\bar{b}$ is smaller, about 20, because of the higher mass³.

These very high boost values cause the decay vertices to be displaced of even few centimetres with respect to the IP, allowing an extremely precise reconstruction.

In Figure 3.13 the distance from the IP of heavy hadron decay points (at Monte Carlo level) is reported for the two physics samples. The average displacement is around 6 mm for $H \rightarrow c\bar{c}$ and 10 mm for $H \rightarrow b\bar{b}$. It is important to remark that b hadrons decay most of the time into final states involving c hadrons. As a consequence, the $H \rightarrow b\bar{b}$ sample contains also c decay vertices, whose distance from IP depends on c hadron flight length as well as on the b hadron parent flight length.

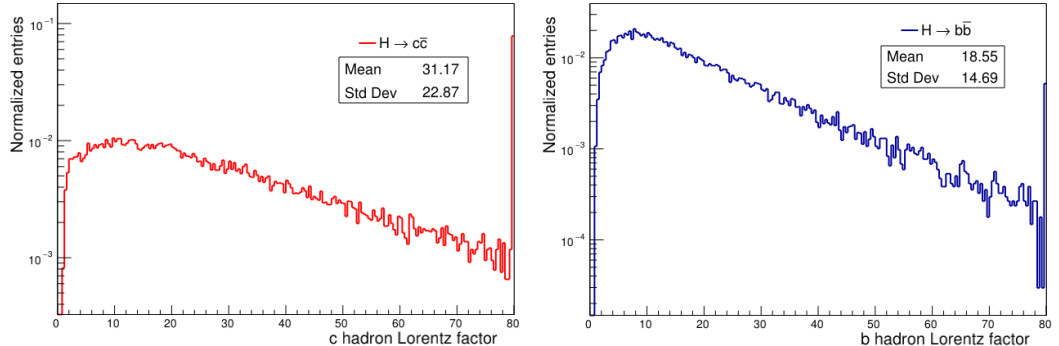


Figure 3.12: Lorentz factor for c hadrons in the $H \rightarrow c\bar{c}$ sample (left) and b hadrons in the $H \rightarrow b\bar{b}$ (right) at $\sqrt{s} = 1.5$ TeV.

The ability to reconstruct the displaced vertices is crucial to discriminate heavy-flavour jets from light-flavour ones. Moreover, reaching very high quality in vertex finding is necessary to exploit the difference between b hadron decay and c hadron decay and achieve the challenging b-to-c jet discrimination.

In this analysis the vertex reconstruction is performed through the LCFIPlus processor implemented in the Marlin framework of ILCSoft. The first part

³The average c hadron mass is 2 GeV, while the average b hadron mass is 5 GeV.

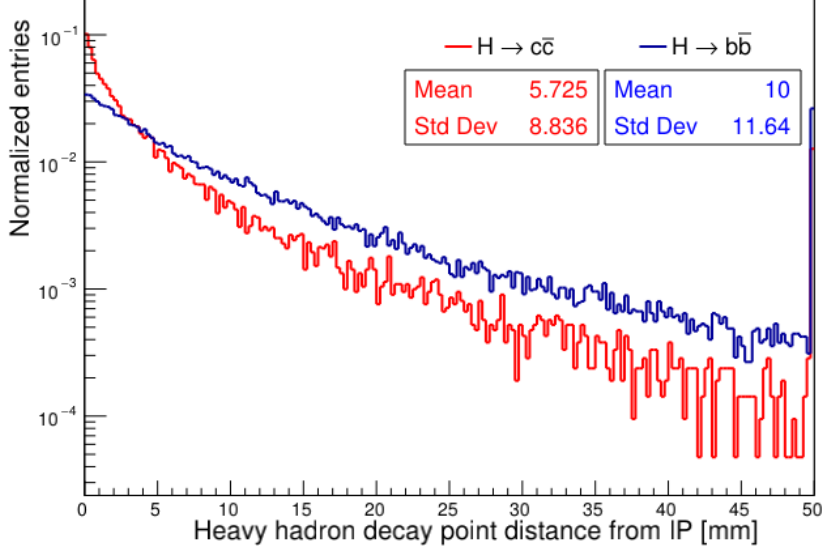


Figure 3.13: Distance from the IP of b hadron and c hadron decay points in the $H \rightarrow c\bar{c}$ sample (red) and in the $H \rightarrow b\bar{b}$ (blue) at $\sqrt{s} = 1.5$ TeV.

of this section is focused on the description of LCFIPlus and its algorithms. Then the track selection needed for vertexing is illustrated. As the LCFIPlus processor has never been employed in the context of Muon Collider studies, I have carried out an optimization procedure to find the proper set of parameters to be adopted in the algorithms. Several attempts were performed with different configurations and tested on 10^3 events of $H \rightarrow b\bar{b}$ and $H \rightarrow c\bar{c}$. The main purpose is to achieve a small contamination (less than few percent) of prompt tracks in the secondary vertices and, at the same time, retain a good reconstruction efficiency for the displaced vertices. The optimization procedure takes the following vertex features as figure of merit:

- The number of tracks from heavy hadron decay wrongly associated to the reconstructed primary vertex (PV) per event (left Figure 3.14) and the number of tracks from IP erroneously associated to the reconstructed secondary vertex (SV) per event (right 3.14).
 - The number of reconstructed SVs per jet (left Figure 3.15), where the association SV-jet is made through a geometrical matching (see section 4.1.2 for further details).
 - The reconstructed mass associated to the SVs (right Figure 3.15), corrected with a procedure that will be later explained in section 4.1.2, to verify that the difference between $H \rightarrow b\bar{b}$ and $H \rightarrow c\bar{c}$ samples is the one expected from the mass hierarchy of heavy hadrons (see Ref. [71] for a comparison).
 - The flight distance of the reconstructed SVs (left Figure 3.16) to check if the distribution is compatible with the Monte Carlo truth (Figure 3.13): as expected, the SV flight distance for vertices in the $H \rightarrow b\bar{b}$ sample is higher, on average, with respect to vertices in $H \rightarrow c\bar{c}$.
- The flight distance is also divided for its error, obtaining the so-called

flight distance significance (right Figure 3.16), to control the uncertainty on the reconstructed position.

The distributions in Figures 3.14-3.16 are shown after the optimization process. The quality of the SV reconstruction is quantified with a method explained in section 3.5.3, where the performance achieved at the end of the optimization procedure is reported and compared to the one found in literature [54].

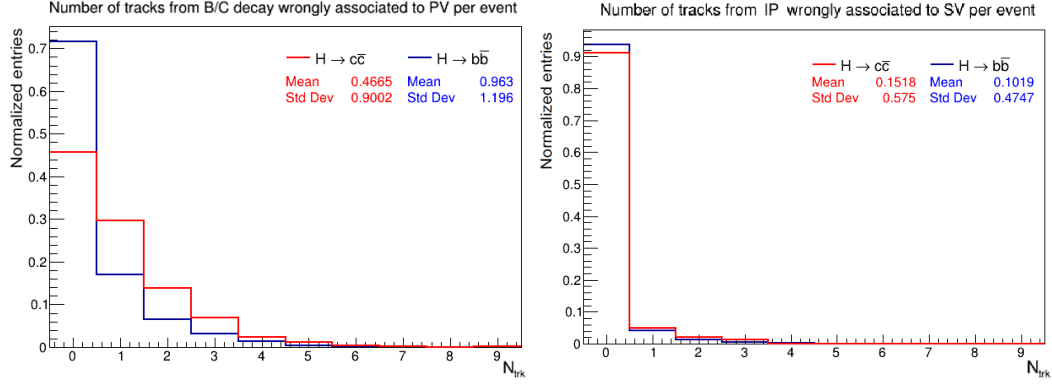


Figure 3.14: Number of tracks wrongly associated to PV per event (left) and number of tracks wrongly associated to SV per event (right) in the $H \rightarrow c\bar{c}$ (red) and $H \rightarrow b\bar{b}$ (blue) samples.

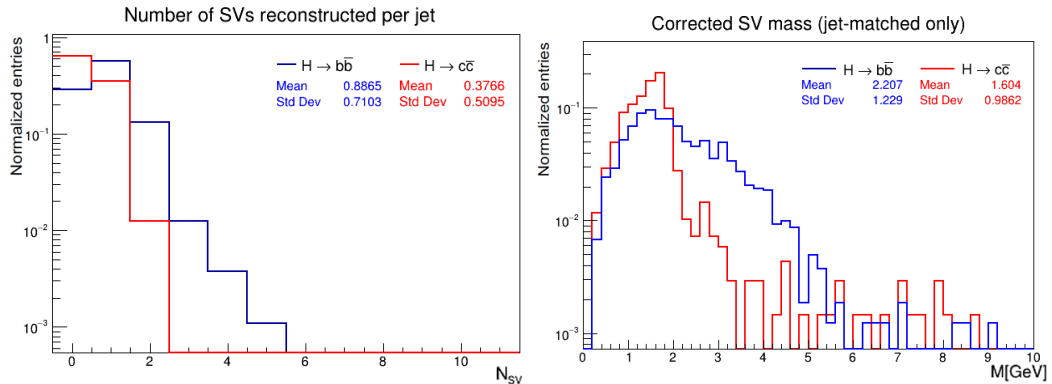


Figure 3.15: Number of SVs reconstructed per jet (left) and corrected mass for SVs matched with a jet (right) in the $H \rightarrow c\bar{c}$ (red) and $H \rightarrow b\bar{b}$ (blue) samples.

3.5.1 LCFIPlus processor

LCFIPlus is a modular software framework, implementing each algorithm as a separate module. In this work, only the high-quality vertex finders algorithms for the reconstruction of the PVs and of SVs are used.

A vertex fitter is implemented in the processor, with the aim of taking a set of tracks in input and calculates the point at which the tracks are likely to have originated. It works as follows [54]:

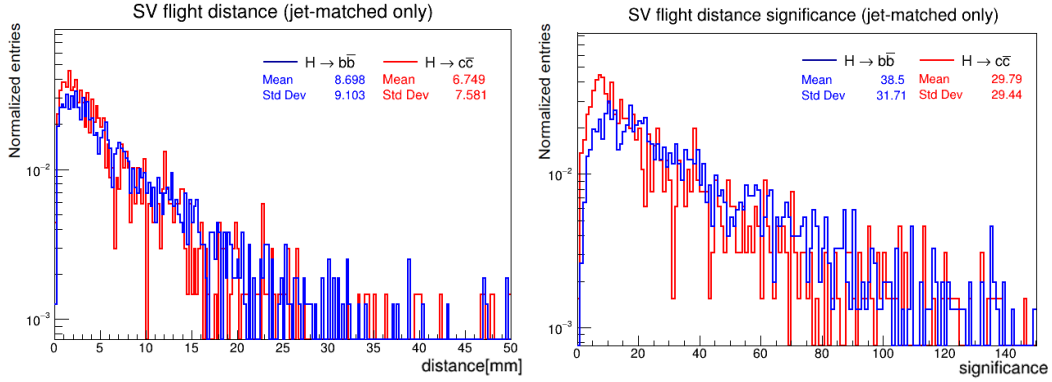


Figure 3.16: Flight distance (left) and flight distance significance (right) for SVs matched with a jet in the $H \rightarrow c\bar{c}$ sample (red) and in the $H \rightarrow b\bar{b}$ (blue).

1. An initial 3D point is specified such that:
 - If there exists a constraint for the fit (as the beam spot one for PV), the initial point is set as the center of the constraint.
 - If no constraint is present, firstly, the two tracks which give the highest vertex probability are chosen. Then the 2D crossing point of the two circles projected from the track helical trajectories is evaluated. The third coordinate (in the direction perpendicular to the projected circles) is determined scanning along the helical trajectory.
2. A 3D fit is performed for the vertex position using the Minuit algorithm as implemented in the ROOT package [72]. The value to be minimized is the χ^2 of the vertex, that is calculated adding the χ^2 contribution of every track to the fitted vertex point.
3. The vertex fitter finally gives as output the minimized vertex χ^2 value and the individual contribution to the χ^2 from each track, the vertex probability and the vertex position and relative uncertainty.

The *Primary Vertex Finder* uses the vertex fitter in this way:

1. The minimized χ^2 is evaluated using all the tracks in the event.
2. The track whose contribution to χ^2 is the greatest (and greater than a set threshold) is removed and the vertex χ^2 recalculated.
3. The step 2 is repeated until the contribution from each remaining track is smaller than the threshold.

In this analysis, I have set the threshold value for track contribution to be 10. Moreover, the beam spot constraint is imposed, considering a beam size in the horizontal and vertical direction (in the plane transverse to the beam axis) of $\sigma_x = \sigma_y = 5.9 \mu m$ and a longitudinal (with respect to the beam axis) size of $\sigma_z = 10 mm$ [73].

The *Secondary Vertex Finder* uses a new strategy for reconstructing SVs with

respect to the conventional one. Traditional vertex finders rely on the jet reconstruction, meaning that only the tracks clustered in jets are used for the fit, in order to reduce the possible number of track combinations. In such methods, vertices are discarded if their position is inconsistent with jet direction, and this could affect the efficiency of SV finding if the jet reconstruction step is inaccurate. The inclusive novel approach used in LCFIPlus processor increases reconstruction efficiency especially in final states involving many jets [54].

The algorithm works as follows:

1. All the tracks not used for the PV fit are used to build all possible track pairs.
2. The χ^2 is computed with the vertex fitter for all track pairs.
3. Several selections are applied on the two-track vertices:
 - Invariant mass of the track pair smaller than a set threshold.
 - Invariant mass of the track pair smaller than the energy of both tracks.
 - Pass of the V^0 rejection for the track pair (see later in the paragraph).
 - Position of the reconstructed vertex on the same side as the sum of the track momentum, with respect to the primary vertex.
 - χ^2 smaller than a set threshold.
4. Additional tracks are then attached to track pairs, given that the same requirements as above are satisfied (except for the V^0 rejection).
5. A procedure based on SV probability is carried out to avoid the usage of a track for more than one vertex.

In this work, a threshold value of 10 GeV for the invariant mass is chosen, in order to be far enough from the heaviest b hadron mass, ~ 6 GeV. A minimum distance from IP is also required, and it's taken as $300 \mu m$, compatible with the minimum flight distance expected for c hadron (considering a Lorentz boost $\gtrsim 10$). The maximum value for χ^2 is chosen as 5.

The V^0 rejection, mentioned in the algorithm flow, is a control procedure to remove the vertices compatible with the decay of the so called V^0 particles. These are neutral particles which decay or convert into a pair of charged tracks, whose signature can mimic the decay of b or c hadrons. The procedure uses a filter based on kinematic variables to remove the following decays/conversion: $K_S^0 \rightarrow \pi^+ \pi^-$, $\Lambda^0 \rightarrow p \pi^-$ and $\gamma X \rightarrow e^+ e^- X$.

Table 3.2 reports the values of the vertexing parameters I have set at the end of the optimization procedure, aiming to maximize the performance shown in Tables 3.4 and 3.5.

PV	χ^2 threshold Beam spot constraint	10 true
SV	χ^2 threshold Mass threshold Min dist from IP V^0 rejection	5 10 GeV 300 μm true

Table 3.2: Parameters set in the PV and SV finder.

3.5.2 Track selection for vertex finding

In order to reduce cross contamination between PV and SV fit, not all reconstructed tracks are given to the the *Primary Vertex Finder* as well as to the *Secondary Vertex Finder*. In this paragraph the preliminary selections applied on tracks are described and motivated.

As already mentioned, the sizeable lifetime of heavy hadrons leads to tracks displaced from PV. These tracks can be used to reconstruct secondary vertices. A useful observable to quantify this displacement is the impact parameter, defined as the distance between the PV and the tracks at their point of closest approach (see section 3.2.1).

This variable can be defined in 3D or in 2D in the plane normal to the beam axis (in this case it is called *transverse impact parameter* and indicated with D_0) or in 1D along the direction of the beam axis (in this sense it is referred to *longitudinal impact parameter*, Z_0).

The variables D_0 and Z_0 represent good discriminators between tracks truly coming from the PV and tracks originated from a heavy hadron decay. In order to prove that and choose the optimal cuts, I have studied the simulated sample of $\mu^+ \mu^- \rightarrow H \nu \bar{\nu} \rightarrow b \bar{b} \nu \bar{\nu}$ at $\sqrt{s} = 1.5 \text{ TeV}$.

In particular two set of tracks are selected according to their properties at generator level:

- *Tracks from heavy hadron decay*, which have a b or c hadron parent at generator level with a non-zero lifetime. These tracks should be used to fit a SV in the vertex finding process.
- *Tracks from hadronization*, which have a starting point far less than 1 μm from the IP at generator level. These tracks come predominantly from the hadronization process or from the strong, i.e. instantaneous, decay of hadrons generated in the hadronization process. They should be used by the vertexing algorithm to fit the PV.

In Figure 3.17 the distributions of D_0 and Z_0 are shown for the two sets of tracks. As expected the impact parameter is much more peaked on zero for the prompt tracks. After the optimization procedure, I set a maximum value

of 0.1 mm for both D_0 and Z_0 in the track selection for the PV fit. In this way tracks with a higher impact parameter are excluded and remain available for the SV fit.

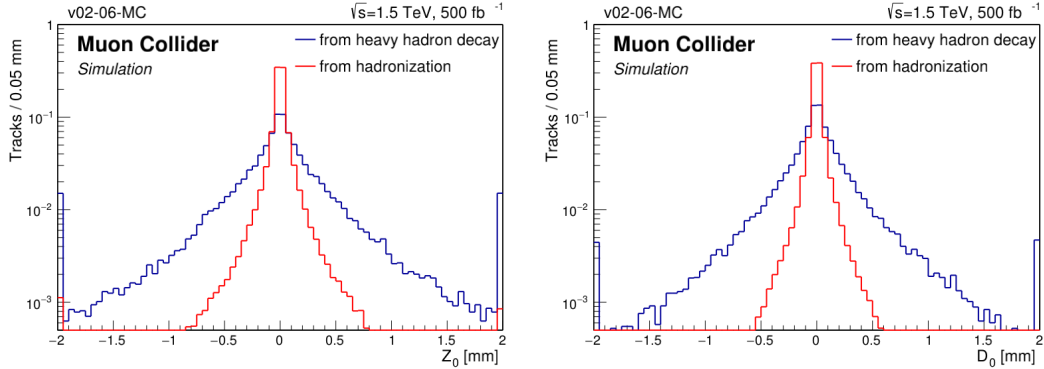


Figure 3.17: Longitudinal impact parameter (left) and transverse impact parameter (right) for the two types of tracks.

Instead of choosing a minimum D_0 or Z_0 for the SV fit, a more discriminating variable is considered, the D_0 - Z_0 significance, defined as:

$$\sqrt{\left(\frac{D_0}{\sigma_{D_0}}\right)^2 + \left(\frac{Z_0}{\sigma_{Z_0}}\right)^2} \quad (3.13)$$

where σ_{D_0} and σ_{Z_0} are the uncertainties on D_0 and Z_0 , respectively (Figure 3.18).

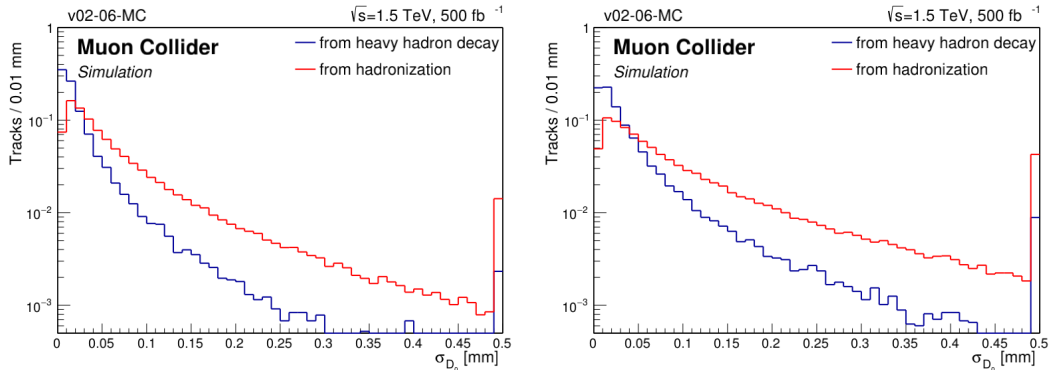


Figure 3.18: Uncertainty on D_0 (left) and Z_0 (right) for the two types of tracks.

Figure 3.19 (left) shows the D_0 - Z_0 significance distributions for the two sets of tracks. A minimum value of 2 is required in track selection for the SV fit, in order to reduce the erroneous usage of prompt tracks. With the aim of reducing even more this kind of contamination, also a requirement on the minimum track p_T is added. In Figure 3.19 (right) the track p_T distribution is reported. The lower limit is chosen to be at 0.8 GeV.

Other requirements, such as the minimum number of hits, the maximum error on impact parameter etc., are also considered in the track selection but their influence is negligible (since cuts are very loose). For completeness the whole set of requirements is reported in Table 3.3.

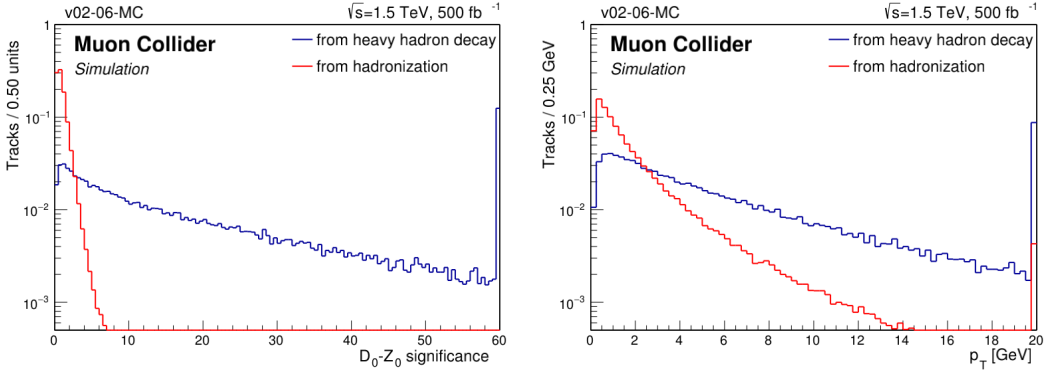


Figure 3.19: D_0 - Z_0 significance (left) and transverse momentum (right) for the two types of tracks selected as described in this paragraph.

PV	Max D_0 Max Z_0 Min n. of hits in VTX	0.1 mm 0.1 mm 4
SV	Max D_0 Max σ_{D_0} Max Z_0 Max σ_{Z_0} Min p_T Min D_0 - Z_0 significance Min n. of hits in VTX	5 mm 1 mm 5 mm 1 mm 0.8 GeV 2 4

Table 3.3: Track selection for PV and SV finding. VTX stands for vertex detector, considering both the barrel and the endcap portion.

3.5.3 Performance of vertex finding

I have evaluated the performance of the *Secondary Vertex Finder* on two samples of 10^4 events of the processes $\mu^+\mu^- \rightarrow H\nu\bar{\nu} \rightarrow b\bar{b}\nu\bar{\nu}$ and $\mu^+\mu^- \rightarrow H\nu\bar{\nu} \rightarrow c\bar{c}\nu\bar{\nu}$ both at $\sqrt{s} = 1.5 \text{ TeV}$, without the BIB overlay. As reference, the results reported by the authors of the LCFIPplus processor [54] are quoted, even though the comparison is not straightforward since the sample used is different ($b\bar{b}$ events at $\sqrt{s} = 91.2 \text{ GeV}$ at ILC [22]).

After the track reconstruction step, subsequently *Primary Vertex Finder* and *Secondary Vertex Finder* are called with the specification of parameters reported in Tables 3.2 and 3.3.

In order to determine performances, tracks are categorized according to their decay chain:

- *Primary*: Tracks whose starting point at generator level is less than $1 \mu\text{m}$ apart from the IP, i.e tracks from primary vertex.
- *Bottom*: Tracks whose most immediate parent with a non-zero lifetime

contains a bottom quark.

- *Charm*: Tracks whose most immediate parent with a non-zero lifetime contains a charm quark.
- *Others*: Tracks not belonging to the b or c hadron decay chain.

In Table 3.4 ($H \rightarrow b\bar{b}$ sample) and 3.5 ($H \rightarrow c\bar{c}$ sample) the total number of tracks per each category is reported together with the fraction of them used to form a secondary vertex. Another figure of merit useful to assess the correctness of the SV reconstruction is the percentage of tracks in SVs coming from the same parent: only SVs fitted with tracks from the same non-zero lifetime parent are considered and only tracks associated with these SVs are counted. This measure accounts for the cross contamination between *Bottom* and *Charm* tracks.

Track Origin	Primary	Bottom	Charm	Others
Number of tracks	116634	34099	40934	2358
Tracks in SVs	$1.02 \pm 0.03\%$	$58.74 \pm 0.27\%$	$63.28 \pm 0.24\%$	$5.13 \pm 0.45\%$
From same parent	-	$27.52 \pm 0.24\%$	$29.80 \pm 0.23\%$	$1.19 \pm 0.22\%$

Table 3.4: The performance of the LCFIPlus vertex finder evaluated on a sample of $H \rightarrow b\bar{b}$ at Muon Collider at $\sqrt{s} = 1.5 \text{ TeV}$

Track Origin	Primary	Bottom	Charm	Others
Number of tracks	150901	166	37942	3108
Tracks in SVs	$1.09 \pm 0.03\%$	$37.35 \pm 3.75\%$	$43.52 \pm 0.25\%$	$4.09 \pm 0.36\%$
From same parent	-	$10.84 \pm 2.41\%$	$38.52 \pm 0.25\%$	$0.90 \pm 0.17\%$

Table 3.5: The performance of the LCFIPlus vertex finder evaluated on a sample of $H \rightarrow c\bar{c}$ at Muon Collider at $\sqrt{s} = 1.5 \text{ TeV}$

In the $H \rightarrow b\bar{b}$ sample, around 60 % of the tracks from b and c hadrons are correctly used to form secondary vertices. Approximately 1 % of *Primary* tracks are erroneously associated to a displaced vertex, while the contamination from *Other* category is around 5 %. Of all the tracks used to fit a SV only about the 45% of them are well separated into bottom and charm vertices.

The performance on the $H \rightarrow c\bar{c}$ sample are similar in terms of contamination from *Primary* and *Other* categories. The efficiency for *Charm* tracks is smaller because charm vertices are less displaced with respect to ones in the $H \rightarrow b\bar{b}$ sample, where c hadrons mostly come from the already displaced vertices of b hadron decay. Furthermore, the cross contamination with *Bottom* tracks is decreased because of the reduced presence of b hadrons in the $H \rightarrow c\bar{c}$ sample: the percentage of tracks in SVs coming from the same parent is almost 90 %.

The overall performance looks compatible with the one reported in the LCFI-Plus paper [54] (Table 3.6), especially for what concerns efficiency and contamination from *Primary*, which was the main goal of the analysis explained

Track origin	Primary	Bottom	Charm	Others
Total number of tracks	496897	258299	247352	56432
Tracks in secondary vertices	0.6%	57.5%	64.3%	2.5%
... from the same parent particle	—	32.2%	38.9%	1.2%

Table 3.6: The performance of the LCFIPplus vertex finder evaluated on a sample of $b\bar{b}$ events at $\sqrt{s} = 91.2 \text{ GeV}$ at ILC

in section 3.5.2. Future efforts should be concentrated on the reduction of contamination from *Others*, which is 2.5 % in Table 3.6, and of the cross contamination between *Bottom* and *Charm* tracks, since the percentage of well separated tracks into the two types of vertices rises up to 60 % in the reference text.

Chapter 4

The c jet identification

I have implemented, for the first time at the Muon Collider experiment, a dedicated tagger for c jet identification. In order to discriminate c jets from b jets and light-flavour jets, the properties of heavy-flavour hadrons resulting from radiation and hadronization of c quarks are exploited.

Several variables are combined into a single powerful discriminator with a Boosted Decision Tree (BDT) (see Appendix B for details).

In this chapter the discriminating variables included in the tagger are presented together with the description of the implemented algorithm, inspired to the CMS [71] one. The performance of this first tagger is evaluated and a comparison with CMS [71] and CLIC [43] is given.

4.1 Heavy-flavour jet discriminating variables

Algorithms for heavy-flavour jet identification exploits variables related to heavy-flavour hadrons clustered in jets. As mentioned in the introduction to section 3.5, the sizeable lifetime of b and c hadrons together with their relativistic boost give rise to displaced tracks (large impact parameter) and secondary vertices. Moreover the semi-leptonic decays of heavy hadrons lead to the presence of non-isolated low-energy electrons and muons (collectively called *soft leptons*) that can be exploited as well (see Figure 4.1).

Thus, the variables used for heavy-flavour tagging can be divided into three categories: track related variables, soft lepton related variables and secondary vertex related variables.

All the plots presented in this section are realized using b, c and light jet samples of different physics processes, summarized in Table 5.1 in the analysis section 5. In order to design and optimize heavy-flavour identification techniques, a method is required for assigning a flavour to jets in simulated events: the true flavour flag is assigned by looking for heavy hadrons inside jets at generator level, as explained in section 3.4.1.

Jets used for these studies and for the analysis are required to satisfy few basic requirements: $\eta < 2.5$, $p_T > 10$ GeV and at least two selected tracks in it.

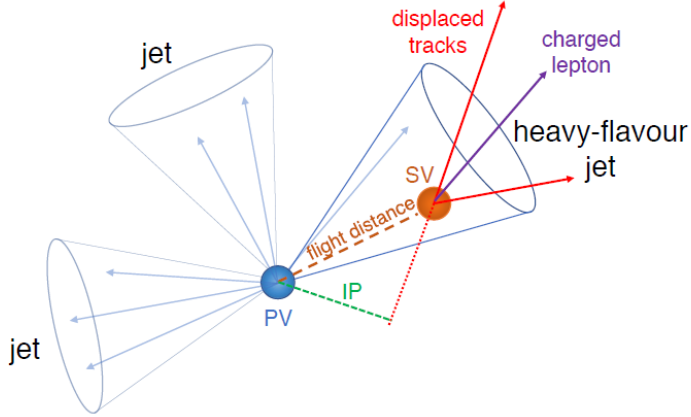


Figure 4.1: Illustration of a heavy-flavour jet with a secondary vertex (SV) from a decay of b/c hadron resulting in displaced tracks (including possibly a soft lepton). The displaced tracks are characterized by a large impact parameter with respect to the primary interaction vertex (PV), while the SV is characterized by a certain sizeable flight distance with respect to PV.

4.1.1 Track selection and variables

The properties of tracks clustered in jets represent the basic inputs of all heavy-flavour jet identification algorithms. In this work, input variables for the tagging algorithms are constructed from the tracks after applying appropriate selection criteria. With the aim of ensuring good quality of the reconstructed tracks, they are required to have p_T higher than 1 GeV, a reduced χ^2 smaller than 5 and more than 4 hits in the vertex detector. Tracks are associated to jets by requiring a ΔR in the pseudorapidity-azimuth space between the track and the jet axis smaller than 1.

The most important track variable is the Signed Impact Parameter (SIP), where the sign convention is different with respect to the one reported in section 3.2.1. Here the sign is given by the sign of the scalar product between the jet momentum and the impact parameter vector (the vector pointing from the PV to the point of closest approach of the track to the PV). In this way the sign is positive if the particle is produced "upstream".

Figure 4.2 illustrates how the sign can discriminate between primary tracks and secondary tracks. In principle, tracks from PV should have a zero impact parameter, but it is not the case because of the detector resolution. Indeed the SIP can be with the same probability slightly greater or smaller than zero, since the resolution effect is symmetric with respect to the PV (left Figure 4.2). As a consequence the yield of positive SIP tracks is the same as the yield of negative SIP tracks. On the opposite, tracks originated from the secondary vertex are more likely to have a positive SIP (right Figure 4.2).

Since the output of the track reconstruction step is the set of parameters described in section 3.2.1, $(\Omega, \phi_0, D_0, Z_0, \tan\lambda)$, a procedure is implemented to calculate the SIP according to the aforementioned sign convention.

Firstly the point of closest approach (p.c.a.) of the track to the PV is computed

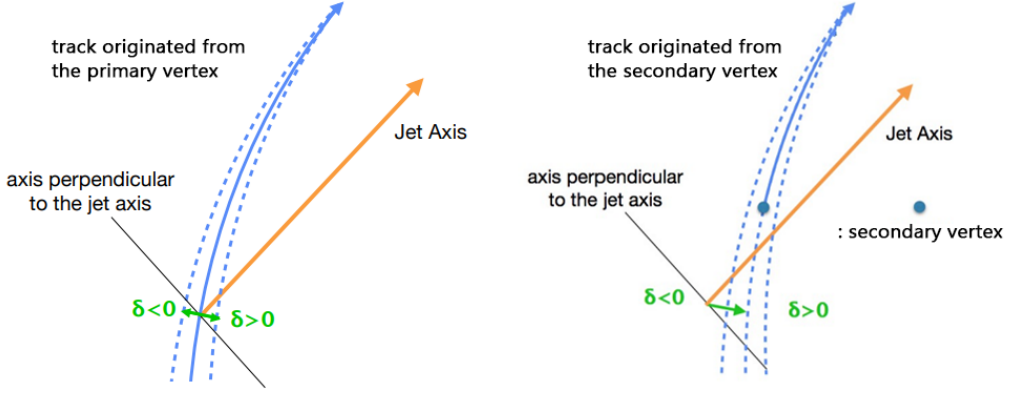


Figure 4.2: Illustration of the difference between primary tracks and tracks from a SV in terms of Signed Impact Parameter.

with the following equations:

$$\begin{aligned} x_{pca} &= -D_0 \sin(\phi_0) \\ y_{pca} &= +D_0 \cos(\phi_0) \\ z_{pca} &= Z_0 \end{aligned} \quad (4.1)$$

The uncertainty on each component is computed with the error propagation formula starting from the uncertainties on the track parameters.

The vector starting from the IP (0,0,0) and pointing to the p.c.a. is evaluated: its magnitude defines the SIP magnitude that can be calculated in 3D, in 2D in the transverse plane, or in 1D in the z direction. The sign of the scalar product between the above mentioned vector and the jet momentum is taken as the SIP sign.

In this analysis, the SIP is divided by its uncertainty, giving the so-called SIP significance. The tracks assigned to a jet are ordered by decreasing 2D SIP significance and only the first two are used in the tagger. From now on, these will be referred to as the *first track* and the *second track*.

Figure 4.3 and 4.4 show the 3D SIP significance of the first and the second track, respectively, for different jet flavours. Tracks in heavy-flavour jets have larger impact parameter significance compared to tracks in light-flavour jets. Nevertheless Figure 4.3 shows that tracks with a large impact parameter significance are also present in light-flavour jets. These originate from the decays of relatively long-lived hadrons, for example K_S^0 or Λ , or from heavy-flavour hadrons where the tracks have been incorrectly clustered into a light-flavour jet. For the second track in light-flavour jets (Figure 4.4), the distribution is much more symmetric as expected for hadrons with a short lifetime.

Finally it can be noticed that also a considerable difference between tracks in c and b jet sample is present, although not so emphasized: the impact parameter is on average higher for tracks in the b sample, compatible with the larger displacement of b hadron decay vertex.

Another track feature that can be exploited is related to the larger mass and harder fragmentation of b and c quarks with respect to light quarks and mass-

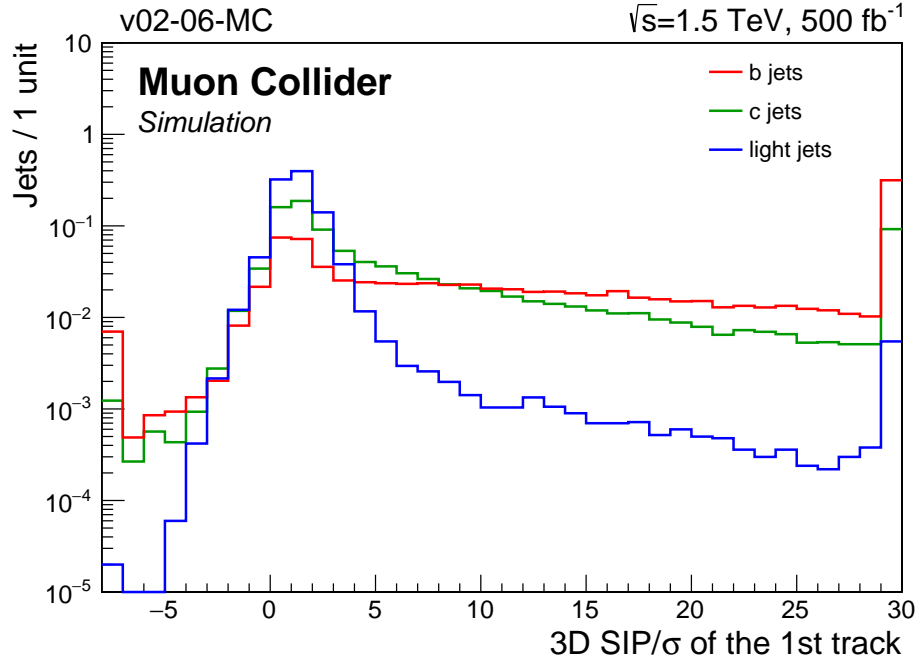


Figure 4.3: Distribution of the 3D SIP significance of the first track, for the three different flavours of jet. Histograms are normalized to unit area. The first and last bin include the underflow and overflow entries, respectively.

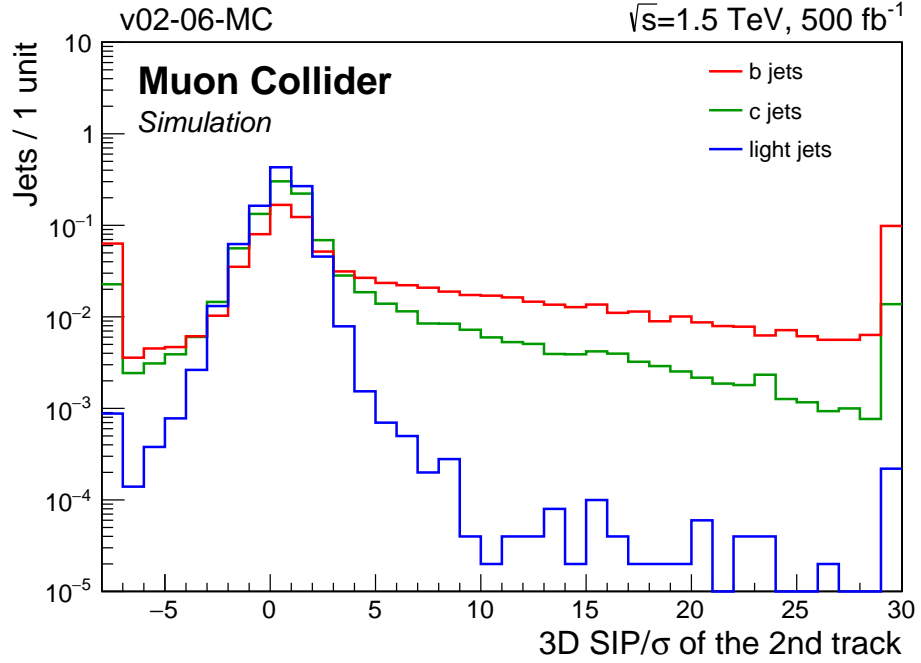


Figure 4.4: Distribution of the 3D SIP significance of the second track, for the three different flavours of jet. Histograms are normalized to unit area. The first and last bin include the underflow and overflow entries, respectively.

less gluons. Because of this property, the decay products of b and c hadrons have, on average, a larger p_T relative to the jet axis than other jet constituents. In Figure 4.5 the distribution of the first track p_T relative to the jet momentum

is reported. A small difference between the b sample and the others is visible, although the variable appears much less discriminating than the SIP-based one.

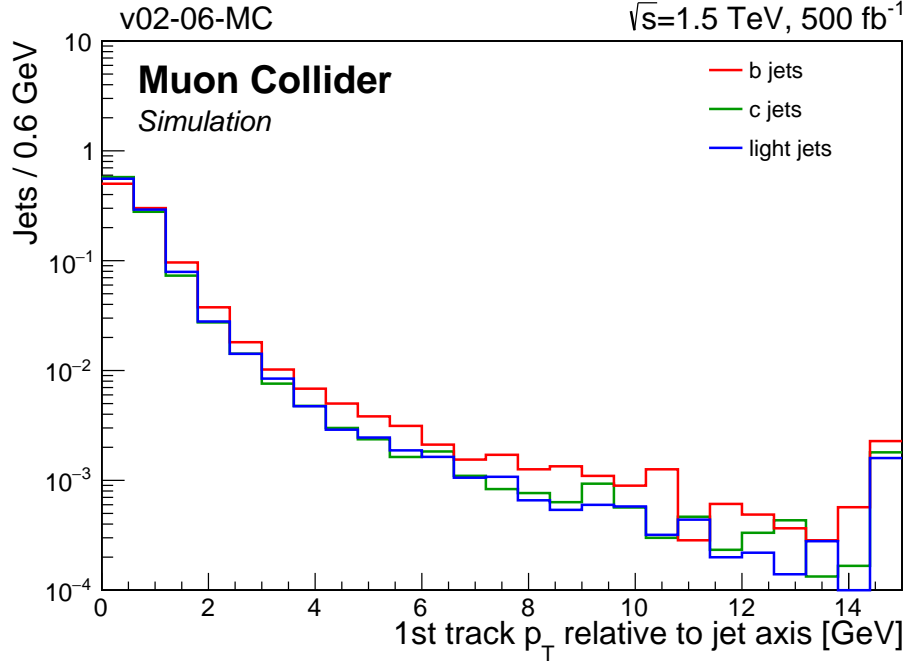


Figure 4.5: Transverse momentum of the first track with respect to the jet axis for different jet flavour samples. Histograms are normalized to unit area. The last bin include the overflow entries.

A variable specific of the c tagging algorithm is the one shown in Figure 4.6: the 2D SIP significance of the first track that raises the combined invariant mass of the tracks above 1.5 GeV [71] (this threshold is related to the c quark mass, as it will be clear in the next paragraph).

This track is selected as follows:

- The four-momenta of the tracks in the jet are summed adding one track at the time, starting from the first one.
- Every time a track is added, the total four-momentum vector is computed together with its invariant mass.
- When the computed invariant mass exceeds the 1.5 GeV threshold, the track responsible for overcoming such a limit is taken, and its 2D SIP significance is chosen as a discriminating input variable.

4.1.2 Secondary vertex selection and variables

Secondary vertex reconstruction is described in section 3.5, where the inclusive vertex finder algorithm of LCFIPlus processor is presented. Powerful discriminating variables can be derived from the reconstructed secondary vertices, particularly useful to distinguish between b and c jets.

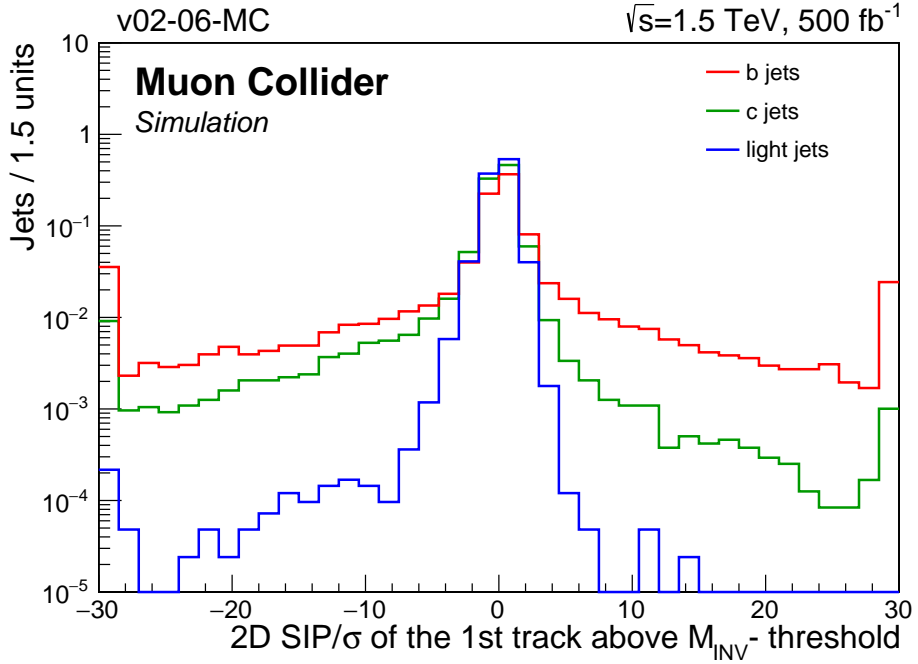


Figure 4.6: 2D SIP significance of the first track above the invariant mass threshold, for different jet flavour samples. Histograms are normalized to unit area. The first and last bin include the underflow and overflow entries, respectively.

Reconstructed vertices are required to have a 2D flight distance significance (i.e. distance from PV in the transverse plane divided by its uncertainty) greater than 1.5. Secondary vertices are associated with jet by requiring the ΔR between the jet axis and the SV flight direction (vector from PV to SV) to be less than 1. SVs matched with a jet are ordered by increasing uncertainty on their 3D flight distance. Only the first vertex variables are included in the tagger.

An example of SV related variable is the so called *SV corrected mass* [71], defined as $\sqrt{M_{SV}^2 + p^2 \sin^2 \theta} + p \sin \theta$, where M_{SV} is the invariant mass of the tracks associated with the secondary vertex, p is the secondary vertex momentum obtained from the tracks associated with it, and θ the angle between the secondary vertex momentum and the secondary vertex flight direction. Using this formula, the secondary vertex mass is corrected for the observed difference between its flight direction and its momentum, taking into account particles that were not reconstructed or which failed to be associated with the secondary vertex.

Figure 4.7 shows the corrected mass distribution for the different jet flavours. The SV mass of c jet sample has a well-defined peak around 1.5 GeV, compatible with the average c hadron mass of 2 GeV. The b peak, instead, is much broader since b jets apart from b hadrons (average mass around 5 GeV) tend to contain also c hadrons coming from b decay. SVs in the light-flavour sample are very rare (approximately 1% of light jets contain a reconstructed SV) and are mainly fake SV reconstructed with primary tracks, if we consider that the V^0 rejection discussed in 3.5 removes the great majority of K_S^0 and Λ decays.

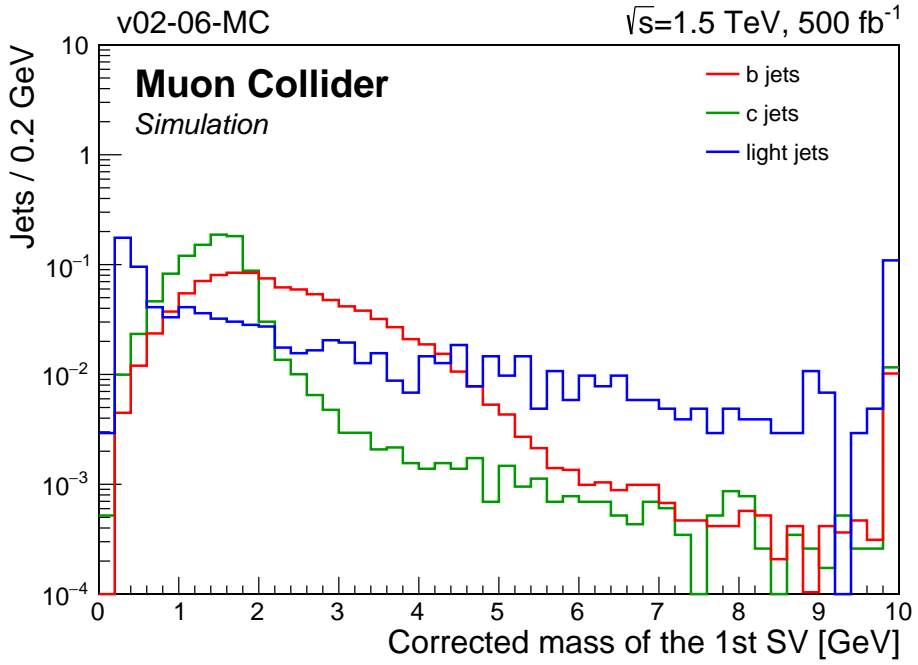


Figure 4.7: Corrected mass of the first SV. Histograms are normalized to unit area. The last bin includes the overflow entries.

Another SV discriminating variable is the flight distance, which is directly related to the lifetime of heavy hadrons. Figure 4.8 shows the 3D flight distance significance of the first vertex. On average, the flight distance is higher for the b jet sample, as expected, while the light distribution is strongly peaked at very small values, dealing with fake SVs fitted with primary tracks.

More complex variables are the so called *SV boost* and *SV mass-energy fraction*, reported in Figures 4.9 and 4.10, respectively.

The SV boost is defined as $\Upsilon^2/(\Upsilon^2 + 10)$ [71] where Υ is:

$$\Upsilon = \frac{\sqrt{5.2794}}{m_{SV} [\text{GeV}]} \frac{\sum_{SV\text{tracks}} p_{T_i}}{\sqrt{p_{T_{jet}}}} \quad (4.2)$$

Here 5.2794 is the average b meson mass in GeV, m_{SV} is the corrected mass, the summation concerns the transverse momenta of the tracks used to fit the SV, and $p_{T_{jet}}$ is the transverse momentum of the jet.

The mass-energy fraction is defined as $X/(X + 0.04)$ [71], where X is :

$$X = \frac{m_{SV} [\text{GeV}]}{5.2794} \frac{\sum_{SV\text{tracks}} E_i}{\sum_{jet\text{ tracks}} E_i} \quad (4.3)$$

with the sum of the energies at the numerator running over tracks related to SV and at the denominator running over all tracks clustered in the jet.

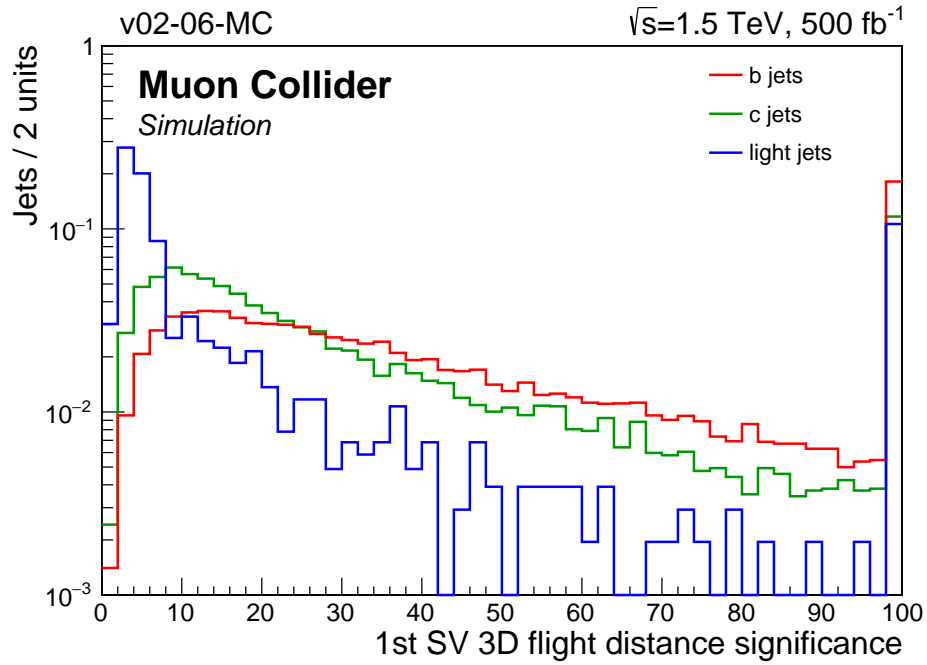


Figure 4.8: 3D flight distance significance of the first SV. Histograms are normalized to unit area. The last bin includes the overflow entries.

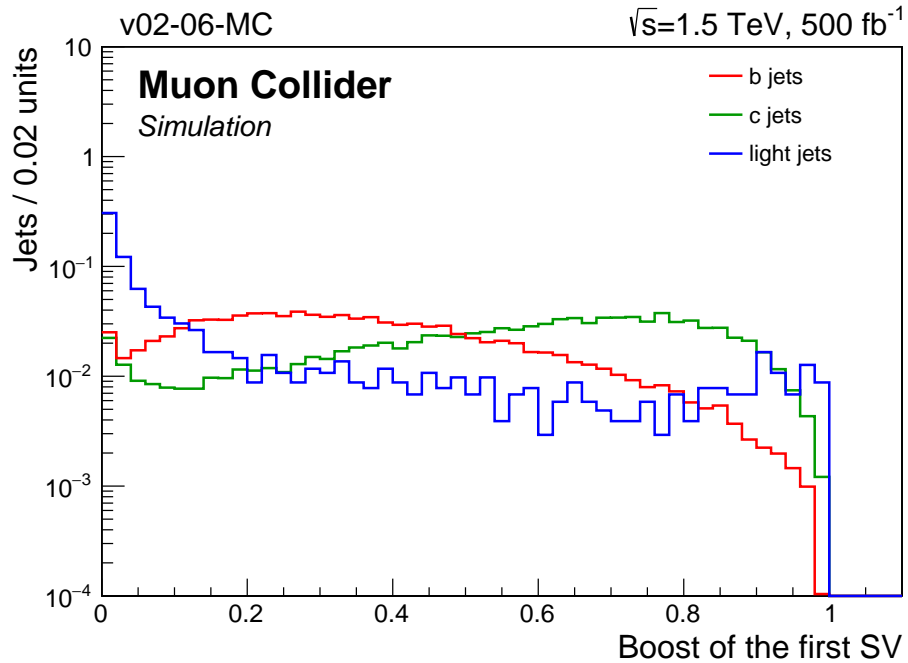


Figure 4.9: Boost of the first SV. Histograms are normalized to unit area.

4.1.3 Soft lepton selection and variables

Leptons are present only in the 20% (10 %) of b (c) hadron decay. Nonetheless the properties of these low-energy non-isolated muons and electrons can help discriminating heavy-flavour from light flavour jets.

The selections applied for leptons are the same as the ones applied to tracks,

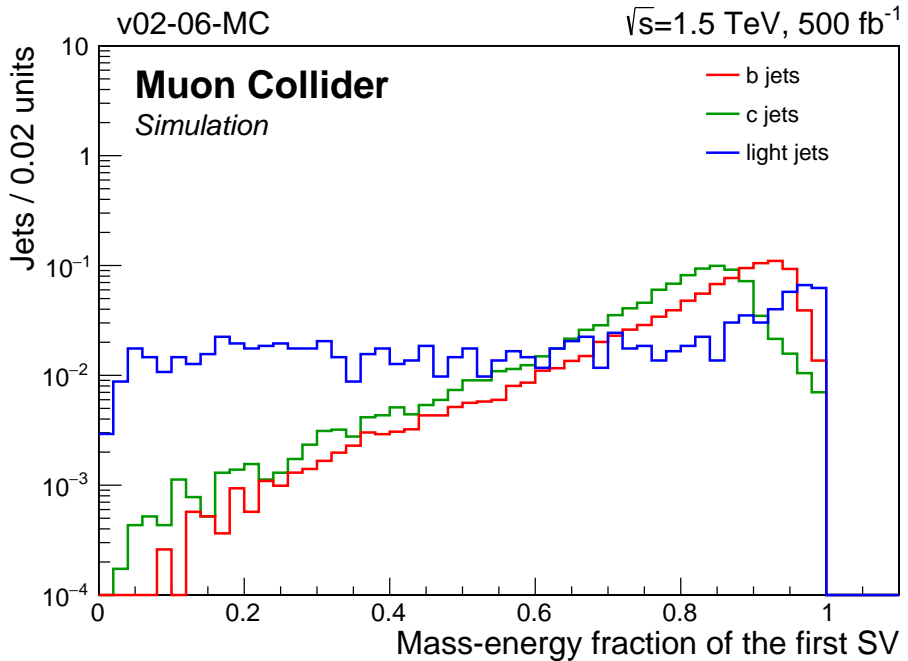


Figure 4.10: Mass-energy fraction of the first SV. Histograms are normalized to unit area.

except for the minimum transverse momentum which in this case is 2 GeV. The requirement is slightly raised up to avoid considering leptons from photon conversion or π decay. Leptons are ordered following the same criterion used for tracks and only the first lepton variables are exploited in the tagger.

Soft lepton related variables are similar to the variables based on track information. Two examples are reported in Figures 4.11 and 4.12: the former represents the ratio between the p_T of the first lepton and the p_T of the jet, while the latter is the p_T of the first lepton with respect to the jet axis.

Table 4.1 summarizes the basic selections applied on tracks, leptons, secondary vertices and jets.

4.2 Tagger algorithm description

The distributions of the tagging variables for c jets lie in between the distributions for b and light-flavour jets, as seen section 4.1. This is due to the lifetime of c hadrons being shorter than the b hadron one, to the lower secondary vertex multiplicity and also to the smaller c quark mass results in a smaller track p_T relative to the jet axis. Therefore, it is particularly challenging to efficiently identify jets originating from c quarks.

Several variables, including the ones shown in section 4.1, are combined in the c tagging algorithm, since no single variable is by itself sufficient to achieve a good discrimination.

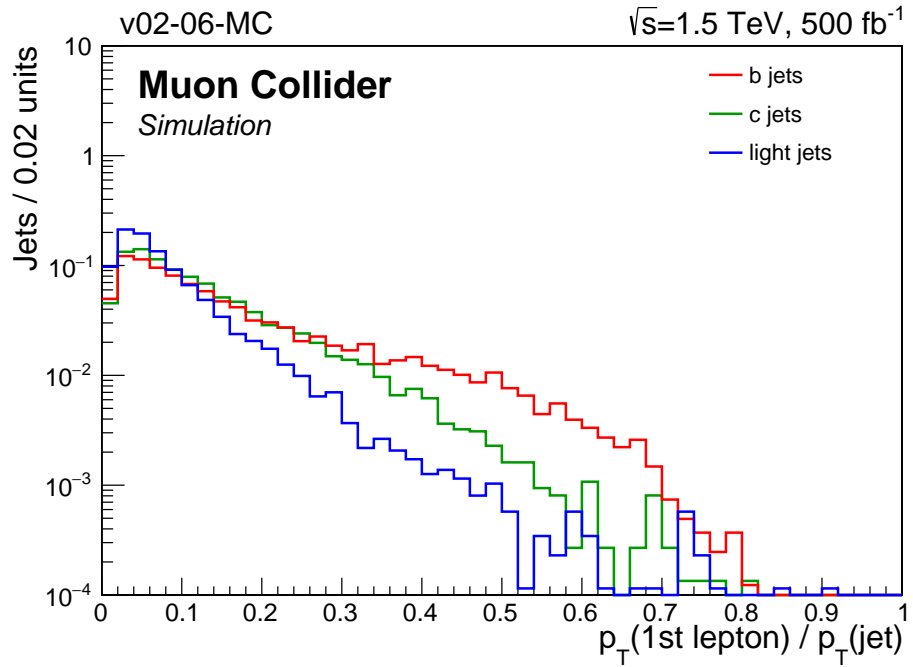


Figure 4.11: p_T of the first lepton divided by jet p_T . Histograms are normalized to unit area. The last bin includes the overflow entries.

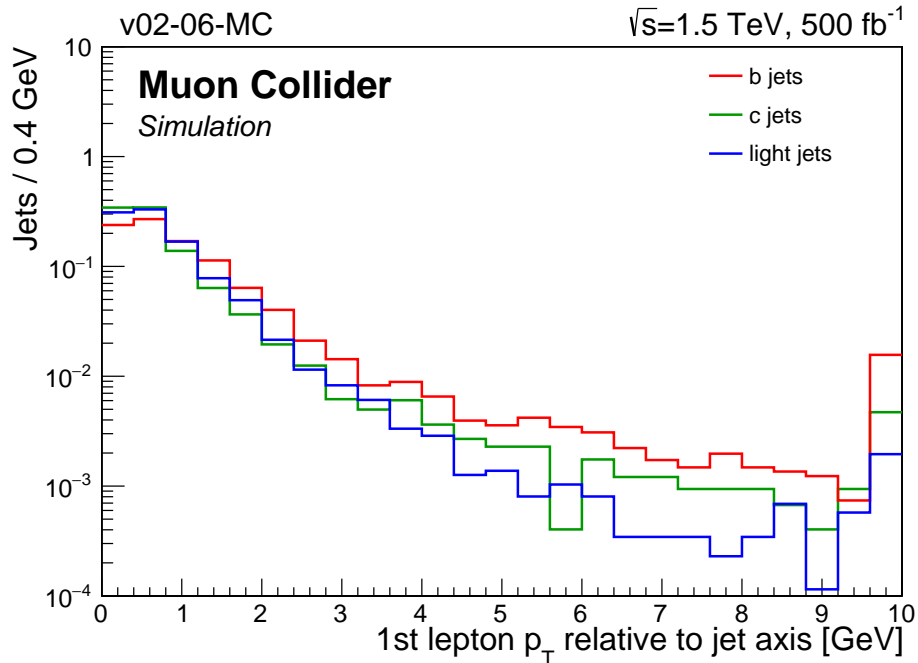


Figure 4.12: p_T of the first lepton with respect to the jet axis. Histograms are normalized to unit area. The last bin includes the overflow entries.

The presence or absence of a secondary vertex in jets leads to the definition of two independent vertex categories :

- **RecoVertex**: including jets that contain one or more secondary vertices.
- **NoVertex** : including jets in which no secondary vertex is found.

Tracks	$p_T > 1 \text{ GeV}$ $\chi^2/ndf < 5$ More than 4 hits in VTX
Leptons	$p_T > 2 \text{ GeV}$ $\chi^2/ndf < 5$ More than 4 hits in VTX
Vertices	2D flight distance significance > 1.5
Jets	$\eta < 2.5$ $p_T > 10 \text{ GeV}$ Min. 2 selected tracks

Table 4.1: Basic quality requirements for reconstructed objects. VTX stands for vertex detector, considering both the barrel and the endcap portion.

Figure 4.13 shows the percentage of jets in the two categories: in almost 80% of b jets there is at least a reconstructed SV; this fraction decreases down to 40% for c jets and about to 1% for light-flavour jets, as expected.

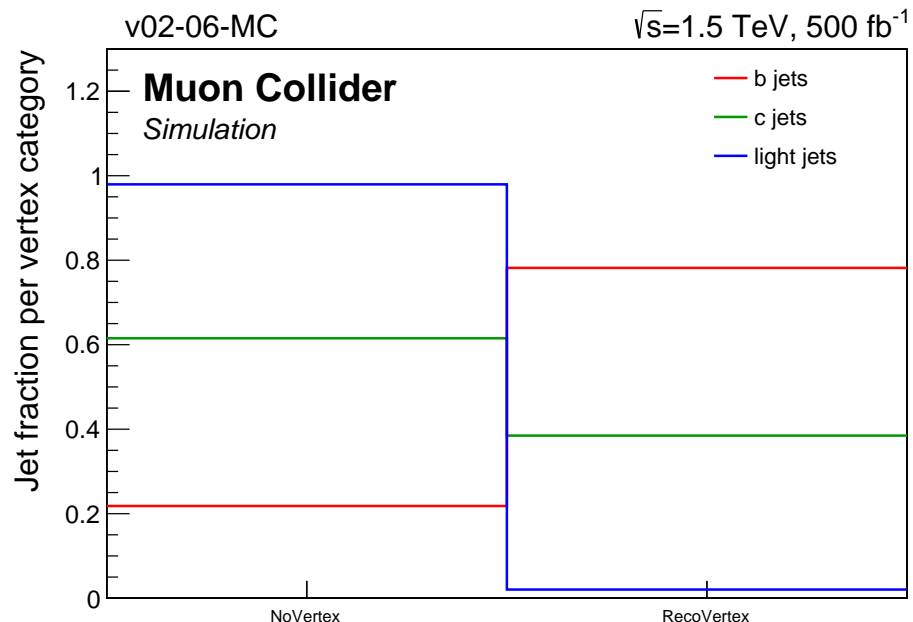


Figure 4.13: Jet fraction per vertex category.

Moreover, three independent lepton categories are defined according to the presence or absence of leptons in jets:

- **NoSoftLepton**: including jets without soft leptons.
- **SoftMuon**: including jets with at least one soft muon.
- **SoftElectron**: including jets with no soft muon, but at least one soft electron.

Figure 4.14 shows the percentage of jets in each lepton category: in about 30% of b jets there is at least a lepton, while for c jet the fraction is 25% and for light ones is 15%. All the three samples show a higher fraction of SoftLepton than expected (if only heavy hadron decay is considered as a source). The cause is probably the contamination from other sources of leptons, as the photon conversion, which affects mostly the SoftElectron category.

Also wrong identification or imprecision in jet clustering can be a reason.

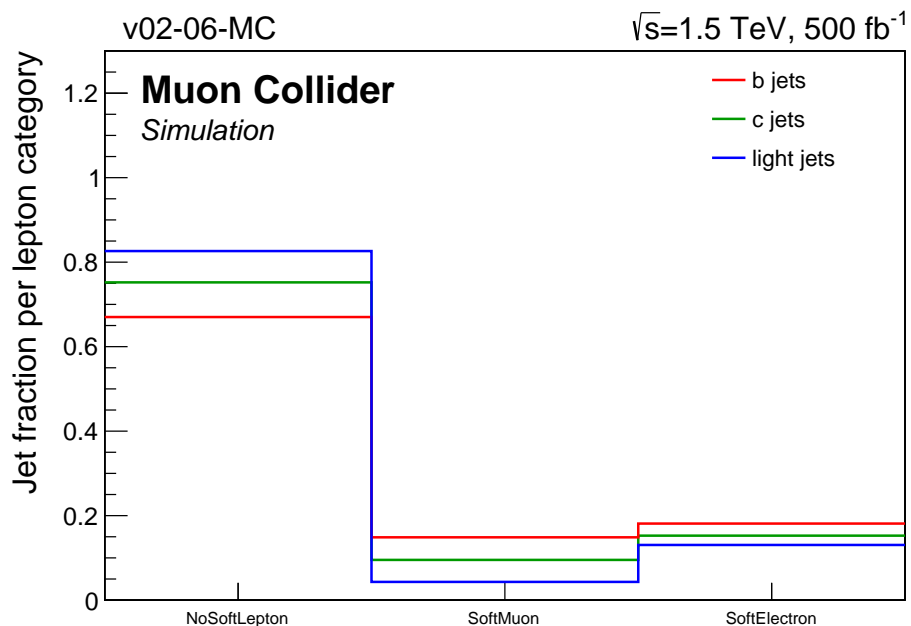


Figure 4.14: Jet fraction per lepton category.

Some tagging variables are only defined if a secondary vertex is reconstructed or if a soft lepton is found inside the jet. Whenever a variable is not available, a default value is assigned to it, taken as -999.

The full list of input features is the following (plots not shown in section 4.1 can be found in Appendix A) :

- The 2D (Figure A.5) and 3D (Figures 4.3 and 4.4) SIP significance of the first two tracks.
- The 2D (Figure 4.6) and 3D (Figure A.6 left) SIP significance of the first track that raises the combined invariant mass of the tracks above 1.5 GeV.

- The ΔR between the first track and the jet axis (Figure A.3 right).
- The track momentum parallel to the jet direction, for the first track (Figure A.7 left).
- The track momentum parallel to the jet direction divided by the magnitude of the track momentum vector, for the first track (Figure A.7 right).
- The track p_T relative to the jet axis, i.e. the track momentum perpendicular to the jet axis, for the first track (Figure 4.5) .
- The track p_T relative to the jet axis divided by the magnitude of the track momentum vector, for the first track (Figure A.8 left).
- The transverse energy of the total summed four-momentum vector of the selected tracks divided by the transverse energy of the jet (Figure A.6 right).
- The ΔR between the total summed four-momentum vector of the tracks and the jet axis (Figure A.4 left).
- The number of tracks associated with the jet (Figure A.4 right).
- The vertex category (Figure 4.13).
- For jets in the RecoVertex category:
 - The number of secondary vertices (Figure A.1 left).
 - The number of tracks associated with the first SV (Figure A.1 right).
 - The 2D (Figure A.2 left) and 3D (Figure 4.8) flight distance significance of the first SV.
 - The corrected SV mass of the first SV (Figure 4.7).
 - The mass-energy fraction of the first SV (Figure 4.10).
 - The boost of the first SV (Figure 4.9).
 - The energy ratio of the first SV, defined as its energy (sum of SV-tracks energies) divided by the energy of the total summed four-momentum vector of the selected tracks (Figure A.2 right).
 - The ΔR between the first SV and the jet axis (Figure A.3 left).
- The lepton category (Figure 4.14).
- For jets in the SoftMuon or SoftElectron category:
 - The ratio between the first lepton p_T and the jet p_T (Figure 4.11).
 - The first lepton p_T relative to the jet axis (Figure 4.12).
 - The first lepton momentum parallel to the jet direction divided by the magnitude of the jet momentum (Figure A.8 right).

The Multivariate Analysis algorithm chosen to combine the aforementioned variables is the BDT. The training and testing of the algorithm is performed through the TMVA-toolkit of ROOT [74], on a mixture of jet samples at $\sqrt{s} = 1.5 \text{ TeV}$ described in Table 5.1, without the BIB overlay. The samples are split in two halves to perform training and test on two independent sets of data.

I have trained and tested two binary classifiers:

- One for discriminating c jets from b jets (*CvsB tagger*), that uses all the variables listed above.
- One for discriminating c jets from light flavour jets (*CvsL tagger*), that uses all the track and lepton variables plus the vertex category information, because of lack of secondary vertices in the samples.

The BDT parameters used for both classifiers are shown in Table 4.2, together with the number of signal and background events for the training procedure.

Max. depth	3	CvsB	
Min. node size	2.5%		
Separation type	Gini Index		
N. of cuts	50	N. of signal events	30014
N. of trees	800	N. of background events	24582
Boost type	AdaBoost	CvsL	
AdaBoost β	0.5	N. of signal events	30014
Use bagged boost	true	N. of background events	50116
Bagged sample fraction	50%		

Table 4.2: BDT parameters and number of signal and background events for the training procedure of CvsB and CvsL. An explanation of the parameters can be found in Appendix B.

The BDT scores for CvsB and CvsL tagger are shown in Figure 4.15, with the overlay of the training and test distributions for an overtraining check (see details in Appendix B).

For the CvsB discriminator (left), the signal (i.e. c jets) are peaked in the higher score region while the b jet background has an almost flat distribution across all the BDT output range.

For the CvsL discriminator (right), instead, the background (i.e. light-flavour jets) is peaked in the lower score region, while the c jet distribution has a structure with two not-well-resolved peaks, one in the background region and one in the signal region, and an almost flat behaviour in the middle.

A K-S test is performed on the background and signal distributions separately, in order to assess the compatibility of the training and test curves. The p-values returned by the test are reported in Table 4.3. The probabilities are around 10-15 % for the CvsB discriminator, while for the CvsL one there is a significant difference between signal and background p-values caused by the bigger statistics available in the light sample. The increase in number of signal events might lead to a better agreement in the future. For both discriminators the overfitting can be excluded (see section B.3 in the Appendix B).

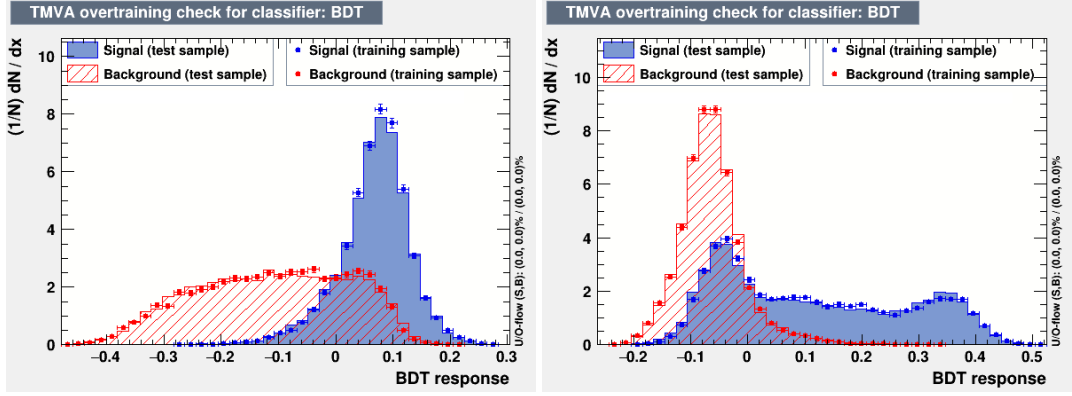


Figure 4.15: BDT score for CvsB (left) and CvsL (right) discriminators. Training and test distributions are overlaid to look for eventual overtraining issues.

CvsB	
Signal p-value	0.11
Background p-value	0.15
CvsL	
Signal p-value	0.05
Background p-value	0.34

Table 4.3: P-values returned by the K-S test are reported for Signal and Background distributions independently, for both CvsB and CvsL tagger.

4.3 Flavour tagging performance

I have evaluated the performance of the c tagging algorithm using the same physics processes employed for the training and testing processes.

Figure 4.16 shows the CvsB and CvsL discriminator outputs when the trained classifiers are applied on the three different jet samples.

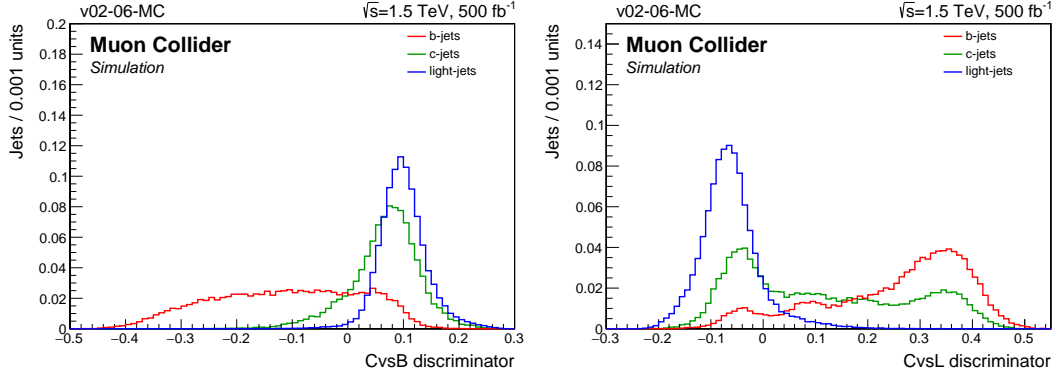


Figure 4.16: Distribution of the CvsB (left) and CvsL (right) discriminator scores for jets of different flavours in simulated events described in Table 5.1. Histograms are normalized to unit area.

Looking at the CvsB discriminator distribution, it can be noticed that when the algorithm is trained to learn the differences between c jets and b jets, once

it is applied on the light sample, it recognises the jets as c-like. Moreover the light jet histogram is even more peaked in the signal region with respect to the c jet one.

Similarly, the CvsL classifier recognizes b jets as c-like. In this case, it can be also noticed that in the b jet sample there is no peak in the background region, differently from the c jet sample.

These discriminator output features are a natural consequence of the characteristics of the c jet input variables, since they lie in between the b jet and the light jet ones. In Figure 4.17 the efficiencies as a function of the applied BDT cut are also reported, being useful to choose the tagger working point.

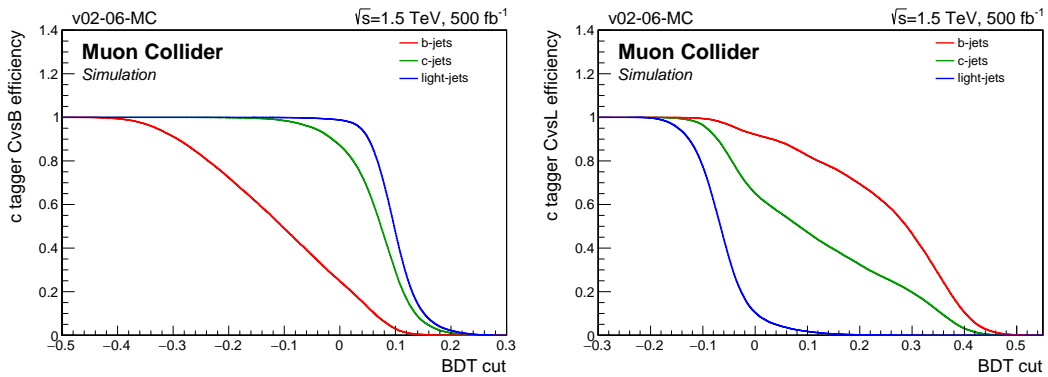


Figure 4.17: Efficiency for b, c and light jets versus discriminator cut, for CvsB and CvsL.

The individual performances of the taggers are evaluated through the ROC curves in Figure 4.18.

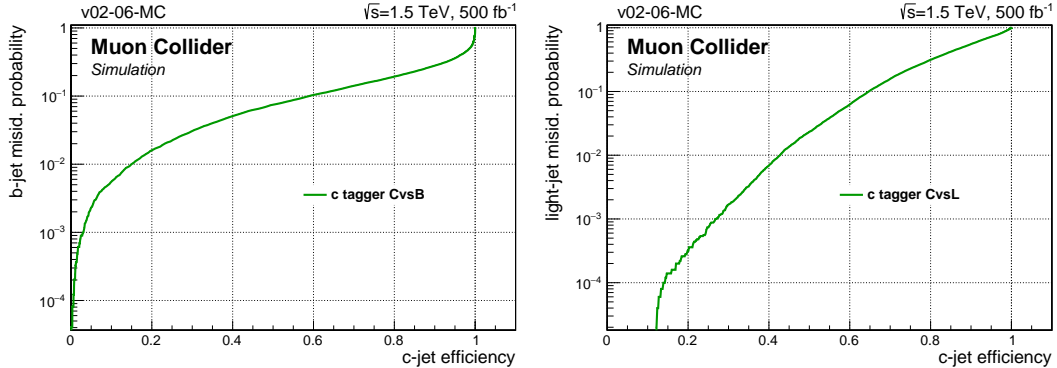


Figure 4.18: Misidentification probability for b jets (left) and light-flavour jets (right) versus c jet identification efficiency.

A comparison with CMS and CLIC c tagger performances is reported in Table 4.4. CMS is taken as a reference because the implemented algorithm is inspired by the CMS analysis [71], while CLIC is an example of future lepton collider with a very clean environment. CMS results have been evaluated on a sample of $t\bar{t}$ events at 13 TeV, while the CLIC ones [43] on a sample of di-jet events at 500 GeV without overlay of the $\gamma\gamma \rightarrow \text{hadrons}$ background.

These first results for the Muon Collider outperform the CMS one while are compatible with the performance reported by CLIC without BIB overlay.

c-tag eff.	b misid. probability			light misid. probability		
	MuColl (w/o BIB)	CMS	CLIC (w/o overlay)	MuColl (w/o BIB)	CMS	CLIC (w/o overlay)
	50%	7.5%	11%	7%	2.3%	14 %
60%	10%	14%	11%	6.3%	25 %	6 %
70%	14%	20%	15%	16%	40 %	12 %
80%	19%	26%	23%	31%	55 %	25 %
90%	28%	40%	32%	55%	75 %	52 %

Table 4.4: Beauty and light-flavour contamination for fixed values of c tagging efficiencies at Muon Collider (w/o BIB), CMS and CLIC (w/o overlay).

Since the two discriminators are applied together in the analysis, it is helpful to evaluate their combined action on the samples and calculate the total tagging efficiency and mis-tagging probability.

This is the purpose of the plot in Figure 4.19, which shows the light misidentification probability versus the b one for fixed values of c tagging efficiency.

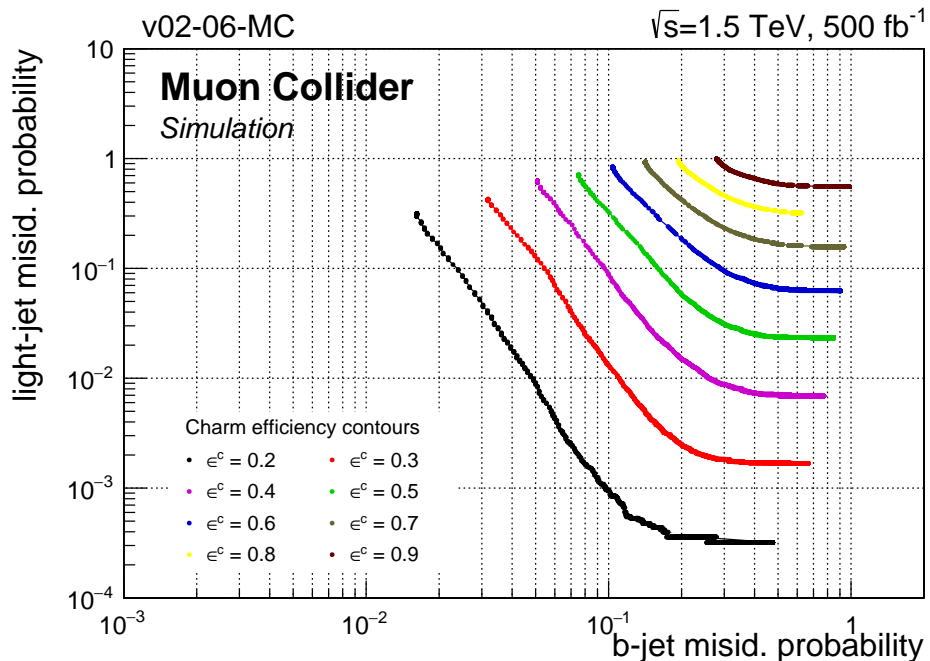


Figure 4.19: Misidentification probability for light-flavour jets versus misidentification probability for b jets for several constant c jet efficiencies.

In the next chapter the tagger here described in full detail is applied in the $H \rightarrow c\bar{c}$ analysis, choosing an appropriate working point. The developed c jet identification technique will allow the first evaluation of the precision achievable at Muon Collider on the Hcc coupling.

Chapter 5

Analysis of $H \rightarrow c\bar{c}$

In this chapter the analysis of $H \rightarrow c\bar{c}$ at $\sqrt{s} = 1.5$ TeV without the Beam Induced Background overlay is outlined. The full reconstruction with the full BIB is not yet available due to some limitations in the computing resources related to the tracking algorithm with BIB. This problem is expected to be solved in the near future, and one of the development of this work would be the implementation of the BIB in the c-tagging and in the analysis. Here I present a first estimate of the precision achievable on the Higgs coupling to c quark (g_{Hcc}) at Muon Collider.

In principle with the application of a mitigation strategy, as mentioned in section 2.3, the BIB overlay should lead to only a little degradation of the measurement. If this assumption is correct, this work demonstrates that the performance at Muon Collider are competitive with that of other Future Colliders (as CLIC [32]). Moreover the precision is expected to increase, and the BIB to decrease, with increasing center of mass energy. A projection of this result at $\sqrt{s} = 3$ TeV is presented at the end of the chapter.

5.1 Signal and background event generation

The signal under study is the Higgs decay into charm quarks, where the Higgs Boson is produced through *WW fusion*, that is the dominant process for Higgs production at this energy (see section 1.5).

The considered background consists of processes that have at least two jets in the final state. For what concerns the peaking background in the Higgs region, the decays $H \rightarrow b\bar{b}$ and $H \rightarrow gg$ are considered as their branching ratios are respectively 20 and 3 times higher than the signal one.

The non-peaking background is represented by processes with two jets and two leptons (of any kind) in the final states. The exclusive final state with only two jets (i.e. no leptons) is neglected since firstly it can only occur through an s-channel process which is characterized by a small cross section at this energy and, secondly, the di-jet invariant mass does not fall into the Higgs mass region.

All the samples produced for this work are summarized in Table 5.1, where they are divided on the basis of the final state jet flavour. When the process is

specified, Pythia8 [75] is used as generator, while when the process is generic but the final state fixed, MadGraph5 (MG5) [76] is employed.

MadGraph5 calculates all the Feynman diagrams relevant for the specified final states and produces events according to them and their cross section. In order to increase events in the interesting region and reduce the required computational time, several selections are applied at this level.

A summary of the selections applied at generator level is given below:

- Jet pseudorapidity less than 3, in order to simulate only jets in the acceptance of the detector.
- Jet transverse momentum greater than 10 GeV, as the same cut is applied in the analysis.
- Jet separation greater than $\Delta R = 0.5$, otherwise the jets are likely to be clustered in a single object.
- Jet invariant mass in the range 100 – 300 GeV.
- Eventual charged leptons in the final state are required to be out of the detector acceptance, since if they can be detected, a simple lepton veto can be implemented to discard the events.

The first sample of light jets produced with MadGraph (see Table 5.1) has actually only an upper limit on the di-jet invariant mass at 300 GeV, but it was later considered not enough to produce the required number of events in the relevant region. Nonetheless the sample was kept and included in the analysis for completeness.

5.2 Event selection

In Figure 5.1 the number of jets per event, the jet pseudorapidity, transverse momentum and energy, the di-jet invariant mass and separation are shown for the $H \rightarrow b\bar{b}$, $H \rightarrow c\bar{c}$ and $H \rightarrow gg$ processes. In order to build the Higgs candidates, only events with at least two jets are considered and if more than two jets exist the two with the highest p_T are chosen. The histograms are filled with the kinematic variables of the jets used to form the Higgs candidates.

The invariant mass of the selected jet pairs is peaked around the Higgs Boson mass for all the samples, as expected. The pseudorapidity, the energy and the transverse momentum distributions of the three samples are the same. Only the jet pair ΔR is slightly different for the $H \rightarrow gg$ sample, peaking towards lower values of separation. Considering these distributions, it's clear that the three processes are kinematically indistinguishable and, as a consequence, it is crucial to deploy a powerful c tagging algorithm.

	Physics process	$\sigma(\text{fb})$	N.(k)	Cuts	Gen.
c jet samples	$\mu^+ \mu^- \rightarrow H \nu \bar{\nu}$ $\rightarrow c\bar{c} \nu \bar{\nu}$	8.9	10	-	Pythia
	$\mu^+ \mu^- \rightarrow c\bar{c} 2\text{lep}$	399	9.993	$m_{jj} \in [100, 300] \text{ GeV}$, $p_{T_j} > 10 \text{ GeV}, \eta_j < 3$, $\Delta R_{jj} > 0.5, \eta_{\text{lep}} > 2.4$	MG
b jet samples	$\mu^+ \mu^- \rightarrow H \nu \bar{\nu}$ $\rightarrow b\bar{b} \nu \bar{\nu}$	180	10	-	Pythia
	$\mu^+ \mu^- \rightarrow b\bar{b} 2\text{lep}$	508	9.784	$m_{jj} \in [100, 300] \text{ GeV}$, $p_{T_j} > 10 \text{ GeV}, \eta_j < 3$, $\Delta R_{jj} > 0.5, \eta_{\text{lep}} > 2.4$	MG
light jet samples	$\mu^+ \mu^- \rightarrow H \nu \bar{\nu}$ $\rightarrow gg \nu \bar{\nu}$	26.4	10	-	Pythia
	$\mu^+ \mu^- \rightarrow 2\text{light}$ $2\text{lep} (*)$	$2.2 \cdot 10^8$	10	$m_{jj} < 300 \text{ GeV}$, $p_{T_j} > 10 \text{ GeV}, \eta_j < 3$, $\Delta R_{jj} > 0.5, \eta_{\text{lep}} > 2.4$	MG
	$\mu^+ \mu^- \rightarrow 2\text{light}$ 2lep	$2.8 \cdot 10^6$	10	$m_{jj} \in [100, 300] \text{ GeV}$, $p_{T_j} > 10 \text{ GeV}, \eta_j < 3$, $\Delta R_{jj} > 0.5, \eta_{\text{lep}} > 2.4$	MG

Table 5.1: Table summarizing the sample produced for the analysis. It reports the simulated physics processes, the estimated cross sections, the number of simulated events, the cuts imposed at generator level and the generator used. All samples are produced at $\sqrt{s} = 1.5 \text{ TeV}$.

The first step in this analysis consist of applying the basic requirements reported in Table 4.1. Afterwards the two trained classifiers CvsB and CvsL are applied in order to reject b jets and light-flavour jets. The working point chosen for the analysis (*CvsB cut, CvsL cut*) = (0, 0.04) is shown in the scatter plot of Figure 5.2. The working point identifies in the CvsL-CvsB space four regions, of which the upper left one is predominantly populated of light jets, the upper right one of c jets and the bottom right one of b jets. In order to identify c jets, the upper right region is selected, i.e. CvsL and CvsB scores are required to be greater then the working point values.

As a check of the stability of the tagging efficiency at the chosen working point, a study of the performance as a function of the jet transverse momentum is carried out, considering the two discriminators individually. In Figure 5.3 the c tagging efficiency (left, measured in a c-jet-enriched sample) and mis-tagging probability (right, measured in a b-jet-enriched sample) for the CvsB discriminator are reported as a function of p_T .

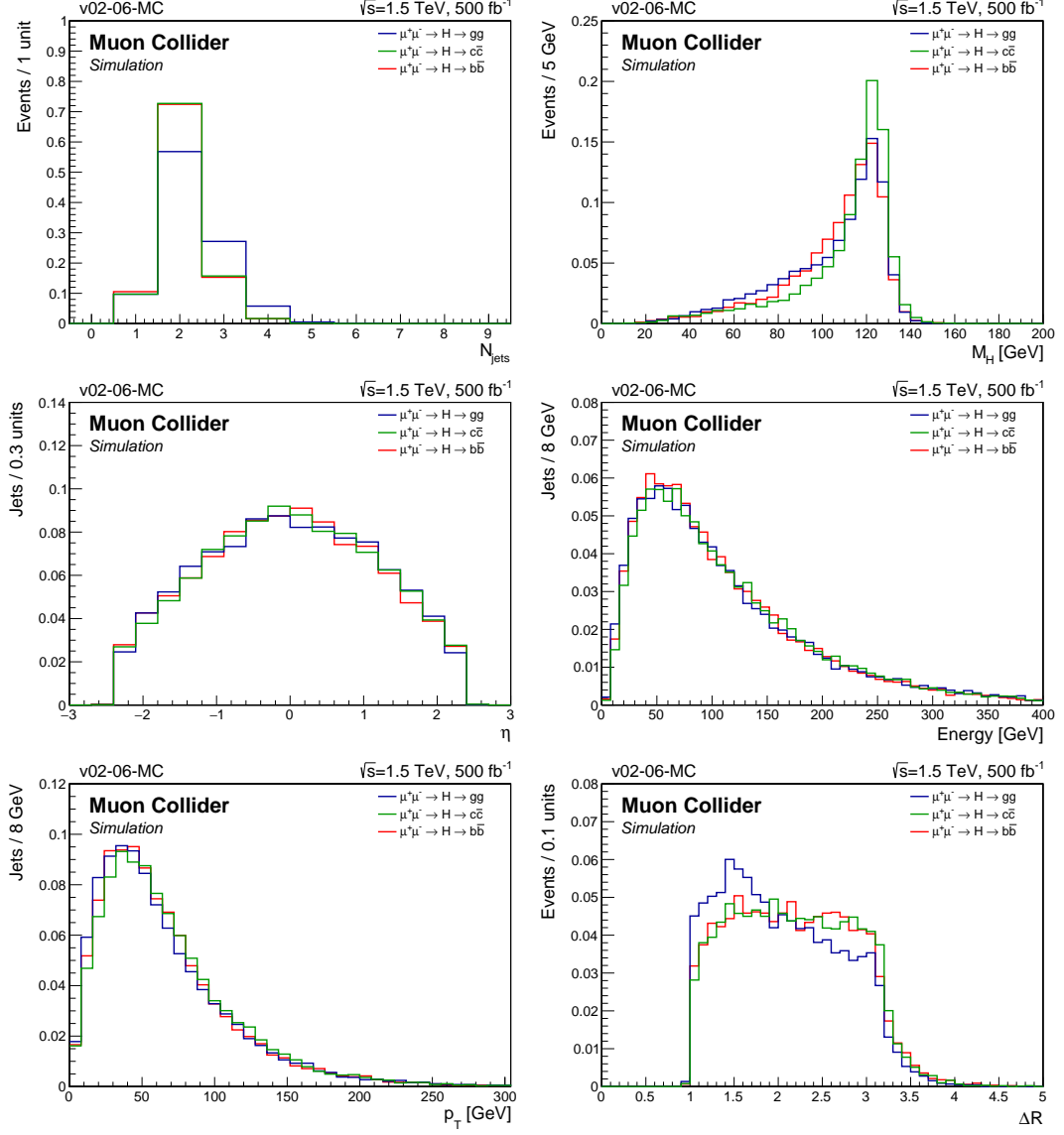


Figure 5.1: Number of jet per event, invariant mass of the Higgs candidate, jet pseudorapidity, jet energy, jet transverse momentum and di-jet separation, for the samples $H \rightarrow b\bar{b}$, $H \rightarrow c\bar{c}$ and $H \rightarrow gg$. For the kinematic variable plots only the jets used to form the Higgs candidate are included. No further selections are applied. Distributions are normalized to unit area.

As can be seen, the tagging efficiency is approximately stable with p_T , while the b misidentification probability decreases visibly. The CvsB tagger efficiency and contamination integrated over the p_T distributions are respectively 87 % and 25 %. In Figure 5.4 the c tagging efficiency (left, measured in a c -jet-enriched sample) and mis-tagging probability (right, measured in a light-jet-enriched sample) for the CvsL discriminator are reported as a function of p_T . The tagging efficiency increases with increasing p_T as well as the light misidentification probability. The CvsL tagger efficiency and contamination integrated over the p_T distributions are respectively 57 % and 5 %.

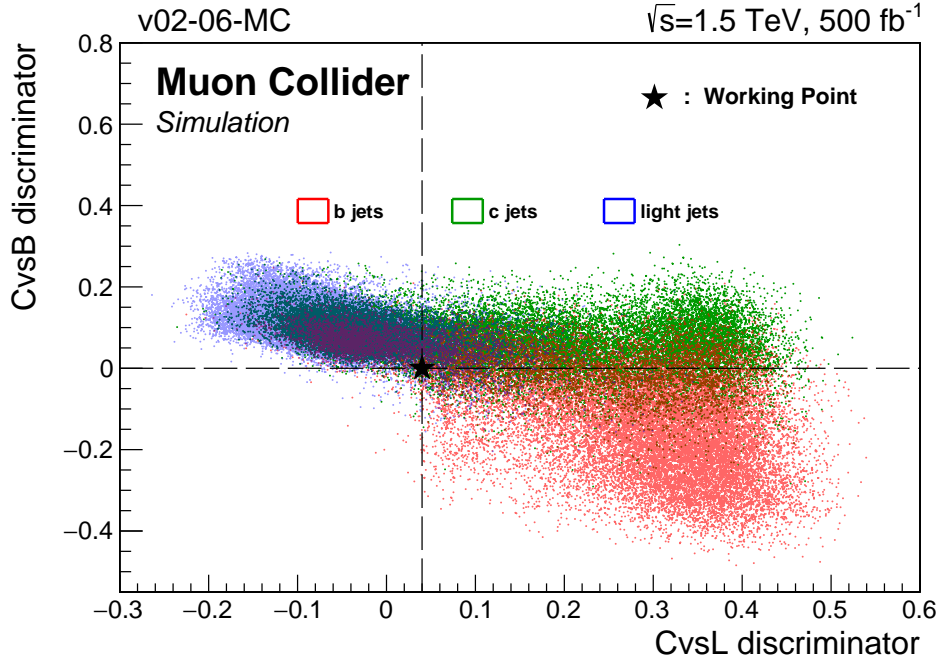


Figure 5.2: Correlation between CvsL and CvsB taggers for the different jet flavours, with a star indicating the chosen working point.

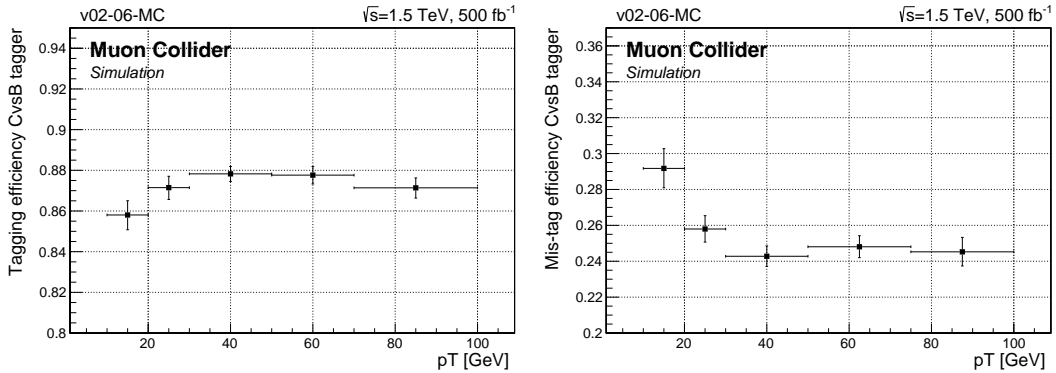


Figure 5.3: C tagging efficiency (left) and misidentification probability for b jets (left) as a function of the jet transverse momentum. The working point for CvsB is fixed at 0.

Table 5.2 reports the number of jets before and after the flavour tagging (combined action of the two discriminators). The efficiencies for the c jet samples are around 40 %, for the b jet samples about 14 % and for the light-flavour ones around 5 %, compatible with the magenta curve in Figure 4.19.

In order to build a Higgs candidate two reconstructed jets are needed in the event. Table 5.3 shows the number of events with at least two jets before and after the flavour tagging for each sample. For the c jet samples, selection efficiencies are 16-20 % (depending on the process), for the b jet samples around 2 %, and about 0.5 % or less for the light-flavour samples.

After the flavour tagging, several variables related to the jet pairs and the Higgs candidates are studied, in order to discard the non-peaking backgrounds.

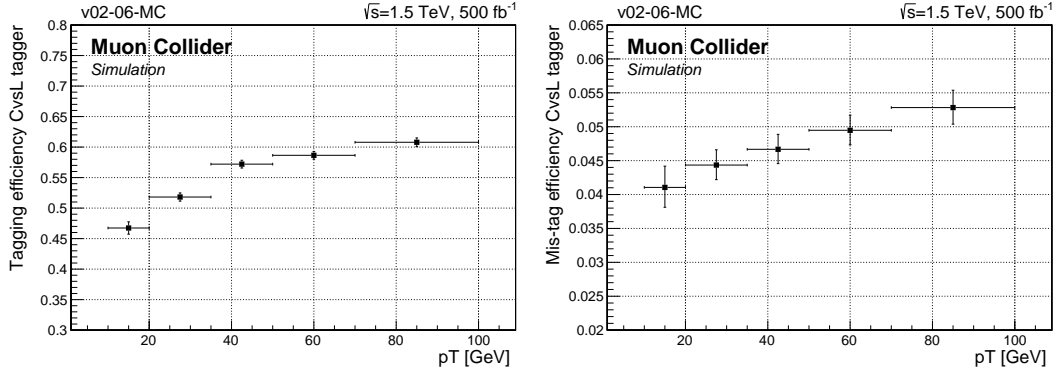


Figure 5.4: C tagging efficiency (left) and misidentification probability for light-flavour jets (left) as a function of the jet transverse momentum. The working point for CvsL is fixed at 0.04.

Physics process	N. of jets before tagging	N. of jets after tagging	Tagger efficiency
$\mu^+ \mu^- \rightarrow H \nu \bar{\nu}$ → $c\bar{c} \nu \bar{\nu}$	17658 ± 133	7621 ± 87	0.4316 ± 0.0037
$\mu^+ \mu^- \rightarrow c\bar{c} 2\text{lep}$	16035 ± 127	5945 ± 77	0.3708 ± 0.0038
$\mu^+ \mu^- \rightarrow H \nu \bar{\nu}$ → $b\bar{b} \nu \bar{\nu}$	17104 ± 131	2458 ± 50	0.1437 ± 0.0027
$\mu^+ \mu^- \rightarrow b\bar{b} 2\text{lep}$	9230 ± 96	1236 ± 35	0.1339 ± 0.0035
$\mu^+ \mu^- \rightarrow H \nu \bar{\nu}$ → $gg \nu \bar{\nu}$	19002 ± 138	1094 ± 33	0.0576 ± 0.0017
$\mu^+ \mu^- \rightarrow 2\text{light} 2\text{lep} (*)$	15803 ± 126	672 ± 26	0.0425 ± 0.0016
$\mu^+ \mu^- \rightarrow 2\text{light} 2\text{lep}$	18144 ± 135	852 ± 29	0.0470 ± 0.0016

Table 5.2: Number of jets for each process before and after the tagger application. The tagger efficiency is reported.

Physics process	N. of events with $n_j \geq 2$ before tagging	N. of events with $n_j \geq 2$ after tagging	Efficiency
$\mu^+ \mu^- \rightarrow H \nu \bar{\nu}$ → $c\bar{c} \nu \bar{\nu}$	7166 ± 85	1413 ± 38	0.1972 ± 0.0047
$\mu^+ \mu^- \rightarrow c\bar{c} 2\text{lep}$	5711 ± 76	929 ± 30	0.1627 ± 0.0049
$\mu^+ \mu^- \rightarrow H \nu \bar{\nu}$ → $b\bar{b} \nu \bar{\nu}$	6743 ± 82	148 ± 12	0.0219 ± 0.0018
$\mu^+ \mu^- \rightarrow b\bar{b} 2\text{lep}$	2760 ± 53	53 ± 7	0.0192 ± 0.0026
$\mu^+ \mu^- \rightarrow H \nu \bar{\nu}$ → $gg \nu \bar{\nu}$	7604 ± 87	42 ± 6	0.0055 ± 0.0008
$\mu^+ \mu^- \rightarrow 2\text{light} 2\text{lep} (*)$	6070 ± 78	14 ± 4	0.0023 ± 0.0006
$\mu^+ \mu^- \rightarrow 2\text{light} 2\text{lep}$	7551 ± 87	15 ± 4	0.0020 ± 0.0005

Table 5.3: Number of events with at least two jets for each process before and after the tagger application. The selection efficiency is reported.

The main goals are:

- The suppression of the background from light jets that is characterized by a huge cross section with respect to the signal process.
- The reduction of the c jet background, since it mostly survived the flavour tagging.

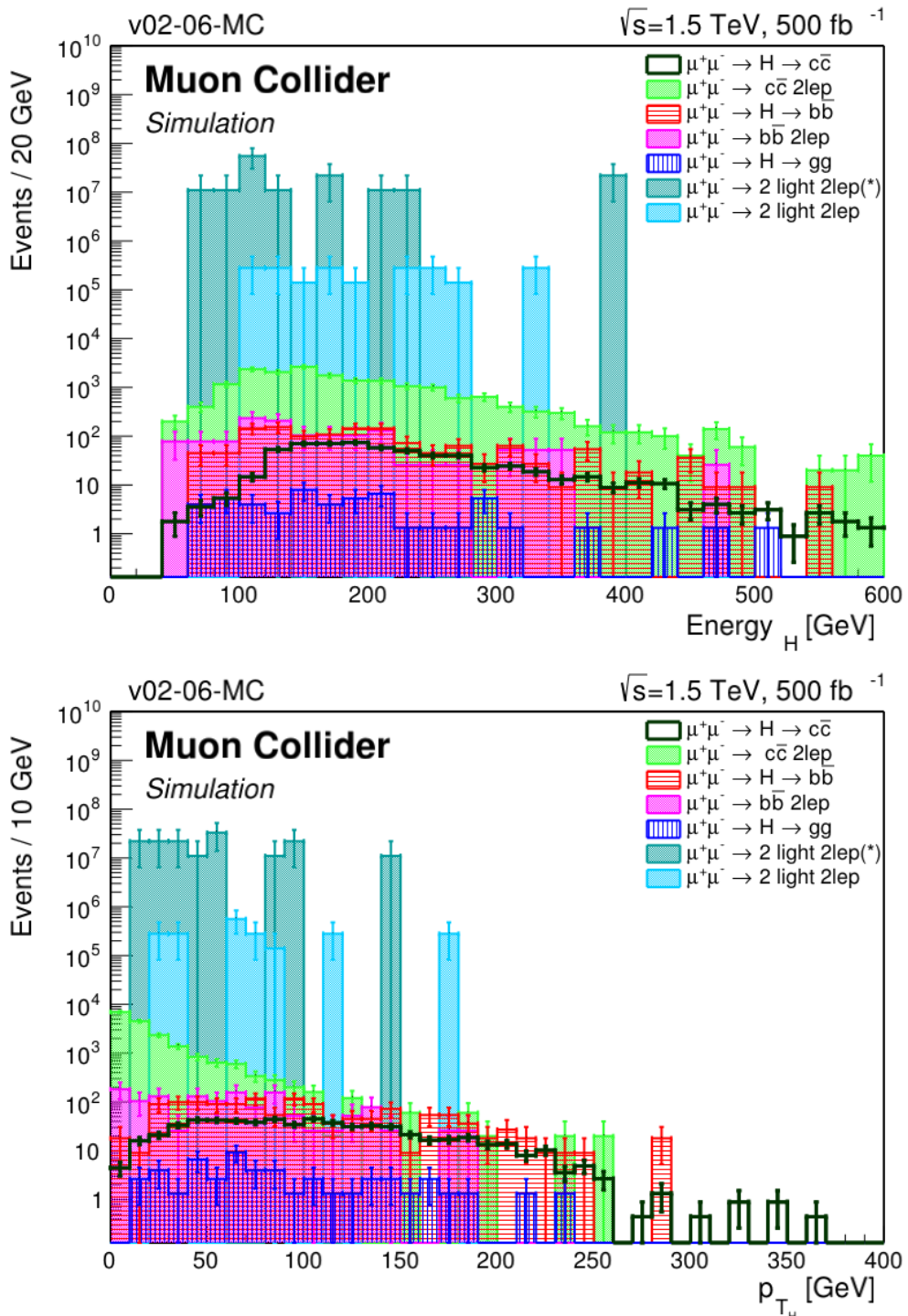
The relevant discriminating variables are the ΔR separation between jets, the transverse momentum, the energy and the invariant mass of the Higgs candidates. In Figures 5.5 the variables are shown for all the samples, after flavour tagging. The number of entries (n) is scaled to cross section (σ), total number of generated events (n_{tot}) and luminosity (\mathcal{L}), considering four years of data taking at $\sqrt{s} = 1.5 \text{ TeV}$ center of mass energy and $\mathcal{L}_{inst} = 1.25 \cdot 10^{34} \text{ cm}^{-2} \text{ s}^{-1}$ instantaneous luminosity. The following formula is used:

$$N = \frac{\mathcal{L} \cdot \sigma \cdot n}{n_{tot}} \quad (5.1)$$

The candidates in the non-peaking background samples are characterized by smaller energy and transverse momentum with respect to the signal. Furthermore the invariant mass of the candidates in the background processes is mostly shifted below the Higgs mass region. Finally, the ΔR distribution for c jet background is quite different, since jets appear to be more separated with respect to signal ones, with a peak right after 3 radians. After an optimization procedure aiming to maximize the efficiency of signal while reducing the background contamination, the following cuts are applied:

- Energy of the Higgs candidate greater than 130 GeV.
- Transverse momentum of the Higgs candidate greater than 30 GeV.
- ΔR between jets smaller than 3.
- Invariant mass in the *Higgs region*, defined by the range [110, 130] GeV.

In Table 5.4 the number of events surviving the first three selections and the relative efficiencies are reported. The remaining events in the Higgs mass region are from $H \rightarrow b\bar{b}$ and $H \rightarrow gg$ processes and from electroweak prompt c jet production. Table 5.5 reports the final yields, with the absolute efficiencies calculated with respect to the total number of generated events.



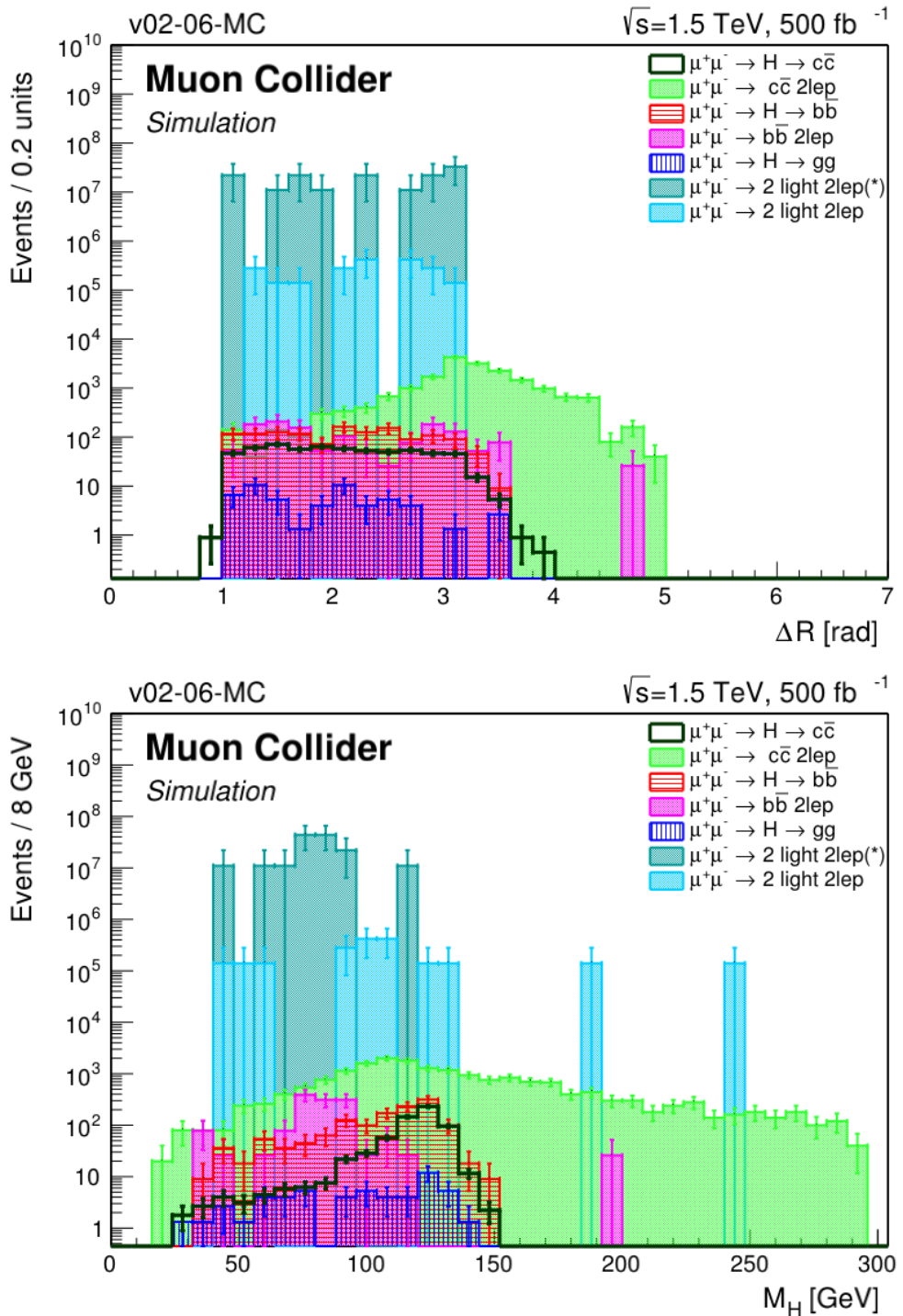


Figure 5.5: From top to bottom: energy, transverse momentum, ΔR and invariant mass of the di-jet system for all the samples after flavour tagging. Histograms are scaled to cross section and luminosity.

Physics process	$E_H > 130 \text{ GeV}$	Rel. Eff.	$p_{T_H} > 30 \text{ GeV}$	Rel. Eff.	$\Delta R(j_1, j_2) < 3$	Rel. Eff.
$\mu^+ \mu^- \rightarrow H \nu \bar{\nu} \rightarrow c \bar{c} \nu \bar{\nu}$	582 ± 16	0.925 ± 0.007	554 ± 16	0.953 ± 0.006	515 ± 15	0.929 ± 0.007
$\mu^+ \mu^- \rightarrow c \bar{c} 2lep$	13416 ± 518	0.723 ± 0.015	3693 ± 272	0.275 ± 0.017	2515 ± 224	0.681 ± 0.034
$\mu^+ \mu^- \rightarrow H \nu \bar{\nu} \rightarrow b \bar{b} \nu \bar{\nu}$	1035 ± 97	0.777 ± 0.034	990 ± 94	0.957 ± 0.019	954 ± 93	0.964 ± 0.018
$\mu^+ \mu^- \rightarrow b \bar{b} 2lep$	727 ± 137	0.528 ± 0.069	571 ± 122	0.786 ± 0.078	545 ± 119	0.955 ± 0.044
$\mu^+ \mu^- \rightarrow H \nu \bar{\nu} \rightarrow gg \nu \bar{\nu}$	40 ± 7	0.714 ± 0.070	37 ± 7	0.933 ± 0.046	37 ± 7	1 ± 0
$\mu^+ \mu^- \rightarrow 2light\ 2lep\ (*)$	$(7.7 \pm 2.9).10^7$	0.500 ± 0.134	$(5.5 \pm 2.5).10^7$	0.714 ± 0.171	$(4.4 \pm 2.2).10^7$	0.800 ± 0.179
$\mu^+ \mu^- \rightarrow 2light\ 2lep$	$(1.6 \pm 0.5).10^6$	0.733 ± 0.114	$(1.4 \pm 0.5).10^6$	0.909 ± 0.087	$(1.4 \pm 0.5).10^6$	1 ± 0

Table 5.4: Number of scaled events after each cut, together with the relative efficiencies.

Physics process	N. of events in the Higgs region after all selections	Absolute efficiency
$\mu^+ \mu^- \rightarrow H \nu \bar{\nu} \rightarrow c\bar{c} \nu \bar{\nu}$	378 ± 19	0.0849 ± 0.0028
$\mu^+ \mu^- \rightarrow c\bar{c} 2lep$	619 ± 25	0.0031 ± 0.0006
$\mu^+ \mu^- \rightarrow H \nu \bar{\nu} \rightarrow b\bar{b} \nu \bar{\nu}$	567 ± 24	0.0063 ± 0.0008
$\mu^+ \mu^- \rightarrow H \nu \bar{\nu} \rightarrow gg \nu \bar{\nu}$	19 ± 4	0.0014 ± 0.0004

Table 5.5: Number of surviving events (normalized to cross section and luminosity) in the Higgs region after all selections. The absolute efficiencies are reported. The unreported processes are completely rejected by the cuts.

5.3 Statistical analysis and results

After the selections described in the previous section, the number of expected signal events (S) is $S = 378$, while the expected background events (B) are $B = 1205$ (summing up all the contributions), accounting for an integrated luminosity of 500 fb^{-1} .

From these results, the significance of the signal, evaluated as $S/\sqrt{S+B}$, is 9.5. The uncertainty on the $H \rightarrow c\bar{c}$ production cross section is calculated through the following approximation [31]:

$$\frac{\Delta\sigma}{\sigma} \simeq \frac{\sqrt{S+B}}{S} \quad (5.2)$$

and is evaluated to be 10.5 %.

Since the Higgs boson production at $\sqrt{s} = 1.5 \text{ TeV}$ is dominated by *WW fusion*, the calculated uncertainty on the cross section is related to the Higgs boson coupling as follows:

$$\sigma = \sigma(\nu\nu H) \cdot BR(H \rightarrow c\bar{c}) = \frac{g_{HWW}^2 g_{Hcc}^2}{\Gamma_H} \quad (5.3)$$

where g_{HWW}^2 is the coupling of the Higgs boson to the W boson and the Γ_H is the Higgs boson width. No estimate of the precision achievable at Muon Collider on g_{HWW}^2 and Γ_H is yet available, so it is assumed that they can be measured with the same level of precision expected by CLIC at $\sqrt{s} = 1.4 \text{ TeV}$ [32] (scaled for the lower integrated luminosity assumed for the Muon Collider). This is justified by the fact that the selection of muonic final states at a muon collider is analogous to that at electron-positron accelerators, since the beam-induced background stops at the calorimeters and is not expected in muon detectors [31].

From Equation 5.3 it follows that the uncertainty on the coupling can be obtained with:

$$\frac{\Delta g_{Hcc}}{g_{Hcc}} = \frac{1}{2} \sqrt{\left(\frac{\Delta\sigma}{\sigma} \right)^2 + \left(\frac{\Delta \frac{g_{HWW}^2}{\Gamma_H}}{\frac{g_{HWW}^2}{\Gamma_H}} \right)^2} \quad (5.4)$$

The expected sensitivity on the Higgs coupling to c quark at $\sqrt{s} = 1.5 \text{ TeV}$ without the BIB overlay is then found to be 5.5 %.

The results are summarized in Table 5.6.

Table 5.7 shows the projection at $\sqrt{s} = 3 \text{ TeV}$, $\mathcal{L} = 1300 \text{ fb}^{-1}$, obtained assuming the same fraction of surviving events per each sample (reported in Table 5.5) and scaling the results to cross section and luminosity at the increased center of mass energy.

The results for the Muon collider presented here on the g_{Hcc} coupling are comparable to the CLIC ones [32] (Table 5.8), when both facility collect the same statistics. Next steps will concern evaluating the BIB effects on the reconstruction and analysis and estimating the systematic uncertainties related to the jet energy scale and resolution, the c tagging efficiency, the lepton efficiency and the uncertainty on theoretical cross section and luminosity.

\sqrt{s} [TeV]	\mathcal{L} [fb^{-1}]	S	B	$\frac{S}{\sqrt{S+B}}$	$\frac{\Delta\sigma}{\sigma}$	$\frac{\Delta g_{Hcc}}{g_{Hcc}}$
1.5	500	378	1205	9.5	10.5 %	5.5 %

Table 5.6: Signal and background yields, signal significance, uncertainty on $H \rightarrow c\bar{c}$ production cross section and uncertainty on the Hcc coupling at 1.5 TeV, 500 fb^{-1} integrated luminosity, without BIB overlay.

\sqrt{s} [TeV]	\mathcal{L} [fb^{-1}]	S	B	$\frac{S}{\sqrt{S+B}}$	$\frac{\Delta\sigma}{\sigma}$	$\frac{\Delta g_{Hcc}}{g_{Hcc}}$
3.0	1300	1565	4337	20.4	4.9 %	2.6 %

Table 5.7: Projected signal and background yields, signal significance, uncertainty on $H \rightarrow c\bar{c}$ production cross section and uncertainty on the Hcc coupling at 3 TeV, 1300 fb^{-1} integrated luminosity, without BIB overlay.

350 GeV – 500 fb⁻¹	1.4 TeV – 1.5 ab⁻¹	3 TeV – 2 ab⁻¹
6.2 %	2.3 %	1.9 %

Table 5.8: Relative precisions on the Hcc coupling at CLIC, for different energies and integrated luminosities. Each new stage at increased energy includes all measurements of the previous stages.

5.4 Future developments

The analysis outlined in this thesis led to a preliminary estimation of the precision achievable on the Hcc coupling at Muon Collider. An important role in this context has been played by the c tagger, here developed for the first time at the Muon Collider experiment.

More studies need to be carried out in the future, in order to understand and, possibly, mitigate the BIB impact on jet and vertex reconstruction as well as on tagger performance.

Improvements can be obtained on many levels:

- Different jet reconstruction algorithms can be tested. For example typical choices for lepton colliders are the *Durham* and *Cambridge-Aachen* ones,

or the new *Valencia* which integrates features of both lepton and hadron collider algorithms [77]. In any case, the choice of the strategy requires a dedicated study since the jet reconstruction is a delicate issue, especially for increasing center of mass energy: as the energy grows the jets tend to be closer and closer and thus difficult to be identified as separate objects (*boosted topology*).

- Machine Learning techniques can be used to built a single discriminator for the events, instead of applying the mentioned cuts on the Higgs candidates.
- Machine Learning techniques can also be exploited to improve the jet energy resolution through regression methods.
- Furthermore the analysis strategy can also be reversed, firstly applying cuts on Higgs candidate and then performing the flavour tagging on the remaining events (that in principle should be mainly $H \rightarrow c\bar{c}$, $H \rightarrow b\bar{b}$ and $H \rightarrow gg$). This procedure could possibly increase the efficiency on the signal selection and improve the final estimated sensitivity.
- Instead of using equation 5.2 for a conservative estimate of the cross section uncertainty, a combined fit to the di-jet invariant mass and discriminating kinematic variables can be performed, following CLIC approach, to improve the accuracy.
- An accurate design of the calorimeters, with appropriate timing and increased granularity, would improve the jet reconstruction performance and the BIB mitigation. Moreover the b-to-c discrimination would highly benefit from an optimized tracking stage.

Conclusions

Since its discovery in 2012, the Higgs boson has been at the center of the scientific community effort in the context of Particle Physics. Indeed, the Higgs boson is considered a powerful tool to explore the manifestations of the SM and to probe the physics landscape beyond it. The precise measurement of Higgs properties and couplings to SM particles has, thus, become the primary goal of the proposed Future Colliders, as even small deviation of these values from SM expectation could possibly reveal New Physics.

In this context, a future Muon Collider experiment has been proposed as an unconventional machine with several advantages with respect to the traditional hadronic and e^+e^- colliders. Nonetheless this novel approach poses some new technical challenges that are currently object of study. In particular, the machine background originated from beam muon decay, if not mitigated, can affect negatively the Muon Collider performance, deteriorating the detector components and worsening the object reconstruction. The interaction region has been specifically designed to prevent these effects and, presently, several strategies are under development with the aim of attenuating the background impact in the object reconstruction.

In this thesis, for the first time the search for $H \rightarrow c\bar{c}$ at the Muon Collider has been explored in order to estimate the precision achievable on the Higgs coupling to c quark. The signal process $\mu^+\mu^- \rightarrow H\nu\bar{\nu} \rightarrow c\bar{c}\nu\bar{\nu}$ has been fully simulated together with the main physics backgrounds at $\sqrt{s} = 1.5 \text{ TeV}$. The overlay of the machine background was not yet available due to computational limitation at the tracking stage, whose solution is currently under study. The main challenge faced in the analysis was the discrimination of c jets against b jets and light-flavour jets. Indeed, the features of c jets lie in between that of b jets and light-flavour ones. Moreover, the decay of the Higgs boson into charm quarks is less frequent than that into bottom quarks (factor 20) and that into gluons (factor 3). In order to achieve good identification performance, several variables, related to tracks, secondary vertices and soft leptons clustered in jets, are combined into a single powerful discriminator using Machine Learning techniques. The so-built tagger has reached performance comparable to that of the competitor lepton collider CLIC. The tagger has been employed in the analysis, obtaining a final relative uncertainty on the Higgs coupling to charm quark of 5.5%. A projection to $\sqrt{s} = 3 \text{ TeV}$ shows that the precision improves with increasing energy, reaching the value of 2.6%.

These results show that, under the hypothesis of an efficient machine background mitigation, Muon Collider performance is competitive with that of other Future Colliders. Moreover, the precision improvement with increasing energy and the potential to reach higher energy with respect to electron based colliders, may represent reasons to prefer Muon Collider over traditional machines.

This work will be presented at the 9th Edition of the Large Hadron Collider Physics Conference, planned from 7th to 12th June 2021.

In the next future, this search will be performed with the overlay of the full machine background, in order to estimate its effect on jet reconstruction, secondary vertex finding and c tagging efficiency. Contextually, the proposed mitigation procedures will be optimized and employed to obtain a good rejection power. The full study will be iterated at 10 TeV, carefully selecting the jet clustering algorithm in this high boost condition.

Appendices

Appendix A

Tagger input variables

The tagger input variables not presented in the text are reported here. All distributions are normalized to unit area. The last bin include the over-flow entries, the first bin the under-flow (if present).

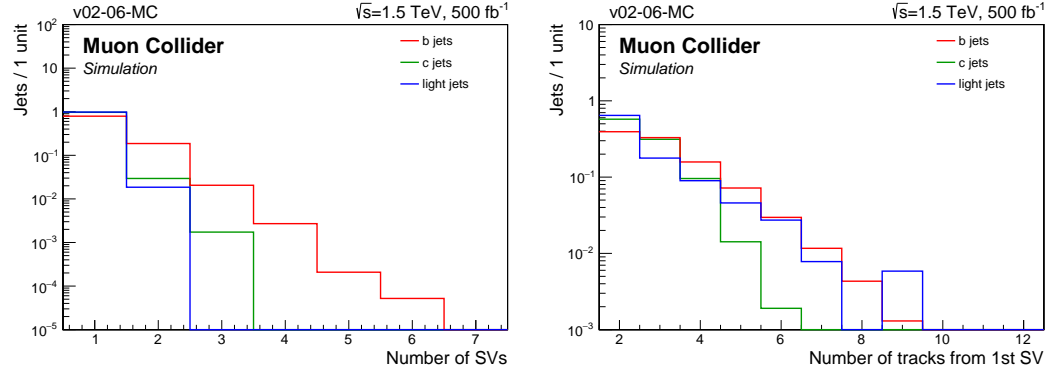


Figure A.1: The number of secondary vertices (left) and the number of tracks associated with the first SV (right) for jets in the RecoVertex category.

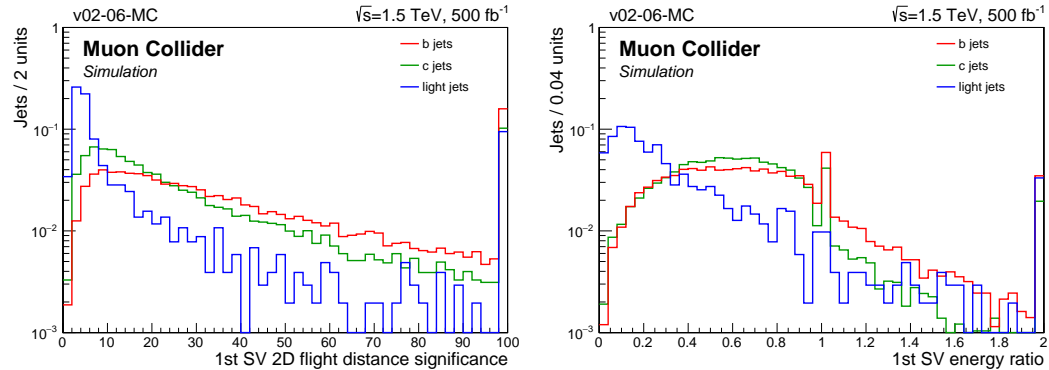


Figure A.2: The 2D flight distance significance (left) and the energy ratio (right) of the first SV for jets in the RecoVertex category.

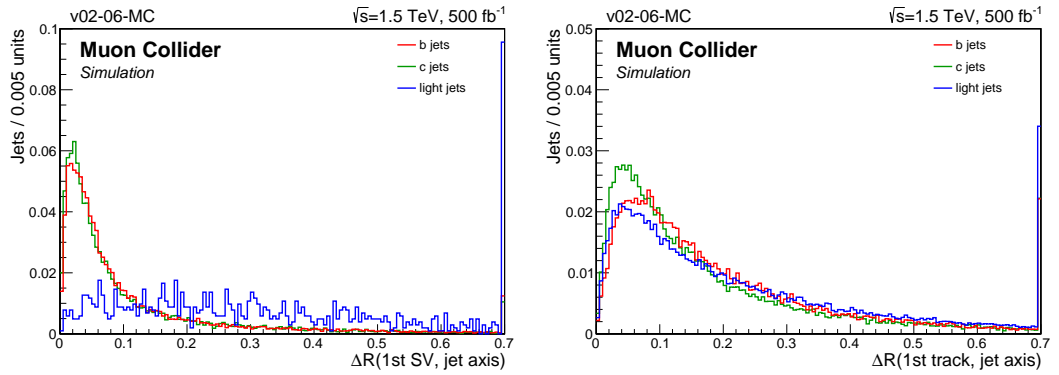


Figure A.3: The ΔR between the first SV and the jet axis for jets in the RecoVertex category (left) and the ΔR between the first track and the jet axis (right).

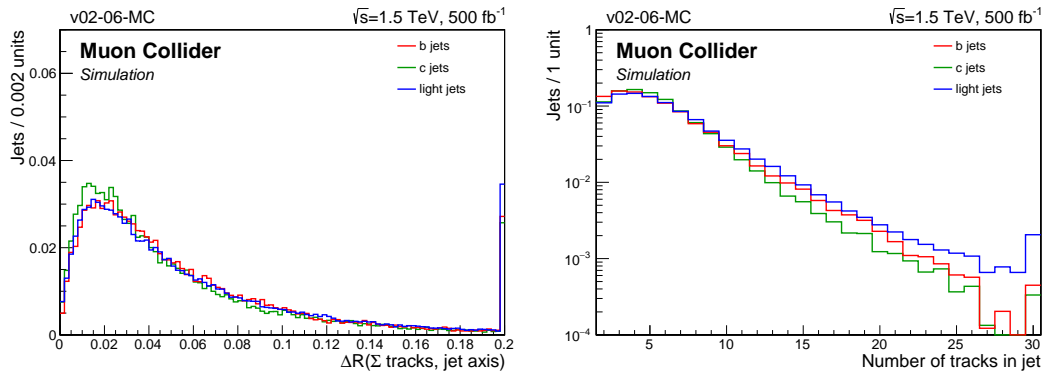


Figure A.4: The ΔR between the summed four-momentum vector of the tracks and the jet axis (left) and the number of tracks associated with the jet (right).

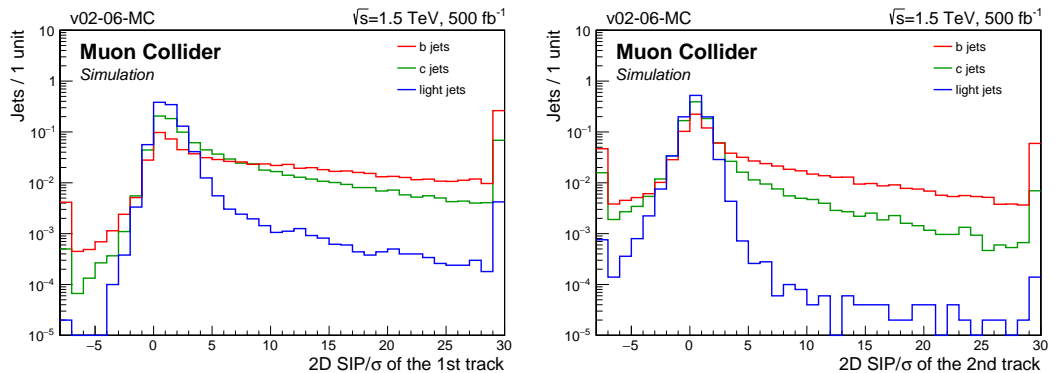


Figure A.5: The 2D SIP significance of the first two tracks.

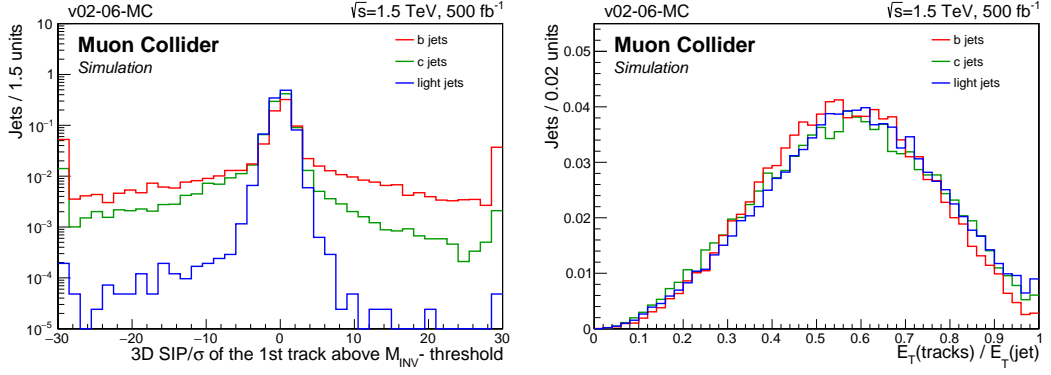


Figure A.6: The 3D SIP significance of the first track that raises the combined invariant mass of the tracks above 1.5 GeV (left) and the transverse energy of the total summed four-momentum vector of the selected tracks divided by the transverse energy of the jet (right).

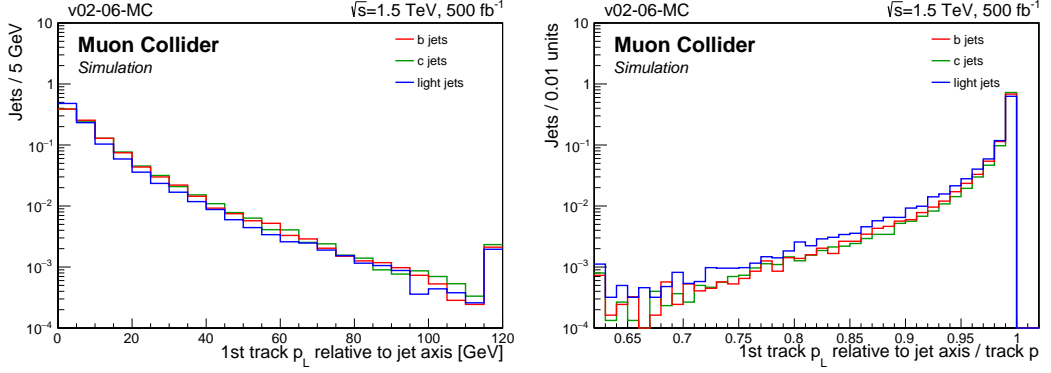


Figure A.7: The track momentum parallel to the jet direction (left) and the track momentum parallel to the jet direction divided by the magnitude of the track momentum vector (right), for the first track.

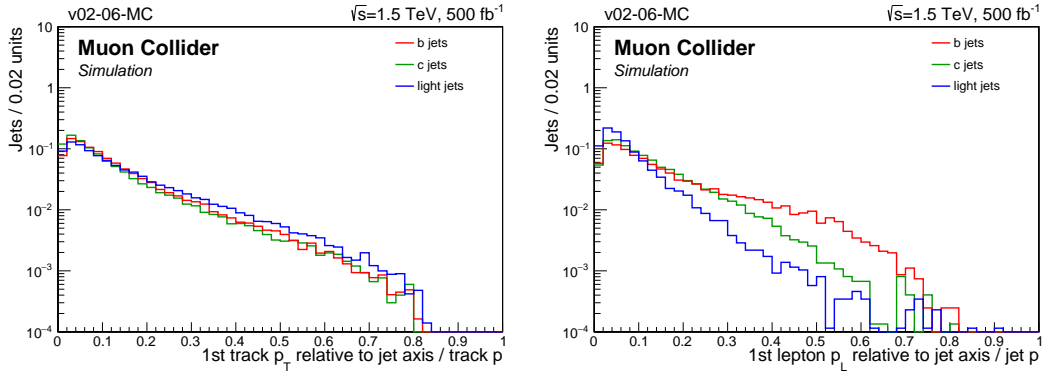


Figure A.8: The track p_T relative to the jet axis divided by the magnitude of the track momentum vector, for the first track (left) and the first lepton momentum parallel to the jet direction divided by the magnitude of the jet momentum, for jets in the SoftMuon or SoftElectron category (right).

Appendix B

Multivariate Analysis

In high-energy physics, with the search for ever smaller signals in ever larger data sets, it has become essential to extract a maximum of the available information from the data. As a consequence, multivariate classification methods based on machine learning techniques have become a fundamental ingredient to most analyses.

Machine Learning exploits algorithms to extract information from raw data and represent it in some type of model (training or learning step). Afterwards this model is employed to predict unknown data (application step).

The learning procedure can be either supervised or unsupervised. A supervised learning algorithm analyses *labelled* training data (for example events labelled as *signal* or *background*) and produces an inferred function, which can be used for mapping new examples. On the contrary, the unsupervised learning is a type of algorithm that learns patterns from untagged data.

Let's focus on the supervised learning. This type of algorithm receives as input the *training set*, i.e. a list of examples in the form of (\vec{x}_i, y_i) where \vec{x}_i denotes the input variables called *features* and y_i the output or *target* variable. The goal is to learn a function called *hypothesis* $h : X \rightarrow Y$ such that $h(\vec{x})$ is a good predictor for the corresponding value of y .

When the target variables is continuous the problem is called a *regression* problem, while if it can only take a small number of discrete values it is called a *classification* problem.

The main sources of errors that can prevent a learning algorithm from generalizing beyond their training set are:

- the *bias*, i.e. an error from erroneous assumptions in the learning algorithm (underfitting).
- the *variance*, i.e. an error from sensitivity to small fluctuations in the training set that can happen if the algorithm models the random noise in the training data, rather than the intended outputs (overfitting).

In the first case, the algorithm learns "too little", in the latter "too much".

In the next paragraphs the theory of a supervised algorithm used for classification problems, the Boosted Decision Tree, is outlined. Later on, the BDT will be used for classify events as *signal-like* or *background-like*.

B.1 The Decision Tree

A decision tree is a binary tree-structured classifier (see Figure B.1). The event classification consists of applying a set of cuts called $\{c_n\}$ on the features variables \vec{x} that are optimized in the training phase in order to maximize signal-background separation. It starts from an initial node, the *root node* that splits into two branches, which in turn are split as well and so on until a stopping condition is reached. The end nodes contain signal and background events. If there are more signal than background events in the end node it is labeled as a *signal-like* otherwise as a *background-like* [74] [78].

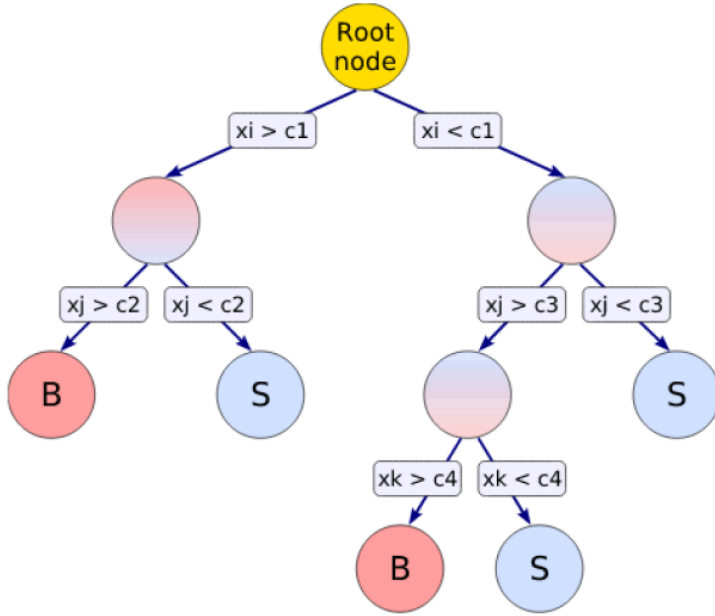


Figure B.1: Illustration of a Decision Tree. The rectangular boxes contain the cuts applied on the features (x_i , x_j and x_k), the circles represent nodes and the terminal ones contain the label S for signal and B for background.

For each nodes present in the n -th iteration/level, the Decision Tree algorithm controls if the stopping criterion is satisfied: if it is, the node is declared as terminal and labelled as *signal-like* or *background-like*, if it is not then:

- It sorts values for each feature.
- For each variable, it chooses the splitting value that allows the best separation between signal and background, performing a scan with a certain granularity.
- It finds the variables and splitting values that determine the best separation and splits the node into two other nodes: one containing events that pass the cut, the other one events that do not pass the cut.

Usually stopping conditions for the tree growth refers to a maximum depth of the tree (i.e. maximum number of layers of nodes allowed) and/or to a required minimum percentage of training events in the nodes.

A popular figure of merit for the goodness of splitting is the *Gini Index*, that for a two-class classification is:

$$G = 2p(1 - p) \quad \text{with} \quad p = \frac{s}{s + b} \quad (\text{B.1})$$

where p is called *purity* and s and b are the signal and background yields at each step in the process. In the training procedure variables and cut values that optimises the decrease of the Gini index between the parent node and the sum of the indices of the two daughter nodes are selected.

The main characteristics of decision trees can be summarized as follows:

- Trees can easily handle data with numeric or categorical variables or both types mixed, which means there's no need for the so called *dummification*.
- There's no need to transform inputs.
- Trees are resistant to irrelevant variables, because they simply avoid using them.
- Trees are resilient to the course of dimensionality, as a matter of fact they work well with many variables.
- The tree structure can be easily unstable: if, for example, there exist two features very similar in the discrimination power, a small statistical fluctuation can lead one to be preferred in the splitting procedure with respect to the other and the preferred can change from training set to training set. This could in principle lead the tree to be structured in a complete different way according to the training set used.
- Trees easily suffer of the overfitting problem, especially if the number of splitting levels is increased in order to have a better predictive power.

Usually the performances of the Decision Trees can be improved with the so called *ensamble methods*. The main idea of these algorithms is that combining together many weak learners (as small decision trees), as long as the performance of each one is slightly better than random guessing, a strong learner can be built. This is the philosophy of the *Adaptive Boosting* explained in the next section B.2. The boosting of a decision tree improves its predictive power thus reducing the bias error. In order to reduce the variance and increase stability another techniques is generally employed: the *bagging*. It points to diversifying the weak learners by training them on slightly different samples. The training data for each tree are built by drawing at random a subsample from the initial training set. In this way, tuning carefully the tree depth and the number of trees, the overfitting can be avoided.

B.2 Boosting of a tree

A boosting algorithm works sequentially: the sampling distribution is modified for every weak learner using information from the weak learners constructed earlier. This modification amounts to adjusting weights for observations in the training set, allowing the next weak learner to focus on the poorly studied region of the input space [79].

The AdaBoost algorithm, in particular, works as follows:

1. It receives in input the training data $(\vec{x}_i, y_i, w_i)_{i=1}^N$, where w_i are the possible weights assigned to the N events, and the number of iterations (i.e. trees) T .
2. It initializes the weights for the first tree

$$w_i^{(1)} = \frac{w_i}{\sum_i^N w_i} \quad \text{for } i = 1, \dots, N \quad (\text{B.2})$$

3. For $t = 1$ to T it does:

- (a) Training of classifier on $(\vec{x}_i, y_i, w_i^{(t)})_{i=1}^N$ to obtain hypothesis $h_t : x \rightarrow \{-1, +1\}$.
- (b) Calculation of the training error $\epsilon_t = \sum_i^N w_i^{(t)} I(y_i \neq h_t(\vec{x}_i))$, where the $I = 1$ if its argument is true, zero otherwise.
- (c) Control on the training error: if it is not in the allowed range $(0, 1/2)$ the loop is exited and T is set to $t - 1$.
- (d) Calculation of the hypothesis weight $\alpha_t = \beta \log \frac{1-\epsilon_t}{\epsilon_t}$.
- (e) Updating of the observation weights

$$w_i^{(t+1)} = \frac{w_i^t e^{-\alpha_t y_i h_t(\vec{x}_i)}}{\sum_i^N w_i^{(t)} e^{-\alpha_t y_i h_t(\vec{x}_i)}} \quad (\text{B.3})$$

4. It returns the score $f(\vec{x})$ of the final strong hypothesis calculated as a weighted sum of predictions from the weak hypotheses:

$$f(\vec{x}) = \sum_t^T \alpha_t h_t(\vec{x}) \quad (\text{B.4})$$

B.3 Kolmogorov-Smirnov test

A convenient way to detect overtraining is to compare the distributions of the classifier output between the training sample and a different sample, called the *test sample*. The Kolmogorov-Smirnov test (K-S) is the most straightforward test of the difference between two cumulative distributions (cdf). The test statistic is built using the maximum difference between the two cumulative distributions being compared.

Given a pair of cdfs F and G on a sample space, it is possible to define a distance or metric, $\rho(F, G)$, that returns a non-negative number satisfying all the usual properties of a distance on a metric space, as:

$$\rho(F, G) \equiv \sup_x |F(x) - G(x)| \quad (\text{B.5})$$

In this case, F and G are the empirical cdfs of the training and test dataset. The K-S test returns the *p-value*, i.e. the probability of obtaining the discrepancy observed under the assumption that the null hypothesis is correct. The null hypothesis here is that the two distributions (training and test ones) come from the same population. Usually a significance level α is fixed a priori (typical values are 0.05 and 0.01), and if the *p-value* is greater than α the null hypothesis is accepted, otherwise is rejected.

Bibliography

- [1] European Strategy for Particle Physics Preparatory Group. “Physics Briefing Book” (2020). arXiv: 1910.11775.
- [2] J. de Blas et al. “Higgs Boson studies at future particle colliders”. *Journal of High Energy Physics* 2020.1 (2020). DOI: 10.1007/jhep01(2020)139. arXiv: 1905.03764.
- [3] Particle Data Group Collaboration. “Review of Particle Physics”. *Progress of Theoretical and Experimental Physics* 2020.8 (2020). DOI: 10.1093/ptep/ptaa104.
- [4] CMS Collaboration. “Observation of a new boson at a mass of 125 GeV with the CMS experiment at the LHC”. *Physics Letters B* 716.1 (2012). DOI: 10.1016/j.physletb.2012.08.021. arXiv: 1207.7235.
- [5] ATLAS Collaboration. “Observation of a new particle in the search for the Standard Model Higgs boson with the ATLAS detector at the LHC”. *Physics Letters B* 716.1 (2012). DOI: 10.1016/j.physletb.2012.08.020. arXiv: 1207.7214.
- [6] A. Ali and G. Kramer. “JETS and QCD: a historical review of the discovery of the quark and gluon jets and its impact on QCD”. *The European Physical Journal H* 36.2 (2011). DOI: 10.1140/epjh/e2011-10047-1. arXiv: 1012.2288.
- [7] D. J. Gross and F. Wilczek. “Ultraviolet Behavior of Non-Abelian Gauge Theories”. *Phys. Rev. Lett.* 30 (1973). DOI: 10.1103/PhysRevLett.30.1343.
- [8] H. David Politzer. “Reliable Perturbative Results for Strong Interactions?” *Phys. Rev. Lett.* 30 (1973). DOI: 10.1103/PhysRevLett.30.1346.
- [9] Otto Nachtmann. *Elementary particle physics: concepts and phenomena*. Springer Science & Business Media, 2012.
- [10] J. Wess and B. Zumino. “A lagrangian model invariant under supergauge transformations”. *Physics Letters B* 49.1 (1974). DOI: [https://doi.org/10.1016/0370-2693\(74\)90578-4](https://doi.org/10.1016/0370-2693(74)90578-4).
- [11] D. B. Kaplan, H. Georgi, and S. Dimopoulos. “Composite Higgs Scalars”. *Phys. Lett. B* 136 (1984). DOI: 10.1016/0370-2693(84)91178-X.
- [12] M. Bauer, M. Carena, and K. Gemmeler. “Creating the fermion mass hierarchies with multiple Higgs bosons”. *Physical Review D* 94.11 (2016). DOI: 10.1103/physrevd.94.115030. arXiv: 1512.03458.

- [13] R. Barbieri, L. J. Hall, and V. S. Rychkov. “Improved naturalness with a heavy Higgs boson: An alternative road to CERN LHC physics”. *Physical Review D* 74.1 (2006). DOI: 10.1103/physrevd.74.015007. arXiv: hep-ph/0603188.
- [14] D. E. Morrissey and M. J. Ramsey-Musolf. “Electroweak baryogenesis”. *New Journal of Physics* 14.12 (2012). DOI: 10.1088/1367-2630/14/12/125003. arXiv: 1206.2942.
- [15] CMS Collaboration. “Combined measurements of Higgs boson couplings in proton–proton collisions at $\sqrt{s} = 13$ TeV”. *The European Physical Journal C* 79.5 (2019). DOI: 10.1140/epjc/s10052-019-6909-y. arXiv: 1809.10733.
- [16] ATLAS Collaboration. “Combined measurements of Higgs boson production and decay using up to 80 fb^{-1} of proton-proton collision data at $\sqrt{s} = 13$ TeV collected with the ATLAS experiment”. *Physical Review D* 101.1 (2020). DOI: 10.1103/physrevd.101.012002. arXiv: 1909.02845.
- [17] CMS Collaboration. “Evidence for Higgs boson decay to a pair of muons”. *Journal of High Energy Physics* 2021.1 (2021). DOI: 10.1007/jhep01(2021)148. arXiv: 2009.04363.
- [18] CMS Collaboration. “A search for the standard model Higgs boson decaying to charm quarks”. *Journal of High Energy Physics* 2020.3 (2020). DOI: 10.1007/jhep03(2020)131. arXiv: 1912.01662.
- [19] ATLAS Collaboration. “Search for Higgs boson pair production in the two bottom quarks plus two photons final state in pp collisions at $\sqrt{s} = 13$ TeV with the ATLAS detector”. ATLAS-CONF-2021-016 (2021). URL: <https://cds.cern.ch/record/2759683>.
- [20] M. Cepeda et al. “Higgs Physics at the HL-LHC and HE-LHC” (2019). arXiv: 1902.00134.
- [21] FCC Collaboration. “FCC Physics Opportunities: Future Circular Collider Conceptual Design Report Volume 1”. *European Physical Journal C* 79.6 (2019). DOI: 10.1140/epjc/s10052-019-6904-3.
- [22] ILC Collaboration. “The International Linear Collider: A Global Project” (2019). arXiv: 1903.01629.
- [23] CLIC Collaboration. “The Compact Linear Collider (CLIC) - 2018 Summary Report” (2018). arXiv: 1812.06018.
- [24] The CEPC Study Group. “CEPC Conceptual Design Report: Volume 2 - Physics & Detector” (2018). arXiv: 1811.10545.
- [25] J. L. Abelleira Fernandez et al. “A Large Hadron Electron Collider at CERN Report on the Physics and Design Concepts for Machine and Detector”. *Journal of Physics G: Nuclear and Particle Physics* 39.7 (2012). DOI: 10.1088/0954-3899/39/7/075001. arXiv: 1206.2913.
- [26] R. B. Palmer et al. “Muon colliders”. *AIP Conference Proceedings* 372.1 (1996), pp. 3–30. DOI: 10.1063/1.50922.

- [27] J. P. Delahaye et al. “Enabling Intensity and Energy Frontier Science with a Muon Accelerator Facility in the U.S.: A White Paper Submitted to the 2013 U.S. Community Summer Study of the Division of Particles and Fields of the American Physical Society” (2013). arXiv: 1308.0494.
- [28] J. P. Delahaye et al. “Muon Colliders” (2019). arXiv: 1901.06150.
- [29] T. Han et al. “Electroweak couplings of the Higgs boson at a multi-TeV muon collider”. *Physical Review D* 103.1 (2021). DOI: 10.1103/physrevd.103.013002. arXiv: 2008.12204.
- [30] A. Costantiniet al. “Vector boson fusion at multi-TeV muon colliders”. *Journal of High Energy Physics* 2020.9 (2020). DOI: 10.1007/jhep09(2020)080. arXiv: 2005.10289.
- [31] N. Bartosik et al. “Detector and Physics Performance at a Muon Collider”. *Journal of Instrumentation* 15.05 (2020). DOI: 10.1088/1748-0221/15/05/p05001. arXiv: 2001.04431.
- [32] H. Abramowicz et al. “Higgs physics at the CLIC electron–positron linear collider”. *The European Physical Journal C* 77.7 (2017). DOI: 10.1140/epjc/s10052-017-4968-5. arXiv: 1608.07538.
- [33] M. A. Palmer. “The US muon accelerator program” (2015). arXiv: 1502.03454.
- [34] M. Boscolo, J. P. Delahaye, and M. Palmer. “The Future Prospects of Muon Colliders and Neutrino Factories”. *Reviews of Accelerator Science and Technology* (2019). DOI: 10.1142/9789811209604_0010. arXiv: 1808.01858.
- [35] N.V. Mokhov and S.I. Striganov. “Detector Backgrounds at Muon Colliders”. *Physics Procedia* 37 (2012). DOI: <https://doi.org/10.1016/j.phpro.2012.03.761>.
- [36] M. Antonelli et al. “Novel proposal for a low emittance muon beam using positron beam on target”. *Nuclear Instruments and Methods in Physics Research Section A: Accelerators, Spectrometers, Detectors and Associated Equipment* 807 (2016). DOI: 10.1016/j.nima.2015.10.097. arXiv: 1509.04454.
- [37] D. Alesini et al. “Positron driven muon source for a muon collider” (2019). arXiv: 1905.05747.
- [38] R. P. Johnson. “Ionization Cooling and Muon Colliders”. *Proceedings of EPAC08, Genova, Italy* (2008).
- [39] Y. R. Roblin et al. “Recirculating linear accelerators for future muon facilities”. *AIP Conference Proceedings* 1423.1 (2012). DOI: 10.1063/1.3688840.
- [40] D. J. Summers. “Muon Acceleration using Fixed Field, Alternating Gradient (FFAG) Rings”. *International Journal of Modern Physics A* 20.16 (2005). DOI: 10.1142/s0217751x05027813. arXiv: physics/0411218.
- [41] J. Eldred, V. Lebedev, and A. Valishev. “Rapid-cycling synchrotron for multi-megawatt proton facility at Fermilab”. *Journal of Instrumentation* 14.07 (2019). DOI: 10.1088/1748-0221/14/07/p07021.

- [42] N. Mokhov and A. Van Ginneken. “Neutrino Radiation at Muon Colliders and Storage Rings”. *Journal of Nuclear Science and Technology* 37.sup1 (2000). DOI: 10.1080/00223131.2000.10874869.
- [43] D. Arominski et al. “A detector for CLIC: main parameters and performance” (2018). arXiv: 1812.07337.
- [44] N. V. Mokhov et al. “Muon Collider interaction region and machine-detector interface design” (2012). arXiv: 1202.3979.
- [45] N. V. Mokhov. “Status of MARS code”. FERMILAB-CONF-03-053 (2003).
- [46] Muon Collider Group. “Muon Collider detector geometry description” (updated). URL: https://github.com/MuonColliderSoft/detector-simulation/blob/master/geometries/MuColl_v1/text_description.md.
- [47] V. Di Benedetto et al. “A study of muon collider background rejection criteria in silicon vertex and tracker detectors”. *Journal of Instrumentation* 13.09 (2018). DOI: 10.1088/1748-0221/13/09/p09004. arXiv: 1807.00074.
- [48] N. Bartosik et al. “Preliminary Report on the Study of Beam-Induced Background Effects at a Muon Collider” (2019). arXiv: 1905.03725.
- [49] Muon Collider Group. “Muon Collider detector: tracking detector” (updated). URL: <https://confluence.infn.it/display/muoncollider/Tracking+detector>.
- [50] N. Bartosik. “Track reconstruction consideration for the Muon Collider” (2021). URL: https://agenda.infn.it/event/26135/contributions/132719/attachments/79910/104092/2021_03_10_bartosik.pdf.
- [51] L. Sestini et al. “Update on jet reconstruction and calorimeter simulation” (2021). URL: https://agenda.infn.it/event/26925/contributions/136243/attachments/81218/106303/calo_meeting.pdf.
- [52] N. Bartosik. “Object-reconstruction optimisation at Muon Collider” (2021). URL: https://indico.cern.ch/event/1028474/contributions/4318440/attachments/2225479/3774867/2021_04_07_bartosik_v1.pdf.
- [53] G. P. Cacciari M. and Salam and G. Soyez. “FastJet user manual”. *The European Physical Journal C* 72.3 (2012). DOI: 10.1140/epjc/s10052-012-1896-2. arXiv: 1111.6097.
- [54] Taikan Suehara and Tomohiko Tanabe. “LCFIPplus: A framework for jet analysis in linear collider studies”. *Nuclear Instruments and Methods in Physics Research Section A: Accelerators, Spectrometers, Detectors and Associated Equipment* 808 (2016). DOI: 10.1016/j.nima.2015.11.054. arXiv: 1506.08371.
- [55] “iLCSoft repository” (updated). URL: <https://github.com/iLCSoft>.
- [56] F. Gaede et al. “LCIO - A persistency framework for linear collider simulation studies” (2003). arXiv: physics/0306114.

- [57] M. Frank et al. “DD4hep: A Detector Description Toolkit for High Energy Physics Experiments”. *Journal of Physics: Conference Series* 513.2 (2014). DOI: 10.1088/1742-6596/513/2/022010.
- [58] R Brun, A Gheata, and M Gheata. “The ROOT geometry package”. *Nuclear Instruments and Methods in Physics Research Section A: Accelerators, Spectrometers, Detectors and Associated Equipment* 502.2 (2003). DOI: [https://doi.org/10.1016/S0168-9002\(03\)00541-2](https://doi.org/10.1016/S0168-9002(03)00541-2).
- [59] S. Agostinelli et al. “Geant4—a simulation toolkit”. *Nuclear Instruments and Methods in Physics Research Section A: Accelerators, Spectrometers, Detectors and Associated Equipment* 506.3 (2003). DOI: [https://doi.org/10.1016/S0168-9002\(03\)01368-8](https://doi.org/10.1016/S0168-9002(03)01368-8).
- [60] O. Wendt, Frank Gaede, and T. Krämer. “Event reconstruction with MarlinReco at the International Linear Collider”. *Pramana* 69 (2008). DOI: 10.1007/s12043-007-0237-8.
- [61] T. Kraemer and DESY. “Track Parameters in LCIO”. *LC-Notes* (2006). URL: <https://bib-pubdb1.desy.de/record/81214>.
- [62] “MarlinTrkProcessors repository” (updated). URL: <https://github.com/MuonColliderSoft/MarlinTrkProcessors/tree/master/source/Utils>.
- [63] E. Brondolin et al. “Conformal tracking for all-silicon trackers at future electron–positron colliders”. *Nuclear Instruments and Methods in Physics Research Section A: Accelerators, Spectrometers, Detectors and Associated Equipment* 956 (2020). DOI: 10.1016/j.nima.2019.163304. arXiv: 1908.00256.
- [64] Emilia Leogrande. “Conformal tracking for the CLIC detector”. CLICdp-Conf-2018-004 (2018). URL: <http://cds.cern.ch/record/2630512>.
- [65] P. Billoir. “Progressive track recognition with a Kalman-like fitting procedure”. *Computer Physics Communications* 57.1 (1989). DOI: [https://doi.org/10.1016/0010-4655\(89\)90249-X](https://doi.org/10.1016/0010-4655(89)90249-X).
- [66] P. Billoir and S. Qian. “Simultaneous pattern recognition and track fitting by the Kalman filtering method”. *Nuclear Instruments and Methods in Physics Research Section A: Accelerators, Spectrometers, Detectors and Associated Equipment* 294.1 (1990). DOI: [https://doi.org/10.1016/0168-9002\(90\)91835-Y](https://doi.org/10.1016/0168-9002(90)91835-Y).
- [67] J. S. Marshall and M. A. Thomson. “The Pandora Particle Flow Algorithm” (2013). arXiv: 1308.4537.
- [68] M.A. Thomson. “Particle flow calorimetry and the PandoraPFA algorithm”. *Nuclear Instruments and Methods in Physics Research Section A: Accelerators, Spectrometers, Detectors and Associated Equipment* 611.1 (2009). DOI: 10.1016/j.nima.2009.09.009.
- [69] T. H. Tran. “PandoraPFA - a brief introduction” (2012). URL: <https://indico.in2p3.fr/event/7483/contributions/42227/attachments/33987/41889/PandoraPFA.pdf>.

- [70] S. Marzani, G. Soyez, and M. Spannowsky. “Looking inside jets: an introduction to jet substructure and boosted-object phenomenology”. *Lecture Notes in Physics* (2019). DOI: 10.1007/978-3-030-15709-8. arXiv: 1901.10342.
- [71] CMS Collaboration. “Identification of heavy-flavour jets with the CMS detector in pp collisions at 13 TeV”. *Journal of Instrumentation* 13.05 (2018). DOI: 10.1088/1748-0221/13/05/p05011. arXiv: 1712.07158.
- [72] F. James and M. Roos. “MINUIT: a system for function minimization and analysis of the parameter errors and corrections”. *Comput. Phys. Commun.* 10.CERN-DD-75-20 (1975).
- [73] D. Schulte. “Muon Collider parameters at different energies” (2020). URL: https://indico.cern.ch/event/886491/contributions/3797137/attachments/2012900/3363906/MuonMeeting_2020_final.pdf.
- [74] A. Hoecker et al. “TMVA - Toolkit for Multivariate Data Analysis” (2007). arXiv: physics/0703039.
- [75] T. Sjöstrand, S. Mrenna, and P. Skands. “A brief introduction to PYTHIA 8.1”. *Computer Physics Communications* 178.11 (2008). DOI: 10.1016/j.cpc.2008.01.036. arXiv: 0710.3820.
- [76] J. Alwall et al. “MadGraph 5: going beyond”. *Journal of High Energy Physics* 2011.6 (2011). DOI: 10.1007/jhep06(2011)128. arXiv: 1106.0522.
- [77] M. Vos. “Jet reconstruction at future lepton colliders” (2016). URL: <https://indico.cern.ch/event/557400/contributions/2372731/attachments/1375434/2089005/jetsLC.pdf>.
- [78] Y. Coadou. “Boosted decision trees” (2016). URL: https://indico.cern.ch/event/472305/contributions/1982360/attachments/1224979/1792797/ESIPAP_MVA160208-BDT.pdf.
- [79] Ilya Narsky and Frank C Porter. *Statistical analysis techniques in particle physics*. Wiley Online Library, 2013.

Ringraziamenti

La mia più sentita riconoscenza per lo svolgimento di questo lavoro di tesi va alle mie due relatrici, la Prof.ssa Anna Colaleo e la Dott.ssa Rosma Venditti. Mi hanno sempre spronato a dare il meglio e a superare con caparbietà le difficoltà tecniche e gli imprevisti incontrati lungo il percorso. Le ringrazio, in particolare, per avermi proposto un argomento così interessante ed innovativo che mi ha permesso di cimentarmi in studi mai esplorati. Ringrazio inoltre Filippo Errico per i suoi preziosi consigli e le sue schiette opinioni.

La mia gratitudine va all'intera comunità nascente del Muon Collider, perché i numerosi meeting sono stati un'occasione di arricchimento professionale. In particolare, vorrei ringraziare Nazar Bartosik, Laura Buonincontri, Massimo Casarsa, Alessio Gianelle, Simone P. Griso, Donatella Lucchesi, Nadia Pastrone e Lorenzo Sestini, dal momento che il confronto costante con loro e la loro esperienza nel campo sono stati fondamentali per lo sviluppo di questo lavoro .

Per ultimo nell'ambito di questa esperienza, il ringraziamento è d'obbligo per la mia compagna di studi di sempre (e ora anche di tesi), Angela Zaza. La sua presenza e il suo supporto mi hanno permesso di alleggerire la fatica di questi sei mesi, avvallando la tesi che "due teste sono sempre meglio di una".

In ambito universitario vorrei ringraziare tutti i professori che ho incontrato lungo questo percorso che mi hanno arricchito dal punto di vista didattico ed umano. Un ringraziamento speciale va al Prof. Salvatore Nuzzo che ha creduto in me dall'inizio e mi ha indirizzato verso questo gruppo di lavoro.

L'università mi ha regalato tanto in questi anni, compresi degli amici sinceri sempre presenti, che qui ringrazio calorosamente.

Dedico questa tesi alla mia famiglia, a Marco e alle amiche di una vita che mi supportano e mi sopportano con infinita pazienza, e che spero di ringraziare ogni giorno con il mio affetto più sincero.